5-2023

Modeling, simulation and control of microrobots for the microfactory.

Zhong Yang
University of Louisville

MODELING, SIMULATION AND CONTROL OF MICROROBOTS FOR THE MICROFACTORY

By

Zhong Yang

B.E., Tianjin University, 2012

M.S., University of Arizona, 2016

A Dissertation

Submitted to the Faculty of the

J.B. Speed School of Engineering of the University of Louisville

In Partial Fulfillment of the Requirements

for the Degree of

Doctor of Philosophy

in Electrical Engineering

Department of Electrical and Computer Engineering

University of Louisville

Louisville, Kentucky

May 2023

MODELING, SIMULATION AND CONTROL OF MICROROBOTS FOR THE MICROFACTORY

By

Zhong Yang
B.E., Tianjin University, 2012
M.S., University of Arizona, 2015

A Dissertation Approved on

April 21, 2023

by the following Dissertation Committee:

Dan O. Popa

Olfa Nasraoui

Kevin D. Murphy

Tamer Inanc

Michael L. McIntyre

And God said, "Let there be light," and there was light.

Genesis 1:3

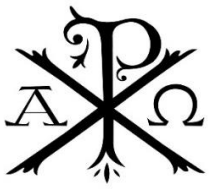

ACKNOWLEDGEMENTS

First, I would like to thank Jesus the Lord. He is my savior who helped me get through all the challenges and struggles in my life and research. He is my strength and has given me wisdom. All glory belongs to God.

Secondly, I would like to thank Dr. Popa for giving me the opportunity to study in the PhD program and Dr. Ruoshi Zhang for introducing me to the lab. When I was stuck in Mexico, Dr. Andriy Sherehiy, Dr. Moath Alqatamin, Brooke Ritz, and Mojtaba Al Hudibi helped me with a lot of experiments. Without their efforts, I would not have been able to finish this research.

Dr. Sri Sukanta Chowdhury and Dr. Mohammad Nasser Saadatzi provided me with a lot of good suggestions and guidance, while Dr. Michael Martin and Dr. Julia Aebersold helped me greatly with the fabrication in the cleanroom. Johanna Boone and Jordan Jones provided administrative support that helped keep our lab well-organized, and Courtney Kerr assisted me with the formatting of my dissertation. I am also grateful to my parents, who sacrificed a lot for me and supported my studies abroad. Additionally, I want to express my thanks to the American taxpayers and the National Science Foundation, whose funding made this research possible. Conducting such research is extremely difficult without proper funding.

The work presented in this thesis was supported by projects IIS-1633119, "EAGER: Cybermanufacturing: Design Tools for Nanofactories with Robust Millimetric Assemblers," from 09/01/2015-08/31/2017, CMMI #1734383, NRI: FND: Light-Powered

Microrobots for Future Microfactories, from 09/01/2017-08/31/2021, and through the Kentucky NSF EPSCOR KAMPERS project IIP #1849213, "RII Track-1: Kentucky Advanced Manufacturing Partnership for Enhanced Robotics and Structures," from 07/01/2019-06/30/2024.

Lastly, I would like to thank Mexico for its hospitality, which helped me get through the hard time of my life. ¡Viva México!

ABSTRACT

MODELING, SIMULATION AND CONTROL OF MICROROBOTS FOR THE MICROFACTORY

Zhong Yang

April 21, 2023

Future assembly technologies will involve higher levels of automation in order to satisfy increased microscale or nanoscale precision requirements. Traditionally, assembly using a top-down robotic approach has been well-studied and applied to the microelectronics and MEMS industries, but less so in nanotechnology. With the boom of nanotechnology since the 1990s, newly designed products with new materials, coatings, and nanoparticles are gradually entering everyone's lives, while the industry has grown into a billion-dollar volume worldwide. Traditionally, nanotechnology products are assembled using bottom-up methods, such as self-assembly, rather than top-down robotic assembly. This is due to considerations of volume handling of large quantities of components, and the high cost associated with top-down manipulation requiring precision. However, bottom-up manufacturing methods have certain limitations, such as components needing to have predefined shapes and surface coatings, and the number of assembly components being limited to very few. For example, in the case of self-assembly of nano-cubes with an origami design, post-assembly manipulation of cubes in large quantities and cost-efficiency is still challenging.

In this thesis, we envision a new paradigm for nanoscale assembly, realized with the help of a wafer-scale microfactory containing large numbers of MEMS microrobots. These robots will work together to enhance the throughput of the factory, while their cost will be reduced when compared to conventional nanopositioners. To fulfill the microfactory vision, numerous challenges related to design, power, control, and nanoscale task completion by these microrobots must be overcome.

In this work, we study two classes of microrobots for the microfactory: stationary microrobots and mobile microrobots. For the stationary microrobots in our microfactory application, we have designed and modeled two different types of microrobots, the AFAM (Articulated Four Axes Microrobot) and the SolarPede. The AFAM is a millimeter-size robotic arm working as a nanomanipulator for nanoparticles with four degrees of freedom, while the SolarPede is a light-powered centimeter-size robotic conveyor in the microfactory. For mobile microrobots, we have introduced the world's first laser-driven micrometer-size locomotor in dry environments, called ChevBot to prove the concept of the motion mechanism. The ChevBot is fabricated using MEMS technology in the cleanroom, following a microassembly step. We showed that it can perform locomotion with pulsed laser energy on a dry surface. Based on the knowledge gained with the ChevBot, we refined tits fabrication process to remove the assembly step and increase its reliability. We designed and fabricated a steerable microrobot, the SerpenBot, in order to achieve controllable behavior with the guidance of a laser beam. Through modeling and experimental study of the characteristics of this type of microrobot, we proposed and validated a new type of deep learning controller, the PID-Bayes neural network controller.

The experiments showed that the SerpenBot can achieve closed-loop autonomous operation on a dry substrate.

TABLE OF CONTENTS

LIST OF TABLES

LIST OF FIGURES

And you shall know the truth, and the truth shall make you free.

John 8:32

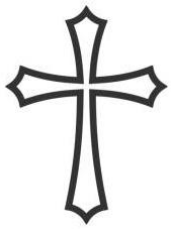

CHAPTER 1 INTRODUCTION

1.1 Motivation

This research focuses on the design, modeling, simulation, and control of MEMS devices with micro-factory applications. The micro/nano structure formation can be done in two approaches: top-down and bottom-up approach. The top-down approach is normally through standard cleanroom procedures, micromachining, or microassembly. The bottom-up approach normally can be found in biological processes such as DNA, RNA, and protein formation.

The micro-factory is a future technology which is inspired by the top-down approach. Its advancement aims to automate manufacturing at the nano scale using swarm microrobots that can transport, process, and assemble nanoscale objects, such as: carbon nanotubes, nanowires, nanospheres, and so on. Our envisioned microfactory is a wafer-scale factory which works in the Scanning Electron Microscope (SEM) and includes several kinds of microrobots: the mobile (or locomotive) microrobot and the articulated (or fixed) microrobot. Locomotive microrobots are working as micro/nano particles as carriers and transporters to the working space of the articulated microrobots, while the articulated microrobots are utilizing those micro/nano particles as raw materials to assemble them to be larger scale micro/nano structures.

Because the size limitation, the power delivery and control method of the microrobots are a serious bottleneck. From an energy and control point of view, in general, the microrobots can be classified as Type-R (Remote-powered) and Type-E (Energy-harvesting) microrobots. Type-E microrobots can harvest and store energy from the environment as the microrobot has a control unit on it. On the other hand, Type-R microrobots also can harvest energy from the environment but they have neither energy storage nor a control unit on-board (Figure 1-2).

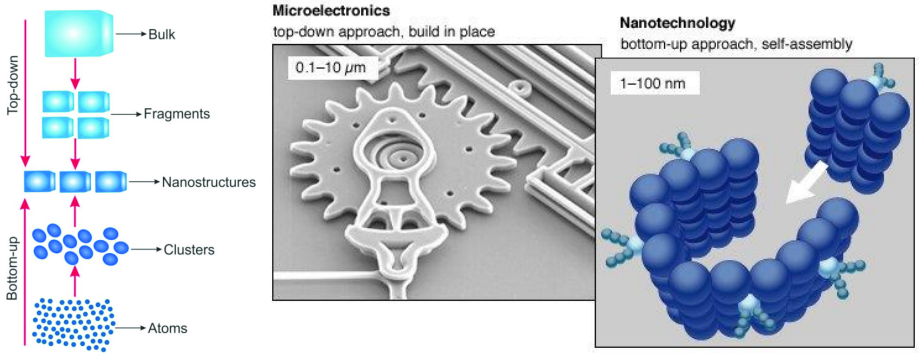

Figure 1-1 Top-down and bottom-up approach for micro/nano structure. [1-2]

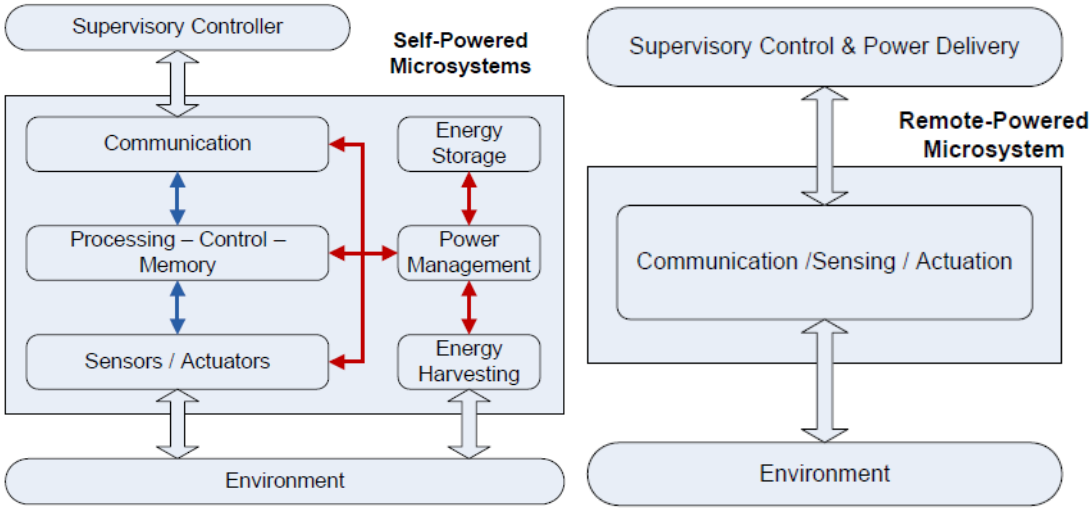

Figure 1-2 (Left) Self-powered microsystem paradigm with energy harvesting, Type-E, (Right) remote-power and control paradigm for microrobots, Type-R.

In our microfactory application, the vision is to use laser or white light as the energy source for powering the microrobot. The light also could be modulated as a control signal for the swarm microrobot. The advantage of using modulated light is it generates a programmable environment and delivers plenty of power even at small scales. This remote powering scheme can simplify the connections and system complexity and is suitable to miniaturization.

1.2 Challenges

Microrobotics is a cross disciplinary research area, including mechanical system design, Multiphysics system modeling and simulation, optical system design, cleanroom processes and fabrication, as well as measurement and control system design. In our research, there are several challenges that we addressed.

1) Challenges in fabrication of MEMS

The microfactory application requires quality consistency in making the microrobots, the factory infrastructure. Typically, fabrication processes for Microelectromechanical Systems (MEMS) have defects driven by low aspect ratio limits. Due to stacking on errors in assembled MEMS mechanisms, microrobots fabricated from MEMS parts (gears, motors, transmissions) suffer from large tolerances relative to their size.

2) Challenge in modeling

MEMS devices and microrobots operate through complex Multiphysics phenomena which are difficult to model. Considering the limited experimental validation, and data acquisition, and so on at the micro scale is hard to precisely measure the numerous

physics parameters such as coefficients associated with temperature, force, displacement, absorption, and vibration phenomena. Furthermore, friction, stiction, and other surface forces dominate, and their models may not be similar to those used at the macro scale. Therefore, basic assumptions must be made leading to simplification of both models and boundary conditions.

3) Challenges in control

Due to limited fabrication precision of their components, microrobots have vastly different properties during operation. In addition, environmental disturbances are very significant due to dry-environment operation (stiction, friction, and surface contamination and particles, etc.) As a result, designing robust controllers to guarantee microrobot precise operation is challenging. Typically reduced-order robot models must be individually identified for each microrobot.

4) Challenges in integration/powering

Due to limited sizes of batteries, sensors, and controllers, microrobots are typically powered from ambient energy sources, rather than from on-board energy storage. This makes extremely challenging to manage power consumption during operation and obtain sensory feedback for closed-loop control.

1.3 Research Activities

In this thesis we studied three microrobots for the future Microfactory:

1) The Articulated Four-Axis Microrobot (AFAM) is a multi-DOF MEMS manipulator with mm-size and nanometer motion resolution. AFAM is a type E tethered microrobot that performs pick and place operations in the microfactory, akin a miniature robotic manipulator.

2) The SolarPede is a Type E mobile microrobot powered by light energy harvested through a solar cell. SolarPede is a cm-size legged micro-crawler with MEMS assembled legs and an electronic backpack that can achieve nanoscale motion resolution and 3 DOFs of positioning in the wafer plane.
3) The ChevBot and SerpenBot are Type R mobile microrobots powered by laser beams. They are sub-mm in size and use different types of thermal MEMS actuators as legs to achieve forward and steering motion, which is dependent on laser pulse frequency or selective radiation. The modeling, simulation, and controller for this type of microrobots have been developed, which is the main topic of this thesis.

This work proposes simulation models for guiding the design and control of these microrobots. The models investigated include multi-physics lumped dynamic models, reduced-order kinematic models and steady state/transient Finite Element Models. These models have been validated experimentally, using microrobots designed and fabricated in the cleanroom.

For AFAM, I derived forward and inverse kinematic models for this parallel microrobot using a constrained optimization approach. These models were implemented using a C++ programming framework within the Robot Operating System (ROS) and visualized during operation. Inverse kinematic models were then used to control the AFAM tip motion during a cooperative manipulation sequence with a carbon nanotube. In the future we intend to use AFAM use inside the Scanning Electron Microscope (SEM).

For SolarPede, I have created lumped dynamic models for the microrobot legs and body and implemented them in MATLAB®. These models were used to predict the effect

of various gaits of the microrobot legs and were experimentally validated using a prototype configured as a conveyor.

For ChevBot, I performed both theoretical and experimental analyses. Using the knowledge gained from ChevBot, I proposed a novel microrobot powered by laser, the SerpenBot. I designed novel thermal actuators to serve as the SerpenBot's legs, which enabled controlled gaits on a Silicon substrate. Two modeling methods were used to gain insight into the SerpenBot, including an analytical model and a FEA model. For the analytical model, dynamic lumped and kinematic-dynamic hybrid models were created using MATLAB and Python code. For FEA simulation, an ANSYS model was created to refine the microrobot design. Microrobots were then fabricated in the UofL MNTC cleanroom, using a new fabrication method involving two-step photolithography and DRIE processes. The experiments verified that the SerpenBot has controllable steering behavior. A new concept for controller design, a Neural Network (NN) PID-Bayes controller, was then implemented to achieve 3DoF motion in the plane for SerpenBots while powered by Nd: YAG laser. Theoretical proof showed that the PID-Bayes controller is stable around equilibrium points, and experiments showed that this new type of controller can control the SerpenBot's movement from its initial configuration to its goal configuration.

1.4 Contributions

1) I proposed a parallel kinematic model for a closed-chain, flexible, mm-scale microrobotic arm, called AFAM (Articulated Four Axes Microrobot), which is capable of computing both forward and inverse kinematics. The model was formulated as a constrained optimization problem and was solved numerically using an efficient algorithm that was implemented in simulation.

2) I proposed a novel Thermo-Mechanical Multiphysics, multi-body dynamic model for SolarPede, a novel type-E laser-driven, 8-legged microrobot. The model was used to simulate gait patterns and motion trajectories of the microrobot in XY plane. I then formulated a simplified dynamic model for SolarPede and developed automatic test programs to experimentally validate this microrobot operating under an Optical Microscope.
3) I proposed a novel Opto-Thermo-Mechanical Multiphysics model for laser-drive Type-R microrobots ChevBot and SerpenBot – the first of their kind. These models include lumped ordinary differential equation (ODE) models, validated using Finite Element Analysis (FEA) and direct experiments in our lab. These models confirm that the microrobot design containing a body, one or two legs, and a dimple can achieve locomotion on a dry substrate under remote laser power.
4) I designed, simulated, and experimentally validated SerpenBot, a Type-R microrobot that is powered by a laser. I investigated the control parameters using both differential resonance to pulse laser and laser beam selective irradiation methods to steer the microrobot. The experiments showed that the laser beam selective irradiation method was more stable for control purposes.
5) I developed a new fabrication method for SerpenBot microrobots to increase their reliability and repeatability. In the older method, the bodies, and dimples of the microrobots had to be fabricated separately and then assembled using UV glue through a microassembly process. In the new method, I developed two-step process involving photolithography and Deep Reactive Ion Etching (DRIE) to directly

fabricate the dimples on top of the microrobot's body. This streamlined the fabrication process and eliminated the need for a separate assembly step.

6) I formulated novel control algorithms based on Deep Neural Networks for system identification and control of SerpenBot. Once learned, these models were used to control the motion of the SerpenBot from the initial configuration to the final goal configuration. The controller steers the microrobot by using the selective radiation method with different laser beam center offsets relative to the center of the SerpenBot. These algorithms were experimentally validated in our lab using a novel laser/stage/microscope setup.

As a result of my research, the following papers were published in International Conference Proceedings and Journals:

- Z. Yang and D. O. Popa, "A General Kinematic Modeling Framework for a 3D Compliant Micromechanism," 2018 International Conference on Manipulation, Automation and Robotics at Small Scales (MARSS), Nagoya, 2018, pp. 1-6, doi: 10.1109/MARSS.2018.8481221.
- J. F. Klotz et al., "Concept Validation for a Novel Stick-and-Slip, Light-Powered, Mobile Micro-Crawler," 2019 International Conference on Manipulation, Automation and Robotics at Small Scales (MARSS), Helsinki, Finland, 2019, pp. 1-7, doi: 10.1109/MARSS.2019.8860938.
- Zhang, R., Klotz, J.F., Wei, D. et al. SolarPede: a stick-and-slip, light-powered, Mobile micro-crawler. J Micro-Bio Robot 16, 1–12 (2020).
- R. Zhang, A. Sherehiy, D. Wei, Z. Yang, M. N. Saadatzi and D. O. Popa, "Tracking Experiments with ChevBot: A Laser-Actuated Stick-Slip Microrobot," 2019

International Conference on Manipulation, Automation and Robotics at Small Scales (MARSS), Helsinki, Finland, 2019, pp. 1-6, doi: 10.1109/MARSS.2019.8860947.

- R. Zhang, A. Sherehiy, Z. Yang, D. Wei, C. K. Harnett, and D. O. Popa, "ChevBot – An Untethered Microrobot Powered by Laser for Microfactory Applications," 2019 International Conference on Robotics and Automation (ICRA), Montreal, QC, Canada, 2019, pp. 231-236, doi: 10.1109/ICRA.2019.8793856.
- Z. Yang et al., "Multiphysics Dynamic Model Validation Methodology for Laser-Driven Microrobots," 2019 IEEE 15th International Conference on Automation Science and Engineering (CASE), Vancouver, BC, Canada, 2019, pp. 1555-1561, doi: 10.1109/COASE.2019.8843032.
- Z. Yang et al., "Design, Fabrication and Experimental Validation of a Steerable, Laser-Driven Microrobot in Dry Environments," 2020 EEE 16th International Conference on Automation Science and Engineering (CASE), Hong Kong, China
- Z. Yang *et al.*, "SerpenBot, a Laser Driven Locomotive Microrobot for Dry Environments using Learning Control," *2022 International Conference on Manipulation, Automation and Robotics at Small Scales (MARSS)*, Toronto, ON, Canada, 2022, pp. 1-6, doi: 10.1109/MARSS55884.2022.9870255.
- Chowdhury, SS, Yang, Z, Clapacs, PW, & Popa, DO. "Untethered Microrobots with Serpentine Actuators: The Role of Elastics Point Contact & Laser Beam Shape on Their Locomotion." Proceedings of the ASME 2021 16th International Manufacturing Science and Engineering Conference. Volume 2: Manufacturing Processes; Manufacturing Systems; Nano/Micro/Meso Manufacturing; Quality and Reliability. Virtual, online. June 21–25, 2021. V002T08A008. ASME.

- Zhong Yang, Moath Alqatamin, Andriy Sherehiy et al. Learning Control of a Laser-Driven Locomotive Microrobot for Dry Environments, 22 December 2022, PREPRINT (Version 1) available at Research Square

1.5 Thesis Organization

The thesis document is organized as follows:

Chapter 2 provides a review of current research activities in the field of microrobotics, including locomotive microrobots and micromanipulators.

Chapter 3 discusses the articulated microrobot, AFAM. We present the forward and inverse kinematics models through an optimization method and implemented a simulation platform for the articulated microrobot. We also discuss the modeling of SolarPede and experimental test platform with experimental data.

Chapter 4 introduces the first-generation Laser Driven Locomotive Microrobot (LDLM), also named ChevBot, and presents a systematic method for modeling this type of microrobots.

In Chapter 5, we discuss the design and implementation of a new LDLM, SerpenBot, inspired by the knowledge obtained from the previous chapter. We also validate SerpenBot through experiments.

Chapter 6 discusses the controller design for SerpenBot. We propose novel control algorithms based on deep learning to move SerpenBot from the initial configuration to the final goal configuration by steering the microrobot with a selective radiation method using different laser beam center offsets relative to the center of the SerpenBot.

Finally, Chapter 7 presents conclusions and discusses future work.

CHAPTER 2 BACKGROUND

2.1 Microfactory

Microfactory is a new concept of a manufacturing method. It's been unveiled since the 1990s from the Japanese National Micromachine Project. [3] Compared to the traditional manufacturing process, through miniaturized device and manufacturing process, the microfactory has several different advantages.

First, the microfactory is ecofriendly. The miniature device and manufacturing process can save energy, space, and materials. It also can reduce pollution to the environment such as: acoustical noise, heat, and wastes. Second, the microfactory technology can achieve economic efficiency since the device size becomes smaller, the cost per unit from production can be reduced while achieving portable, scalable, reconfigurable, and agile manufacturing. Third, because of the smaller size, the moving range of the actuators of the microfactory is also reduced. This leads the microfactory to achieve precision and productivity from the manufacturing process. Finally, due to the smaller size of the manufacturing process, it's becoming a good platform for medical application, education or personal user applications. [4]

In 1991, the Ibaraki team introduced the first concept of the desktop system of microfactory. The system has a Precision Assembling Unit, Machining and Pre-assembling Unit and Parts Supply Unit. The AFM tip has been utilized as a manipulator during the micro assembly process. The whole system is controlled by a desktop computer.[3] In 1996,

the Mechanical Engineering Laboratory (MEL) developed the first microlathe system with a numerical control system. The whole system power consumption is less than 1 W.[5-7] In 2003, Dr. Codourey designed a desktop Cleanroom as the microfactory for the fabricating microsystem. The minienvironment inside the microfactory has been controlled by the particles and contaminations.[8] The past works of our lab, we have introduced the concept of Wafer-Size Robotic Microfactory, depicted in Figure 2-1. This microfactory has combined different types of microrobots to achieve transport, sorting and assembly of micro or nano particles.[15][43][45][46]

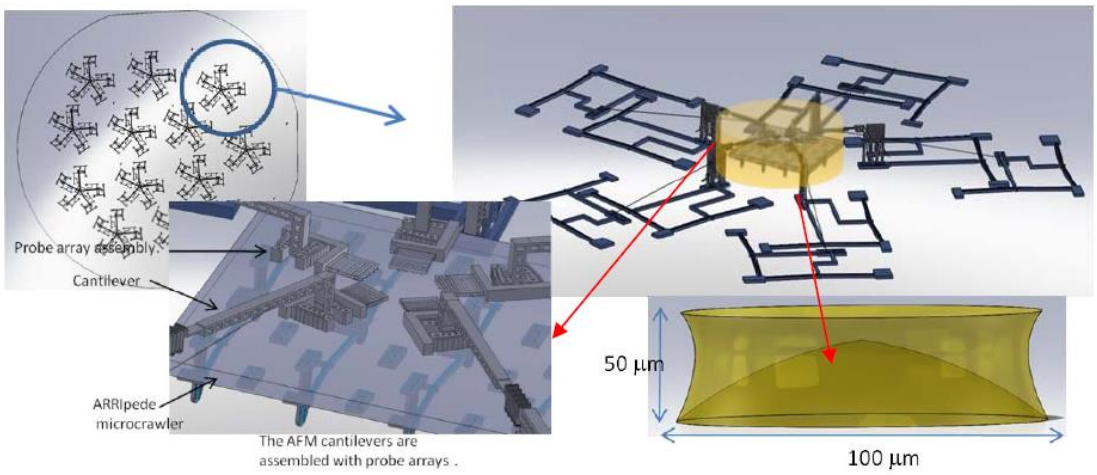

Figure 2-1 Wafer-size microfactory.

2.2 Microrobots

The microrobots in our microfactory can be classified as Mobile (Locomotive) Microrobots and Stationary (Fixed) Microrobots. The Locomotive Microrobots are working as micro/nano particles carriers, and they can transfer those tiny particles to other microrobots' working space. The Stationary Microrobots include two types of microrobots: microconveyor and micromanipulator. The microconveyor, like Locomotive Microrobots,

is part of the transportation system on the microfactory. When those micro/nano particles transported to the working space of those Micromanipulator, then those Articulated Microrobots assemble them to be desired micro/nano structures. In this section, we will discuss those microrobots in detail.

2.2.1 Stationary Microrobots

2.2.1.1 Micromanipulator and AFAM

Precision robots have been widely used in manufacturing applications over the last two decades, in particular for operation inside microfactories or at the nano scale [36-39]. Such robots have been configured in multi-degree-of freedom microassembly stations for 3D manipulation of sub-millimetric components, such as Micro Electromechanical System (MEMS). Microassembly technology using microgrippers provides the ability to measure, manipulate, and assemble micro and nano scale components to make even smaller autonomous robots. Some of these examples are discussed below.

In [40], researchers have integrated a robotic manipulator with a MEMS microgripper. The robot manipulator has five axes that provide $0.1\ \mu m$ motion resolution on the translation axes and 0.36° on the rotational axes. The microgripper is attached via solder onto contacts mounted on the robot tip. The microgripper can open and close a grasper by thermal resistive actuation.

In [41], researchers have developed another microgripper tool for micromanipulation. They have achieved $0.45 \pm 0.24\ \mu m$ accuracy of the system for the assembly of photonic crystals. Electrostatic actuation was selected for the design of the microgripper, due to better temperature control of adhesion forces, and higher bandwidths.

In [13], researchers designed parallel micromanipulation techniques based on magnetic levitation and photo-thermal SU-8 microgripper which can achieve 13.2 μm accuracy. They used electromagnets to generate a magnetic field in order to levitate and control the microrobot, then use photo-thermal effects to drive the gripper fingers. The microrobot has a permanent magnet for following the maximum magnetic field point of the levitation field and an actuated polymeric (SU-8) microgripper. In this example, the microrobot is operated as a system free of electrical wiring.

In [42] researchers have introduced so-called programmable force fields to achieve micromanipulation. This solution is implemented by massively parallel arrays of thermal and electrostatic microactuators. When the motion of actuators is controlled, the array of actuators will generate different force fields to position microobjects.

In [45] the research team have provided a method combined magnetic and acoustic method, the traditional magnetic method has narrow stable margin while acoustic method is hard to achieve parallel handling and object orientation control, the combination of this method can achieve manipulate objects in complex environment with precision, stable and flexible behavior.

Despite considerable progress in recent years, satisfying precision requirements for robots operating at the nano scale is still challenging. In order to manipulate nanoscale objects, the Atomic Force Microscope (AFM) has traditionally been used as a manipulator and imaging system, while the Scanning Electron Microscope (SEM) is often employed as a high precision imaging system. Although these tools can achieve high resolution of imaging, they have limited manipulation dexterity, and are slow and expensive to operate.

For instance, during the operation, the AFM needs to change state between sensing and manipulation [49-50].

Over the last two decades, new types of compliant microrobots have also been demonstrated. In [51] a CMOS and MUMPS material and fabrication process was used to for multi-articulated microrobots; [52] proposed a multi-degrees of freedom (DOF) articulated microrobot called "sc-AFM," which uses electro-thermal actuation to drive the motion of a cantilever for scanning the sample surface; in [53], a piezoelectric driven, flexible, parallel, millimetric robot called milliDelta was introduced.

In recent years, some novel micro manipulations mechanisms have been proposed. The uncontacted method has become popular in the research field, since those manipulation methods won't damage or bring contaminations to the sample, they have widely applied it in the biological research area. In [31][55][56], the optical tweezers have been developed and utilized as uncontacted micro particle manipulation method. In [57], research has utilized Magneto-Acoustic field to operation micro particles in 3D space with high dexterity.

The reference [54] utilize capillary effect as gripper to pick up and release submillimeter objects. The gripper first step is capturing the microdrop of liquid, then using this liquid capture the microparticle, through the joule effect to evaporate liquid the microparticle will get released.

During the last decade, our research group has also introduced news type of mm-scale microrobots for nanoscale positioning applications. The aim of the AFAM (Articulated Four Axes Micro) robot was to provide a system a positioning and assembly tool with the ability to push, pull, bend, twist, cut, pick, and place, position, orient and

assemble nano scale objects like carbon nanotubes, silicon nanowires, nanoparticles and colloids, supra-molecules, etc. [46]. The ultimate goal of the AFAM is an entire nanofactory with thousands of such units operating in parallel [45].

The Articulated Four Axes Microrobot (AFAM) features four degrees of freedom (DOF), $3 \times 1.5 \times 1\ mm$ overall dimensions, two Chevron actuator-controlled planar positioners and a copper wire-controlled arm [46]. The robot introduced several years ago, was constructed via 3D microassembly from 50 or 100 μm Silicon on Insulator (SOI) wafers.

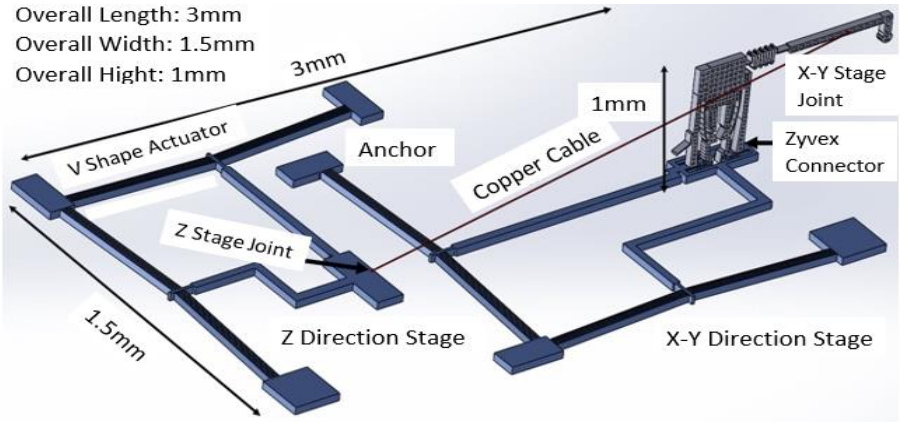

Figure 2-2 Articulated Four Axis Microrobot (AFAM), illustration [49].

As shown in Figure 6-1, the AFAM consists of two *XY* thermally driven coupled stages, an assembled arm mounted on one of the *XY* stages using the Zyvex snap-fastener [48], and a "glued" copper wire to pull the end-effector. The assembled arm contains a 2-dimensional torsional joint with tunable stiffness. By actuating the four Chevron actuators in a controlled way, the end-effector generates pitch and yaw direction motions due to the 2D compliant arm joint.

The AFAM is a MEMS device, with well-established fabrication and assembly processes. As a result, the motion of AFAM joints is not independent, rather, the kinematics of the robot is highly coupled and nonlinear. Hence, the traditional robot methodology of modeling such as using DH parameters is difficult to apply for these classes of robots. In this paper, we introduce a novel, scalable modeling framework based on constrained compliant energy minimization for a class of 3-dimensional microrobots composed of pseudo-rigid links and compliant joints. Such models can be used prior to microrobot fabrication to evaluate mechanism dexterity, precision, and sensitivity to dimensional tolerances. They can also be used for microrobot visualization, control synthesis and for fast parametric optimization. We exemplify our approach by modeling the forward and inverse kinematics of the AFAM, and use the models to analyze the microrobot workspace, repeatability, and plan complex tip motions in preparation for future operation. A library written in the robot operating system (ROS) [44] was used for robot visualization and motion planning.

The fabrication process for the AFAM has 15 steps, all based on standard cleanroom process using Deep Reactive Ion Etching (DRIE) in 50 or 100 μm Silicon on Insulator (SOI) wafers device layer [40]. After fabrication, the MEMS components are assembled using a passive "jammer" end-effector using a multi-manipulator assembly station. The mounting and connection of the arm through the Zyvex snap-fastener requires a microassembly accuracy of approximately 4 μm. [43]

2.2.1.2 Microconveyor and SolarPede

The microconveyor is a novel microrobot in the microfactory application. The microconveyor system can move a larger range than the locomotive microrobots. Hence,

the microconveyor is utilized as micro-positioning or transportation system in the microfactory. The popular design of microconveyor is using a piezoelectric actuator to drive a linear stage. The Physik Instrumente (PI) company has commercialized this type of microconveyor system. [25] In [26], people have utilized arrays of piezoelectric devices to generate the ultrasound to be an uncontacted micro conveyor system. In [27], people have proposed a matrix of multilayer of serpentine coils to generating modulated magnetic fields as the mechanism of microconveyor system.

The original design of SolarPede is a Type-E locomotive micororobot. However, in our microfactory application, it can be configured as a microconveyor mode. The SolarPede is a die size ($1 \times 1\ cm$) holonomic micro-crawler with 8 legs, and it can move in *X-Y* direction. Each leg of SolarPede is driven by Chevron Thermal Actuator (CTA) through joule heat from electricity. The energy of the SolarPede is harvesting from environmental light through solar cells, and the micro-battery can be utilized for energy storage. When we configure the microrobot on the position up-side-down and add an extra die as linear stage on the top of the SolarPede leges, the SolarPede is working as a microconveyor system. The micro/nano particles can be placed on the linear stage to transport to the working space of other microrobots.

2.2.2 Locomotive Microrobots

Microrobotics has received a lot of attention in the last few decades due to a myriad of applications in medicine such as drug delivery, cell injection, surgery, etc., and in nanotechnology, such as nanomanipulation, characterization of new materials and microscopy. Several research groups have studied locomotion mechanisms for microrobots based on harvesting ambient fields to produce controlled motion on the micro and

nanoscales. These fields include electrostatic, magnetic, electromagnetic, laser and ultrasonic vibration energy delivered to mobile agents with sizes below 1 mm. Microrobot fabrication is based on Integrated Circuit (IC) and Micro Electromechanical System (MEMS) technology.

From our former discussion, the microrobots have two different types: Type-R and Type-E. We can utilize this classification method to summarize former researcher's works. Work in [9-12] exploit magnetic fields for moving and operating microrobots as Type-R units. Work in [13] proposes using an electromagnetic field to levitate the microrobot, while actuate the microgripper with laser beam, and this microrobot can be classified as a Type-R microrobot. Researchers at Harvard [14] designed a Type-E microrobot based on piezoelectric actuator, for which the actuation energy is from a carried battery. In [15] the Type-E microrobot also powered by a battery and actuated by an electrothermal actuator. Furthermore, Robo-Fly from University of Washington [16] was designed by harvesting laser energy for actuating piezoelectric actuators as a classic Type-E microrobot.

2.2.2.1 ChevBot

In past work in our lab, R. Zhang introduced a novel Type-R microrobot, the ChevBot (Figure 2-3) [17,18]. ChevBot is a laser-driven locomotor which is able to navigate through an operating surface following desired trajectories. Our paper [17] saw the first introduction of the concept of modulated laser pulse frequency to control the behavior of the microrobot, and this behavior was predicted using simulations. In [18] the ChevBot was designed using a Chevron Thermal Actuator (CTA) and was fabricated by standard MEMS cleanroom process on the Silicon on Insulator (SOI) wafers. A $532\ nm$ Nd: YAG laser beam was used for both driving and controlling the ChevBot's velocity.

When the laser spot focuses on the CTA, the thermal expansion is generated, while kinematic constraints of the actuator convert the thermal expansion to displacement of a shuttle containing a microassembled dimple. This microassembled dimple generates a stick and slip motion on a dry, Silicon substrate. Although the ChevBot can locomote on a dry substrate, it is not able to steer and follow trajectories in 3 degrees of freedom (DOF). Because it had only one actuator, the motion of the ChevBot was typically uni-directional, and the robot was turning unpredictably depending on substrate surface conditions.

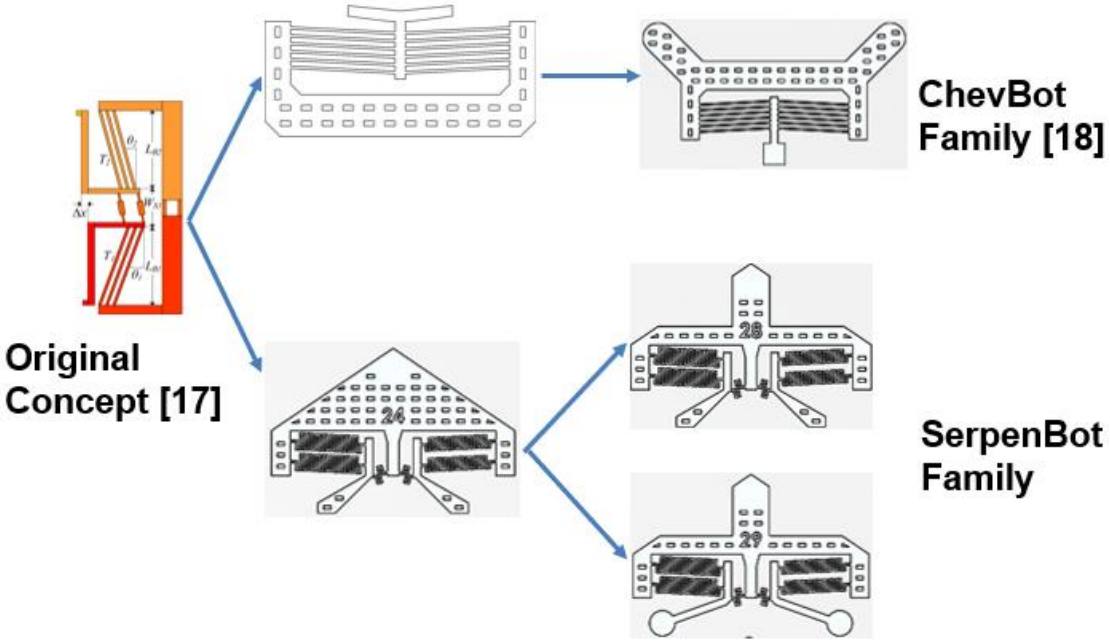

Figure 2-3 Families of Laser-Driven Microrobot including ChevBot and SerpenBot.

2.2.2.2 SerpenBot

The ChevBot has proved the concept of Laser Driven Locomotive Microrobot (LDLM). However, this type of microrobot doesn't have the controllable behavior over its steering. To deal with this issue, we need to design a new mechanism to let the microrobot be steered under the same fabrication and experimental condition as the ChevBot. In this

thesis, we will introduce a new laser-driven microrobot, the SerpenBot, with serpentine-like actuators and leg designs that allow controllable turning motions in addition to forward and backward velocities when we modulate laser pulse in a different repeat frequency. We discuss the novelties of the microrobot design, present simulation and analysis of its predicted behavior, and experimental validation demonstrating steerable trajectories on a Silicon substrate. Experimental results reported here show that the SerpenBot is capable of velocities up to $68\ \mu m/s$, and angular velocities of $3.8°/s$ while turning left and right.

CHAPTER 3 MODELS FOR AFAM AND SOLARPEDE

In this chapter, we will discuss another stationary microrobot for our microfactory application. The AFAM is an articulated microrobot with 4 DOF microscale robotic arm for nano/micro-scale assembly in our proposed wafer-size microfactory model. AFAM motion analysis is realized using Forward Kinematic (FK) and Inverse Kinematic (IK) models including the trajectory planning method.

3.1 AFAM Kinematic Modeling

In this section, we discuss the kinematic modeling of AFAM, with applicability to a broader class of compliant microrobots, in particular those composed of pseudo-rigid links and flexible joints.

3.1.1 Constrained Optimization Problem

Kinematic models for microrobots like the AFAM can be formulated as a constrained optimization problem, with a number of control inputs - actuator displacements, outputs - the robot tip pose, and constraints - the length of rigid links in the mechanism. The principle of minimum joint elastic energy can be used as an optimization index to obtain both forward and inverse kinematic solutions.

Define an input control value space $X \in \mathbb{R}^n$, the pose of the robot end-effector in Cartesian space $Y \in \mathbb{R}^6$, and the position of other joints of the mechanism $Z \in \mathbb{R}^m$. To model the robot, we wish to find the forward kinematics (FK) mapping $g : X \to Y \times Z$, or

its inverse kinematics (IK) $g^{-1}: Y \to X \times Z$, while satisfying link length constraints and minimizing mechanism elastic energy. If the joint variable space is denoted by $\Theta = (\Theta_1, \Theta_2, \dots \Theta_3) \in \mathbb{R}^p$ and Θ is also the function of X, Y and Z. For instance, Θ could be the displacement of the angular, stretch or compression motion of the mechanism joint springs. We can find an energy objective function $f(\Theta)$ to minimize under pseudo-rigid length conditions and other constraints on the inputs or outputs of the robot $h(X, Y, Z) = 0$.

$$\begin{gathered} minimize\ f(\Theta) = \frac{1}{2}\sum_{i=1}^{p} K_i \theta_i^2\ , \\ subject\ to\ h(X, Y, Z) = 0, \end{gathered} \tag{3-1}$$

in which K_i is the i-th robot joint stiffnesses constant. To solve this problem, we introduce Lagrange multipliers λ for both the FK and IK problems. The solution for the FK problem will be computed given control values X, so that Y and Z are the variables by minimizing $L(X, Y, Z, \Theta, \lambda) = f(\Theta) - \lambda \cdot h(X, \mathrm{Y}, \mathrm{Z})$. The problem becomes solving the nonlinear equation:

$$\begin{cases} \nabla_{Y,,Z,\lambda} L(X, Y, Z, \Theta, \lambda) = 0 \\ h(X, Y, Z) = 0 \end{cases}, \tag{3-2}$$

in which $\nabla_{Y,Z,\lambda} = \left[\frac{\partial}{\partial Y_i}, \frac{\partial}{\partial Z_j}, \frac{\partial}{\partial \lambda_k}\right]^T, i = 1, \dots, 6; j = 1, \dots, m; k = 1 \dots n$ is gradient operator.

A similar optimization problem can be formulated for the inverse kinematics, in which Y is given, and X, Z are the variables.

3.1.2 Constrained Optimization Problem Formulation for AFAM

In the case of AFAM, a number of mechanism simplifications and assumptions need to be made to obtain appropriate kinematic equations:

The motions of two stages of AFAM are independent. The motion of *XY* micro-positioners of AFAM are coupled together physically, but they have been designed with

minimal crosstalk, leading to a relatively small cross-axis motion relative to the size of the thermal actuator.

Several joints of the AFAM can be considered rigid, others are free to rotate, while the arm joint is a 2D spring which can be modeled by two revolute joints with known compliance.

The cable which links the XY micro-positioner bank 1 and the assembled arm is stiff, so that it can be considered rigid during the microrobot operation.

Figures 3-1 and 3-2 depict the geometry of AFAM from top and side views. Let the control space be defined as $X = (x_1, y_1, x_2, y_2) \in \mathbb{R}^4$, where $x_\mathrm{i}, y_\mathrm{i}, i = 1{,}2$ is the displacement of micro-positioner, i expressed in a global frame aligned with the substrate of the robot. The end-effector arm tip position is $Y = (x, y, z) \in \mathbb{R}^3$, if we do not control the microrobot orientation. Furthermore, there are other points of interest on the body of the robot such as a middle control point $Y_b = (x_b, y_b, z_b) \in \mathbb{R}^3$,pivot point $Y_r = (x_r, y_r, z_r = h_0) \in \mathbb{R}^3$, since h_0 is a constant, and arm . If we combine these variables as $Z = (x_r, y_r) \in \mathbb{R}^2$, and $Y = (x_b, y_b, z_b) \in \mathbb{R}^3$, then we are interested in finding FK maps $g_1 : X \to Z$ and $g_2 : Z \to Y$. After finding these maps, we will also locate the tip position (x, y, z) and (x_t, y_t, z_t) of AFAM using additional geometric transformations.

The only joint angle $\Theta \in \mathbb{R}$ with non-zero compliance is located at the pivot point and consists of a 2D pitch (α) and yaw (β) angles of the microrobot arm as depicted in Figure 3-1 and 3-2. This decomposition can be obtained by projecting the arm onto the $x - y$ and $x - z$ planes of the global frame. Theta, alpha and beta depend on X, Y and Z. Since $p = 1$, the minimization of potential energy at the pivot point can be written as minimizing the joint angle, or alternatively, maximizing $cos(\theta)$. Since $cos(\theta)$ is the dot product

between the microrobot arm direction and the $(1, 0, 0)$ direction, this problem reduces to maximizing $x_t - x_2 - x_{c2}$, and consequently maximizing $x_b - x_2 - x_{c2}$ subject to cable and arm length constraints, where x_2 is the displacement of the second micropositioner along the x direction, from its equilibrium position x_{c2}.

For the FK problem, equation (3-2) can be written and solved in terms of unknown variables $Y = (x_b, y_b, z_b)$ in Figure 3-2. Then the microrobot tip position (x, y, z) will be derived from Z and Y. The FK problem will be solved for every input X, while the IK problem can be solved for every output Y as:

$$\begin{aligned} &minimize \quad x_b - x_2 - x_{c2} \\ &subject\ to\ h(X, Y, Z) = 0 \end{aligned}. \tag{3-3}$$

3.1.3 Detailed Kinematic Model for AFAM

In last section, we have formulated the constrained optimization problem of AFAM, which we can now derive in detail. Referring to Figure 3-2, a distance constraint from point (x_b, y_b, z_b) to point $(x_1 + x_{c1}, y_1 + y_{c1}, 0)$ (AFAM cable length is constant) is written as:

$$[x_b - (x_1 + x_{c1})]^2 + [y_b - (y_1 + y_{c1})]^2 + z_b^2 = l_0^2. \tag{3-4}$$

A distance constraint from point (x_b, y_b, z_b) to point $(x_r, y_r, z_r = h_0)$ (AFAM arm length is constant) is written as:

$$(x_b - x_r)^2 + (y_b - y_r)^2 + (z_b - h_0)^2 = b_0^2. \tag{3-5}$$

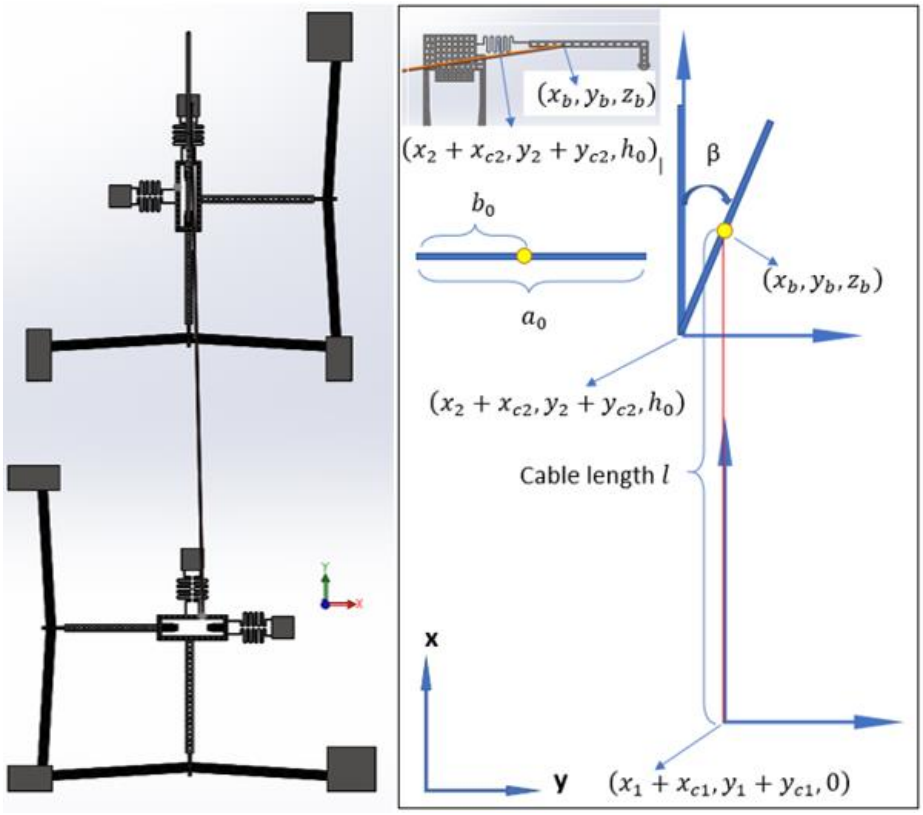

Figure 3-1 Top view diagram of the AFAM and definition of dimensional microrobot variables, in which the _c subscript denotes constant global coordinates.

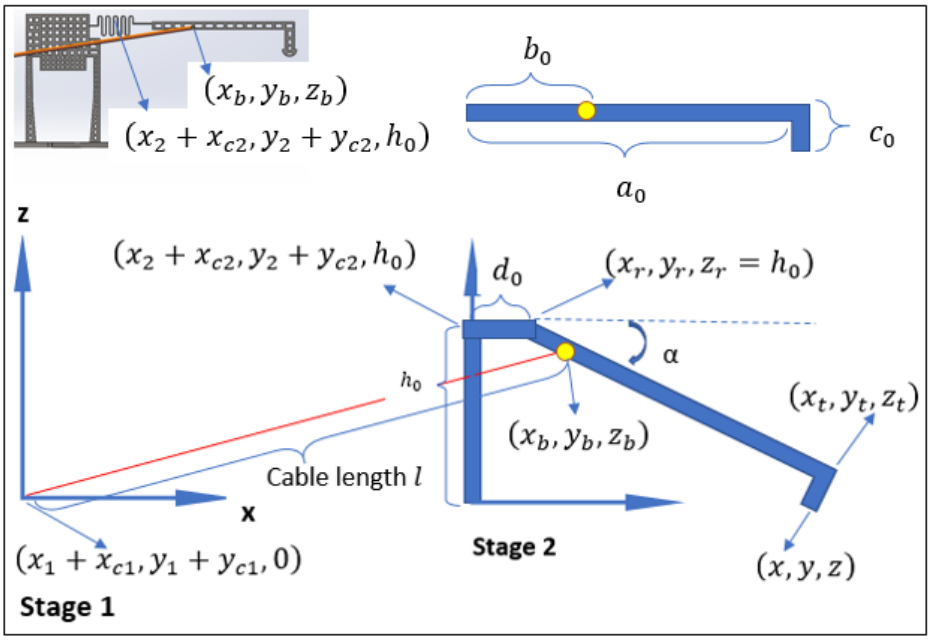

Figure 3-2 Side view diagram of the AFAM and definition of dimensional microrobot variables, in which the _c subscript denotes constant global coordinates.

A distance constraint from point $(x_r, y_r, z_r = h_0)$ to $(x_2 + x_{c2}, y_2 + y_{c2}, h_0)$ (AFAM flexible link length is constant) is written as:

$$[x_r - (x_2 + x_{c2})]^2 + [y_r - (y_2 + y_{c2})]^2 = d_0^2. \quad (3\text{-}6)$$

An additional constraint of the arm plane yaw motion, can be derived by requiring that the cross product of vectors, $(x_r - (x_2 + x_{c2}), y_r - (y_2 + y_{c2}), 0)$ and $(x_b - x_r, y_b - y_r, z_b - h_0)$, be perpendicular to z axis:

$$[(x_r - (x_2 + x_{c2}), y_r - (y_2 - y_{c2}), 0) \times (x_b - x_r, y_b - y_r, z_b - h_0)] \cdot [0 \quad 0 \quad 1] = 0$$

$$\begin{vmatrix} \vec{\imath} & \vec{\jmath} & \vec{k} \\ x_r - (x_2 + x_{c2}) & y_r - (y_2 + y_{c2}) & 0 \\ x_b - x_r & y_b - y_r & z_b - h_0 \end{vmatrix} \cdot [0 \quad 0 \quad 1]$$

$$= \big(x_r - (x_2 + x_{c2})\big)(y_b - y_r) - (x_b - x_r)\big(y_r - (y_2 + y_{c2})\big) = 0$$

Finally, this constraint becomes:

$$\big(x_r - (x_2 + x_{c2})\big)(y_b - y_r) - (x_b - x_r)\big(y_r - (y_2 + y_{c2})\big) = 0. \quad (3\text{-}7)$$

Equations (3-5) -(3-8) impose 4 constraints on the robot kinematics. As described in Section 3.1.1, the optimization problem can be written in terms of the function $f(x_b, x_2) = x_b - (x_{c2} + x_2)$. Using the Lagrange Multiplier method, an additional 5 equations can be written with four λ multipliers from equation (3-2):

$$1 - \lambda_1\big[2\big(x_b - (x_1 + x_{c1})\big)\big] - \lambda_2[2(x_b - x_r)] + \lambda_4\big[\big(y_r - (y_2 + y_{c2})\big)\big] = 0, \quad (3\text{-}8)$$

$$0 - \lambda_1\big[2\big(y_b - (y_1 + y_{c1})\big)\big] - \lambda_2[2(y_b - y_r)] - \lambda_4\big[\big(x_r - (x_2 + x_{c2})\big)\big] = 0, \quad (3\text{-}9)$$

$$0 - \lambda_1(2z_b) - \lambda_2[2(z_b - z_r)] = 0, \quad (3\text{-}10)$$

$$0 + \lambda_2[2(x_b - x_r)] - \lambda_3\big[2\big(x_r - (x_2 + x_{c2})\big)\big] - \lambda_4\big[(y_b - y_r) - \big(y_r - (y_2 + y_{c2})\big)\big] = 0, \quad (3\text{-}11)$$

$$0 + \lambda_2[2(y_b - y_r)] - \lambda_3\big[2\big(y_r - (y_2 + y_{c2})\big)\big] + \lambda_4\big[\big(x_r - (x_2 + x_{c2})\big) +$$

$$(x_b - x_r)\big] = 0. \tag{3-12}$$

Therefore, the robot forward kinematics reduces to solving nonlinear equations(3-4)-(3-12) for 5 unknowns (x_b, y_b, z_b), $(x_r, y_r, z_r = h_0)$, and four λ multipliers, given incremental actuator displacements(x_1, y_1, x_2, y_2). The robot inverse kinematics reduces to solving for actuator displacements (x_1, y_1, x_2, y_2) and the arm joint center point $(x_r, y_r, z_r = h_0)$ given middle control point (x_b, y_b, z_b).

Furthermore, we can find the actual tip position (x, y, z) from x_b, y_b, z_b by considering further geometry constraints.

The relation between (x_r, y_r, z_r), (x_b, y_b, z_b) and (x_t, y_t, z_t) is linear, and can be written as:

$$x_t = x_r + \frac{a_0}{b_0}(x_b - x_r), \tag{3-13}$$

$$y_t = y_r + \frac{a_0}{b_0}(y_b - y_r), \tag{3-14}$$

$$z_t = z_r + \frac{a_0}{b_0}(z_b - z_r). \tag{3-15}$$

A dot-product constraint equation can be written in terms of the perpendicular vectors $(x_b - x_r, y_b - y_r, z_b - h_0)$and $(x - x_t, y - y_t, z - z_t)$ as:

$$(x_b - x_r)(x - x_t) + (y_b - y_r)(y - y_t) + (z_b - h_0)(z - z_t) = 0. \tag{3-16}$$

A constraint equation in terms of vectors $(x_b - x_r, y_b - y_r, z_b - h_0)$ and $(x - x_t, y - y_t, z - z_t)$ can also be written such that their planar motion always occurs in a plane perpendicular to the substrate, written as:

$[(x_b - x_r, y_b - y_r, z_b - h_0) \times (x - x_t, y - y_t, z - z_t)] \cdot [0 \quad 0 \quad 1] = 0$, or

$$\begin{vmatrix} \vec{\imath} & \vec{\jmath} & \vec{k} \\ x_b - x_r & y_b - y_r & z_b - h_0 \\ x - x_t & y - y_t & z - z_t \end{vmatrix} \cdot [0 \quad 0 \quad 1] = 0. \tag{3-17}$$

Equation (3-18) can be rewritten as:

$$(x_b - x_r)(y - y_t) - (x - x_t)(y_b - y_r) = 0. \tag{3-18}$$

Finally, a third constraint can be written as the constant distance between tip coordinate (x, y, z) to coordinate of the middle arm control point (x_b, y_b, z_b):

$$(x - x_b)^2 + (y - y_b)^2 + (z - z_b)^2 = (a_0 - b_0)^2 + c_0^2. \tag{3-19}$$

Solving for unknown tip position (x, y, z) requires solving nonlinear equations (3-16), (3-18), and (3-19) using an unconstrained solver such as the Newton's method.

The inverse kinematics of the AFAM can be posed and solved in a similar manner. Given a new tip location of AFAM (x, y, z), use equations (3-13)-(3-19) to find $Y = (x_b, y_b, z_b)$, and $Z = (x_r, y_r, z_r = h_0)$. Then solve equations (3-3) to find $X = (x_1, y_1, x_2, y_2)$ subject to microrobot cable and arm constraints. In this case, the partial derivatives of the Lagrange function with respect to x_1, y_1, x_2, y_2, are:

$$0 - \lambda_1\left[2\left(x_b - (x_1 + x_{c1})\right)\right] = 0, \tag{3-20}$$

$$0 + \lambda_1\left[\left(y_b - (y_1 + y_{c1})\right)\right] = 0, \tag{3-21}$$

$$-1 + \lambda_2\left[2\left(x_r - (x_2 + x_{c2})\right)\right] + \lambda_3(y_b - y_r) = 0, \tag{3-22}$$

$$0 + \lambda_2\left[2\left(y_r - (y_2 + y_{c2})\right)\right] + \lambda_3(x_b - x_r) = 0. \tag{3-23}$$

3.1.4 Numerical Solver

To solve equations (3-4) -(3-23) for both forward and inverse kinematics, we used the Newton-Raphson method, employing the pseudo-inverse Jacobian matrix, implemented numerically. In general, a constrained kinematic model for flexible

microrobots can be viewed as a set of M multi-variable functions $f_i(x)(i = 1, \dots M)$ of the state variable $x = (x_1, x_2, \dots, x_N)$, written in vector form:

$f(x) = [f_1(x_1, \dots, x_N), \dots, f_M(x_1, \dots, x_N)]^T$, $y = f(x)$, with Jacobian matrix:

$$J_f(x) = \begin{bmatrix} \frac{\partial f_1(x_1,\dots,x_N)}{\partial x_1} & \cdots & \frac{\partial f_1(x_1,\dots,x_N)}{\partial x_N} \\ \vdots & \ddots & \vdots \\ \frac{\partial f_M(x_1,\dots,x_N)}{\partial x_1} & \cdots & \frac{\partial f_M(x_1,\dots,x_N)}{\partial x_N} \end{bmatrix}, \tag{3-24}$$

A classical iterative Newton-Raphson iteration starts from a solution approximation x_k, and iterates on it with the help of the Jacobian pseudoinverse as shown in Algorithm 3-1, NR-Solver:

Algorithm 3-1: NR-Solver (x_0, y)

---

set initial point $x_k = x_0$ (*where* $x_k \coloneqq (x_k^1, \dots, x_k^N)$ *and* $x_0 \coloneqq (x_0^1, \dots, x_0^N)$)
set relative error $err = \infty$

while $err > error\_tolerance$ **do**

Step 1: Calculate $y = f(x_k)$
$where\ f(x_k) = [f_1(x_k^1, \dots, x_k^N), \dots, f_M(x_k^1, \dots, x_k^N)]^T$;
Step 2: Numerically calculate Jacobian matrix $J_f(x_k)$;
Step 3: Iterate on the next solution
$x_{k+1} = x_k - hJ_f^{\#}(x_k)f(x_k)$, *in which* $J_f^{\#}$ *denotes the Jacobian pseudo-inverse, and h is a small step size.*
Step 4: Calculate relative error $err = \frac{x_{k+1} - x_k}{x_k}$;
end while

3.2 Motion Planning and Analysis of AFAM

In this section, we use the IK and FK solvers previously described to plan motions for the AFAM tip and also visualize the robot during operation.

3.2.1 Trajectory Generator

When given initial location of AFAM tip $Y_0 = (x_0, y_0, z_0)$, corresponding to input vector coordinates X_0, and a desired end location $Y(t) = (x, y, z)$, we plan motions along a line trajectory between Y_0 and $Y(t)$ using a linear planner that generates via points on a line in Cartesian Space. The parametric form of a line in 3D with step t can be written as:

$$Y(t) = Y_0 + t \cdot d, \tag{3-25}$$

where $d = [a \quad b \quad c]^T$ is the direction vector between the stand and end tip positions. By incrementing small motion steps t we can generate via points along the line while simultaneously solving the IK problem as shown in Algorithm 3-2, Linear Planner (LP):

Algorithm 3-2: LP $(Y_0, X_0, Y(t))$

---

set initial end point $Y = Y_0$*;*
set initial robot joint vector $X = X_0$*;*

while $\|Y(t) - Y\| > error\_tolerance$ **do**

$Y = Y + t_{step} \cdot \vec{d}$;

call $X = NR\text{-}Solver(X, Y)$;

end while

call $X = NR\text{-}Solver\big(X, Y(t)\big)$;

We tested our kinematic solver and linear planner to generate a tip motion trajectory consistent to nano-object pushing. A visualization interface was written using the ROS/RViz framework [44] and was made publicly available [35].

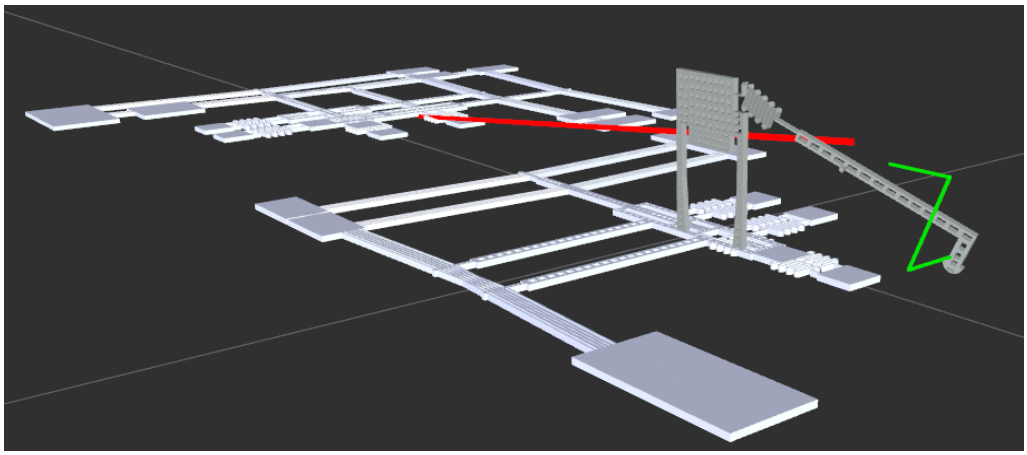

Figure 3-3 Visualization environment for AFAM based on RViz, showing the microrobot tip trajectory in green for planning Algorithm 3-2.

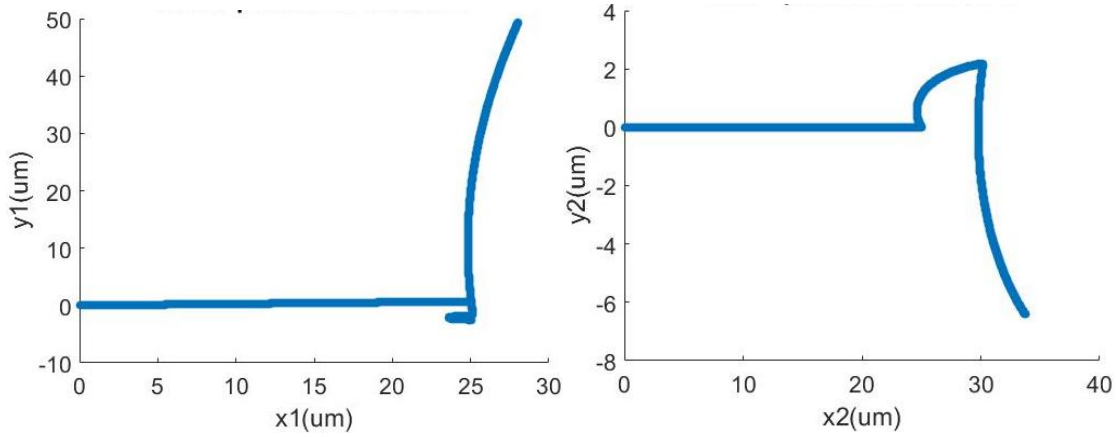

Figure 3-4 Trajectories in XY plane of compliant MEMS stages (1-top) and 2 (2-bottom), computed to generate the 3D tip trajectory in Figure 3-4. Dimensions are in microns.

A sample of the resulting trajectories and robot poses are shown in Figure 3-3. The corresponding X, Y motions on the Chevron actuator bank micropositioners are shown in Figure 3-4.

3.2.2 Workspace, Uncertainty, and Parameters Analysis

As a second application of our FK solver, we derived the tip positional uncertainties by running forward kinematics solution over an input space of 9 dimensional and 4 control

parameters. Since, AFAM is fabricated using cleanroom MEMS technology and then assembled, we have extensive information about the errors inherent in its fabrication process.

Five basic types of errors are introduced in the robot: fabrication (using the Deep Reactive Ion Etching DRIE) errors in the range of $5\ \mu m$, assembly errors in the range of $10\ \mu m$, cable cutting errors in the range of $100\ \mu m$, and electrothermal actuator stage motion control errors in the order of $10\ nm$. There are also errors involved in approximating the joint spring structure of the AFAM arm as two single DOF joints. These errors are reflected in the dimensional bounds depicted in Table I. We were interested in how these uncertainties propagate through the robotic chain to the AFAM tip.

TABLE I: AFAM FABRICATION PARAMETER UNCERTAINTY BOUNDS

Parameter Name	Nominal size (μm)	Manufacturing Method	Error bound (μm)	Simulation Levels
a_0	1610	DRIE	±5	3
c_0	315	DRIE	±5	3
d_0	346.830	approximation	±10	3
h_0	1252	assembly	±10	3
l_0	7580	cable cutting	±50	21
x_{c1}	-6538.861	DRIE+assembly	±15	7
y_{c1}	-214.721	DRIE+assembly	±15	7
x_{c2}	0	DRIE+assembly	±15	7
y_{c2}	0	DRIE+assembly	±15	7

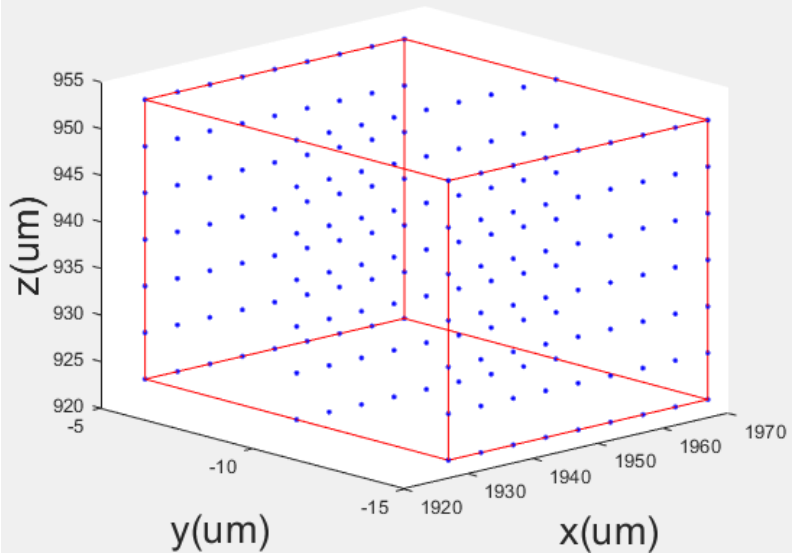

Figure 3-5 AFAM tip uncertainty in cartesian space due to robot fabrication and assembly errors in Table I. Units on the axes are in μm. These errors can be compensated by robot calibration.

For each parameter we used a $5\ \mu m$ or $10\ \mu m$ size increment, which results in varying parameter refinements, from 3 levels of uncertainty in most cases, to 20 levels of uncertainty for the cable since it introduced most errors. In total, we ran $3^5 \times 7^5 = 4.08M$ Monte Carlo runs to evaluate the uncertainty bounds for the microrobot tip. These simulations run for approximately 45 minutes on a high end I-7 Quad Core Intel Computer to generate results depicted in Figure 3-6, showing a resulting tip uncertainty bounding box of $20\ \mu m \times 40\ \mu m \times 30\ \mu m$ in size.

Secondly, by varying the actuator inputs x_1, y_1, x_2, y_2 in their nominal range (0-50 μm), and resolution (0-10 nm) we obtained the actuator workspace and repeatability by running an additional 10^4 simulation runs in each case. Results are depicted in Figures 3-6 and 3-7.

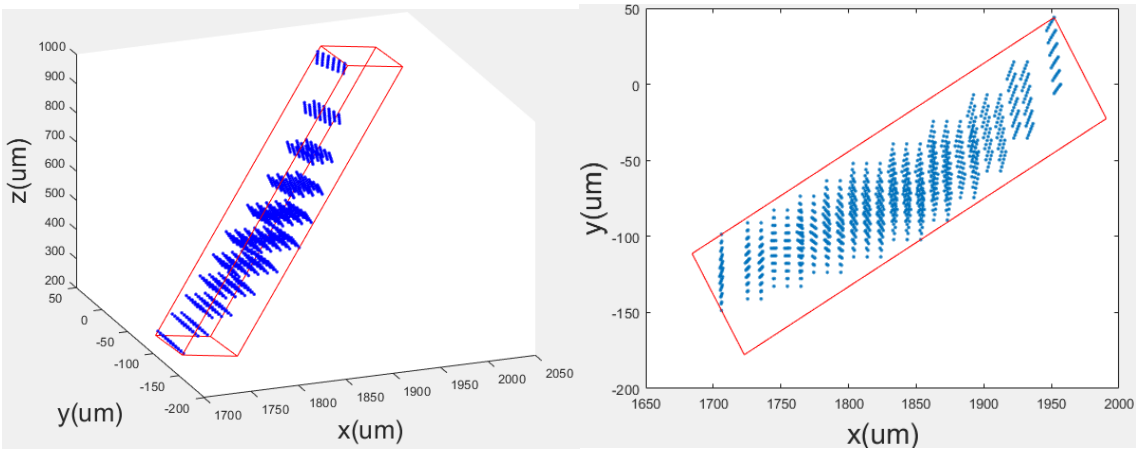

Figure 3-6 AFAM tip cartesian workspace and corresponding projection on X-Y (horizontal) plane. The workspace is enclosed in a parallelepiped approximately $50\ \mu m \times 50\ \mu m \times 800\ \mu m$ *in size.*

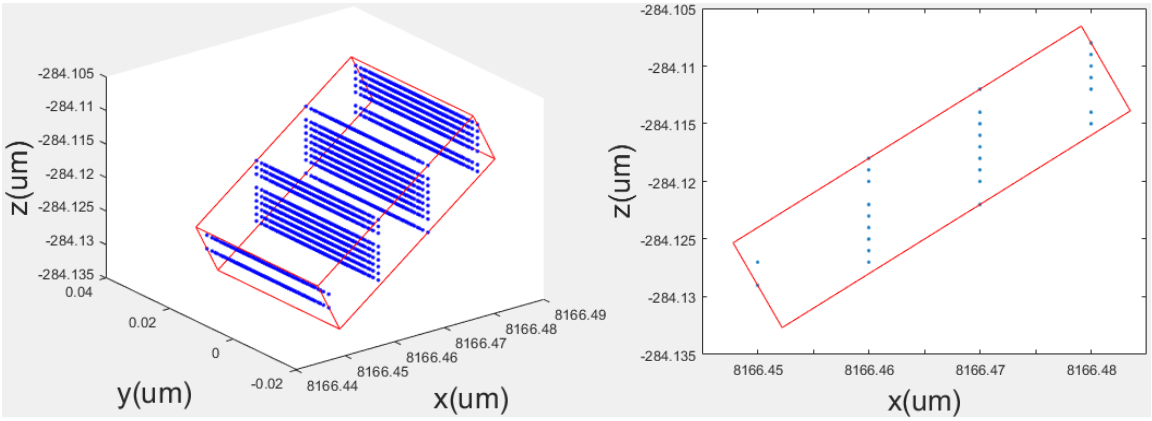

Figure 3-7 AFAM tip repeatability around the joint coordinate origin and corresponding projection on X-Z (vertical) plane. Results are enclosed in a parallelepiped approximately $40\ nm \times 5\ nm \times 20\ nm$.

3.4 SolarPede Modeling

The thermal actuator heating-cooling cycle and thermal expansion can be used for the first order differential equation described [24]. Considering the electrical thermal effect in frequency domain, we can use first order low pass filter system function described the force output from voltage input.

The SolarPede has 4 legs, each leg driving by two Chevron Thermal Actuator, hence, each leg has contributed 2 Degree of Freedom (DOF) (*X-Y* in plan motion), so the system will need at least 8 differential equations. The SolarPede legs and actuators arrangement is shown in Figure 3-8. Considering each leg is supplying the force to the body, those differential equations will highly couple together to be a nonlinear system. So, to avoid simulation complexity, we can use a simplified mode to explain the behavior of the SolarPede.

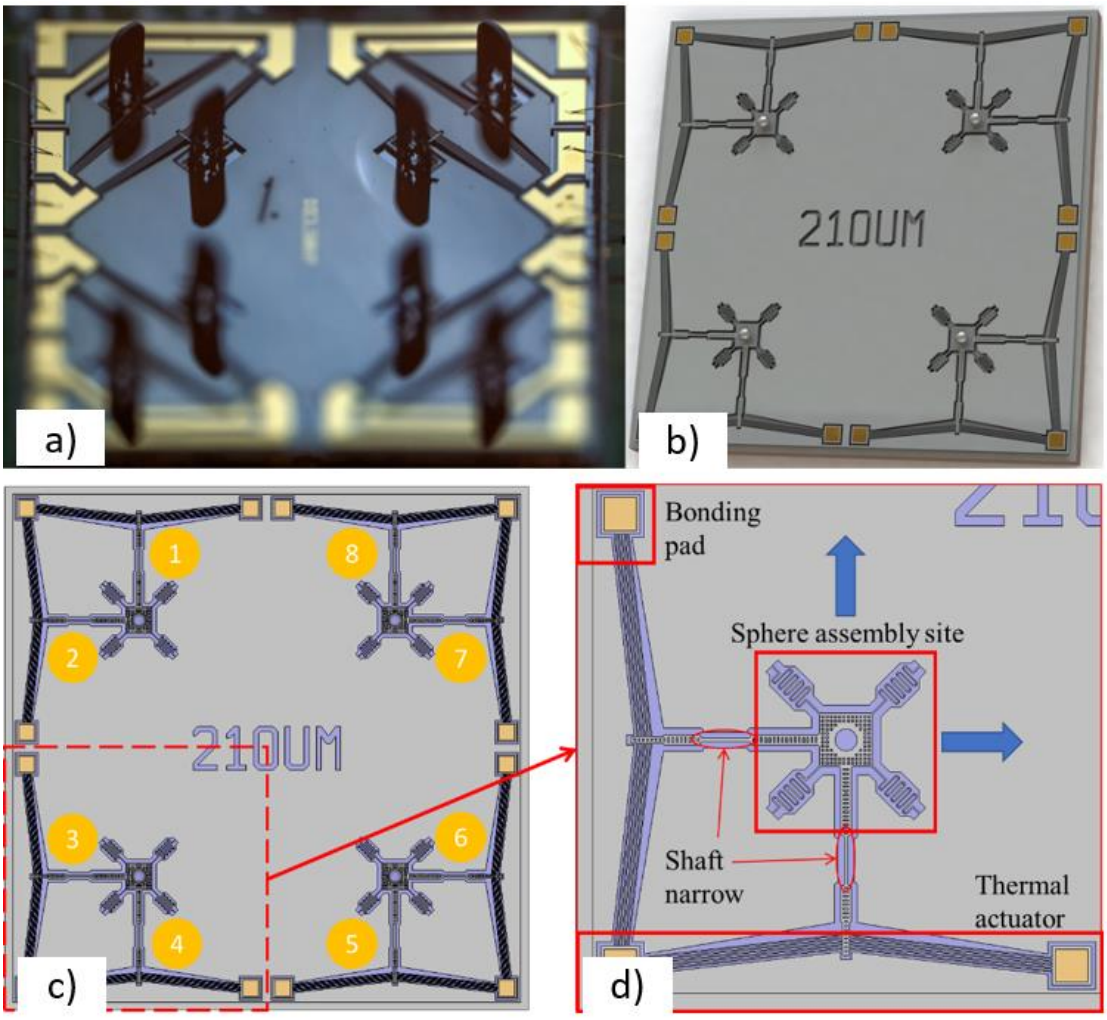

Figure 3-8 The SolarPede design and legs arrangement. The legs can have different designs, in a) the leg is the original fabricated leg design, for minimize the micro-assembly complexity, later design shown in b, c, d) are using micro-balls to replace the original design.

.

Assuming the robot is moving in y direction, and the robots 4 sets of legs supply the force labeled in the graph, each of the forces can be described in the 1D model we have derived, in general, the summation of the force is:

$$\sum F = F_1 + F_2 + F_3 + F_4. \tag{3-26}$$

The total moment of the body is:

$$\sum M = I_M \ddot{\varphi} = r_1 \times F_1 + r_2 \times F_2 + r_3 \times F_3 + r_4 \times F_4, \tag{3-27}$$

where $F_1, F_2, F_3,$ and F_4 are the forces on the legs, $r_1, r_2, r_3,$ and r_4 are the position vectors of the forces, I_M is the moment of inertia, $\ddot{\varphi}$ is the angular acceleration, $\sum F$ is the net force and $\sum M$ is the net torque, the Freebody diagram is shown in Figure 3-9.

Since the Chevron Thermal Actuator can be equivalent to be the Mass-Spring-Damper model by described as second order differential equations, combining the solution of this model in frequency domain with the empirical of the fraction force and actuator structural factors, the final driving force on each leg can be approximated as

$$F_a(V, f, t) = \frac{2NAEsin^2(\theta)}{L} \cdot \frac{\lambda V^2}{1+s\frac{f}{f_{BW}}} + sgn(t) \cdot \mu Mg \tag{3-28}$$

where $N = 6$ is the beam number of Chevron Actuator, E is the Young's modulus of Silicon, $\theta = 3.4°$ is the beam bent angle, A is the cross-sectional area of the beam combine together, V is the input voltage, f is input frequency, f_{BW} is bandwidth of the mechanical system, λ is an empirical constant, μ is coulomb friction coefficient and switching between static friction μ_s and dynamic friction μ_d in the stick and slip motion, M is the weight of the SolarPede load. We have simulated the motion of the SolarPede, with different input voltage, frequency, and friction force constants. The result is shown in Figure 3-10.

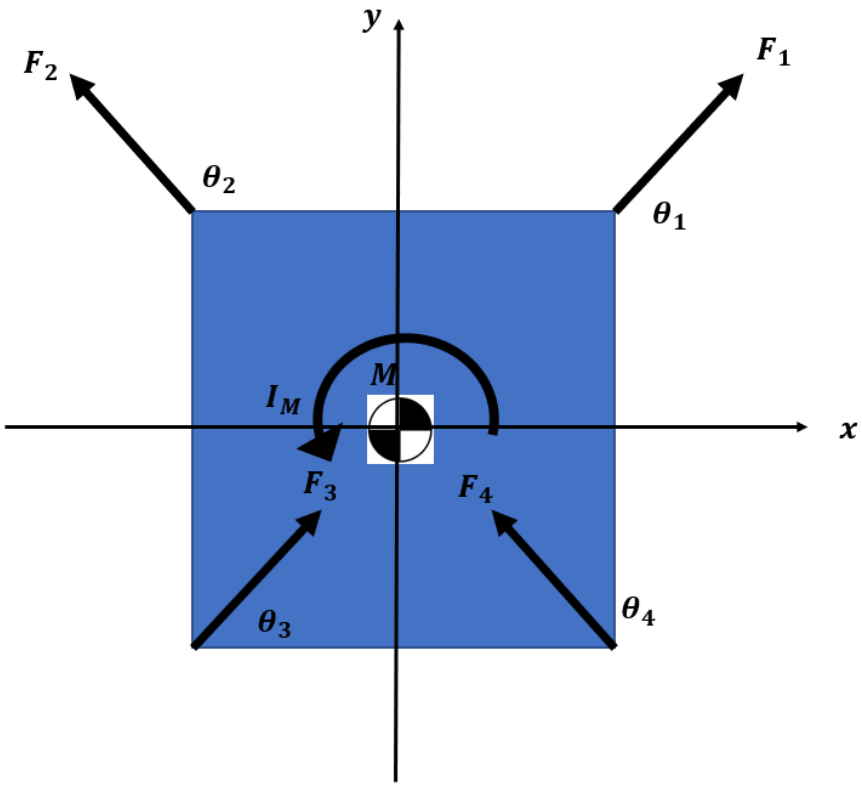

Figure 3-9 Freebody diagram of SolarPede.

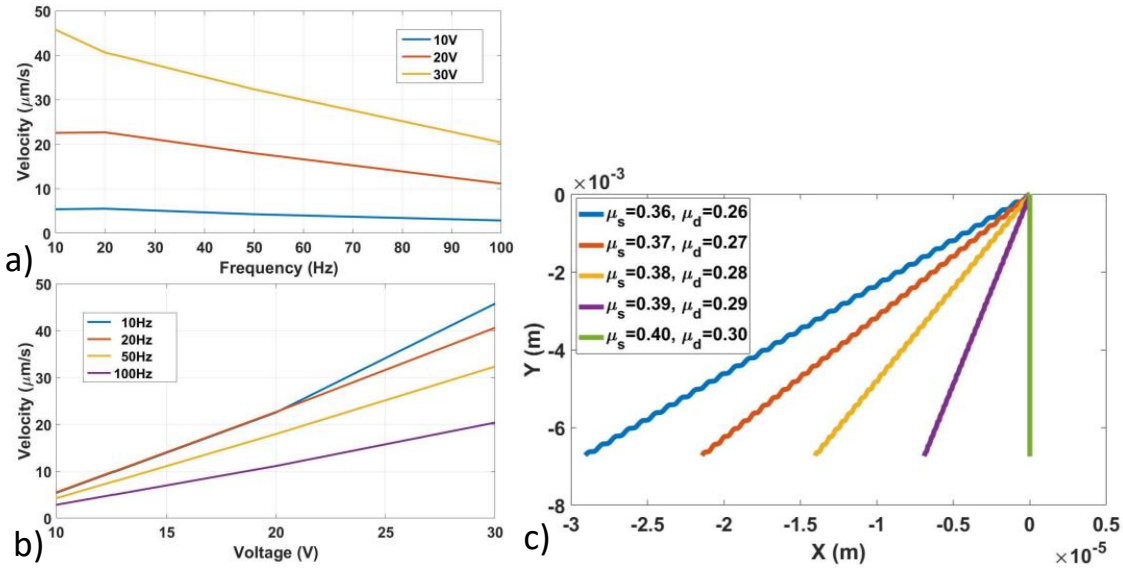

Figure 3-10 Simulation result of SolarPede of different input a) voltage, b) frequency and c) leg friction constants.

3.3 Summary

In this chapter we have given the modeling method for AFAM, and we have simulated in the ROS simulation environment. Through this simulation environment, we have studied the properties of AFAM. Later we can utilize that knowledges to design a better mechanical structure of AFAM and combine the hardware to implement the close loop controller for it.

The SolarPede originally is a Type-E locomotive microrobot. In our microfactory application, the SolarPede has been configured as a stationary microrobot, microconveyor system. In this chapter we will discuss the simplified modeling method and given the simulation results to show the possible control parameters for later controller design.

CHAPTER 4 MODELS FOR CHEVBOT, A LASER DRIVEN MOBILE MICROROBOT

The contribution of this chapter is to put forth a comprehensive methodology for constructing lumped opto-thermo-mechanical models of laser-driven microrobots. An experimental data collection system was used to automate the process of laser power delivery to the microrobots and perform system identification while tracking the robot motion. Simulation results using Finite Element Methods were used to compare the operating performance and the thermal time constant of ChevBots in two different operating conditions: one in which the robots are tethered to the MEMS substrate, and one in which they freely move on the 2D substrate. Experimental motion profiles collected with a laser range sensor were used to validate the dynamics of actuation and construct reduced order models of the CTA. A 1D dynamic model of ChevBot was then proposed and tuned to experimentally collected data. The model was then extended in 2D to study the expected motion of the robot under varying friction conditions. In future work, such models can be used for microrobot design optimization, as well as closed-loop control synthesis.

4.1 Robot Description and Locomotion Principe

The ChevBot is a MEMS-based microrobot, fabricated from a silicon-on-insulator (SOI) wafer with 20 μm device layer, to which as microassembled dimple is added using a microassembly system located in our lab. As shown in Figure 4-1, ChevBots consist of four components, namely a body frame, the CTA actuator, a set of "feet", and the assembled dimple under the frame. Conventional CTAs are powered by voltage or current

sources and generate thermal expansion and mN-size forces by Joule heating. In our microrobot, the actuator is powered directly from a laser beam, which can be focused on a part or on the whole robot. In the first case, it may be possible to locally affect the temperature gradient in selected parts of the microrobot, while in the latter case, it will be easier for the laser beam to track the robot while in motion.

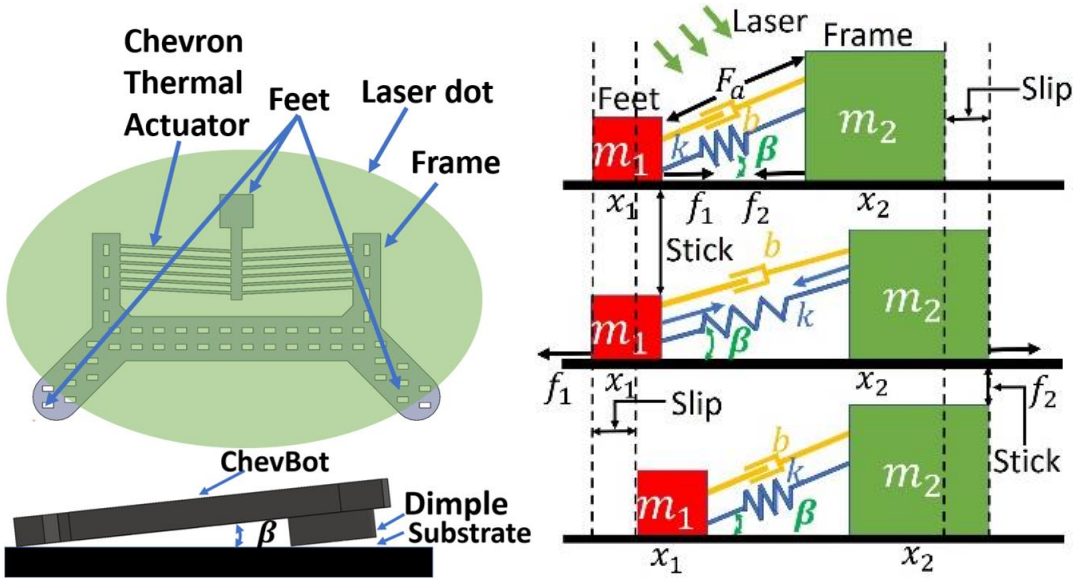

Figure 4-1 (Left) Top and side view of an untethered ChevBot fabricated from a 20 µm device layer SOI substrate. The scale bar is 100 µm. (Right) Free Body Diagram of ChevBot explaining the stick-slip actuation cycle from pulsed laser beam.

As the CTA absorbs energy from laser beam, it generates thermal expansion, which, when combined with a stick-slip motion of the feet will create locomotion on a flat substrate.

In a typical design and fabrication process detailed in [18], ChevBots measured approximately $750\ \mu m$ in width and $425\ \mu m$ in length, and with an assembled dimple, its total thickness is $40\ \mu m$. Each of the 12 beams in the CTA is $5\ \mu m$ wide and they form an acute angle θ with the body frame. In Figure 4-1, the green ellipse represents the laser spot

with large waist diameter of 800 μm and small waist diameter of 600 μm, corresponding to the experimental conditions After the dimple is assembled, the ChevBot is inclined by a small angle β to the substrate, and moves according to a stick and slip cycle induced by the pulsed laser beam. The inner edge of the rectangular-shaped dimple and the tail act as three contact edges to the substrate.

In the "laser on" part of the actuation cycles the body/dimple sticks to the substrate due to static friction conditions, while the feet slip via CTA actuation. In the "laser off" part of the actuation cycle, caused by variations in the robot tilt angle β, the feet stick to the substrate, while the body slips creating a net velocity.

4.2 Opto-Thermal-Mechanical Models

Modeling the ChevBot is a Multiphysics problem, in which an energy transfer process is initiated when laser is focused onto the CTA. Laser energy is absorbed in the robot frame and actuator, and converter into heat. Directional thermal expansion on the actuator will generate the driving force and displacement on the microrobot feet and dimple. Then, static, and dynamic friction/stiction forces will lead to stick-slip locomotion. The resulting Opto-Thermal-Mechanical process is shown in Figure 4-2, in which the three conversion components, and their corresponding physical phenomena and boundary conditions are indicated. The figure also depicts the thickness of various layers involved in the associated heat transfer problem.

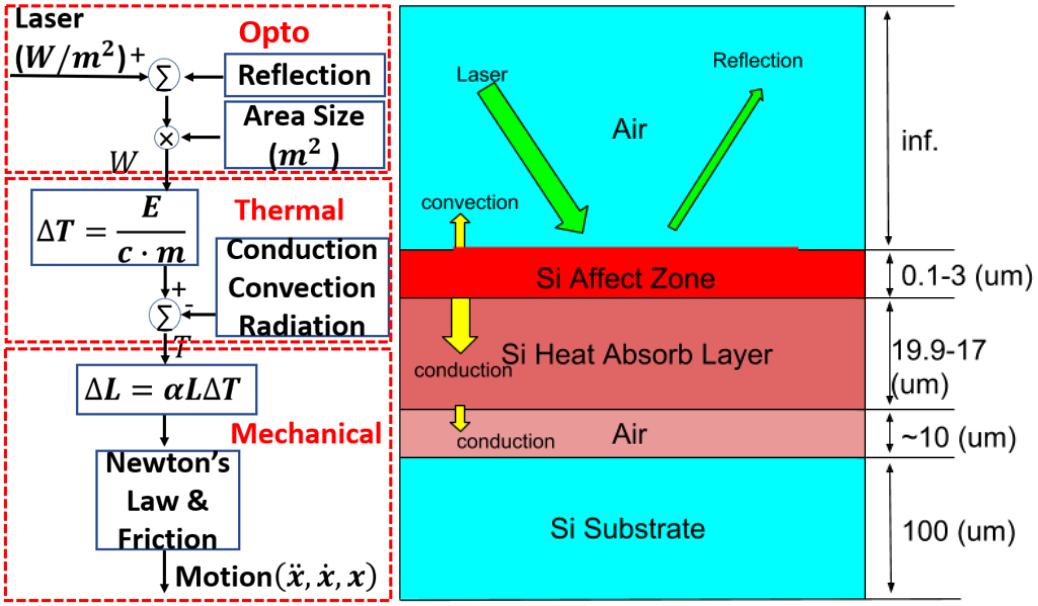

Figure 4-2 Photo-Thermal-Mechanical conversion for ChevBots, and representative layer thickness of the robot geometry.

4.2.1 Opto-Thermal Model

The Opto-Thermal model describes the behavior of the robot transferring light to heat energy. In this process, some of light energy is reflected on the microrobot surface, while the rest is absorbed to generate heat dissipated by thermal conduction, air convection and radiation. If enough time elapses, the temperature on the CTA will reach an equilibrium, and a steady-state displacement. If the temperature stays bounded below normal operating conditions for CTAs, radiation and convection are typically much smaller than conduction, and can be neglected [22,34]. From the conservation law of energy, we have:

$$dQ_{laser} - dQ_{ref} - dQ_{cond} = dQ_{st}, \tag{4-1}$$

where dQ_{laser} is the energy generated by the laser, dQ_{ref} is the energy lost by surface reflection, dQ_{cond} is the energy lost by conduction, and dQ_{st} is the energy storage in the thermal actuator, which will generate thermal expansion. By expanding terms in this

equation through Newton's law of cooling, we obtain a first order differential equation describing the CTA's average temperature T as a lumped model [35]:

$$(1-R)E_eA_l - hA_r(T-T_\infty) = \rho Vc\frac{dT}{dt}, \tag{4-2}$$

in which R is the surface reflectivity, E_e is the laser irradiation, A_l is the laser spot heating area, h is the thermal conductivity constant, A_r is the thermal actuator area, T_∞ is the environment temperature, ρ is the material density, V is the volume of the actuator and c is the specific heat capacity of the microrobot material.

4.2.2 Thermal Expansion and Displacement of the CTA

Eq. (4-2) drives the actuator temperature and is the source of thermal expansion generating both displacement and driving force of the microrobot's CTA. The thermal expansion length $\mathrm{d}L$ can be written as:

$$\mathrm{d}L = \alpha L \mathrm{d}T, \tag{4-3}$$

where the α is the thermal expansion coefficient, $\mathrm{d}T$ is the temperature change on the thermal actuator, and L is the original length actuator beams. Furthermore, the relation between thermal expansion $\mathrm{d}L$ to the displacement d_T of the CTA can be calculated by:

$$d_T = \sqrt{[L^2 + 2L(\mathrm{d}L) - Lcos^2(\theta)]} - Lsin(\theta), \tag{4-4}$$

where the θ is the angle of the bent beam of the CTA. Finally, the relationship between displacement of actuator Δd_T and force F_a on the actuator is given by [23]:

$$F_a = \frac{2NAEsin^2(\theta)}{L} d_T, \tag{4-5}$$

where N is the number of beams of the Chevron actuator, A is cross sectional area of the beams, E is Young's modulus.

4.2.3 1D Spring and Damper Model of the ChevBot

By lumping the mass of the robot frame into mass m_2 and the mass of the CTA and feet into mass m_1, we can describe a 1D dynamic model for the microrobot according to the free body diagram of Figure 4-1 (right). When the laser is on, a CTA force F_a given in equation (4-5) is applied on the spring mid-section of the robot. This force will be projected onto the horizontal and vertical directions and result in varying friction forces as a function of tilt angle β. The spring-mass-damper system has two degrees of freedom x_1 and x_2, resulting in two equations according to force equilibrium along the horizontal x axis. For actuator and feet, this becomes:

$$-F_a \cos\beta + k\left(\frac{x_2 - x_1}{\cos\beta} - l_0\right)\cos\beta - \text{sign}(\dot{x}_1)f_1 + b(\dot{x}_2 - \dot{x}_1) = m_1\ddot{x}_1, \qquad (4\text{-}6)$$

while for robot body and dimple it is:

$$F_a \cos\beta - k\left(\frac{x_2 - x_1}{\cos\beta} - l_0\right)\cos\beta - \text{sign}(\dot{x}_2)f_2 - b(\dot{x}_2 - \dot{x}_1) = m_2\ddot{x}_2. \qquad (4\text{-}7)$$

In the dynamical equations, (4-6) and (4-7), k and b represent the actuator stiffness and viscous damping coefficients, while l_0 is the initial actuator length. Furthermore, the friction forces are expressed from the resultant of vertical forces accruing on masses m_1 and m_2 respectively, expressed by a Stribeck Friction model given by:

$$f_1 = \mu\left(m_1 g + \left(-F_a \sin\beta + k\left(\frac{x_2 - x_1}{\cos\beta} - l_0\right)\sin\beta\right)\right) - k_v\dot{x}_1, \qquad (4\text{-}8)$$

$$f_2 = \mu\left(m_2 g - \left(F_a \sin\beta - k\left(\frac{x_2 - x_1}{\cos\beta} - l_0\right)\sin\beta\right)\right) + k_v\dot{x}_2, \qquad (4\text{-}9)$$

where $\mu \in \{\mu_s, \mu_d\}$, μ_s is static friction constant. μ_d is the dynamic friction constant, depending on the pushing force F_a and the friction regime, k_v is a viscous friction constant. h_d is the dimple height. The tilt angle β can be expressed by:

$$\beta = \tan^{-1}\frac{h_d}{x_2 - x_1}. \quad (4\text{-}10)$$

The Stribeck friction model is a combination of Coulomb friction and viscous friction and was shown to be accurate in predicting the average speed of microscale stick and slip motion, but not in accurately predicting the instantaneous velocity of the microrobot legs [23]. In particular, the velocity of dimple or leg in the "stuck" phase will not be zero as needed. Although other stick-slip models such as LuGre can be applied for more accurate leg motion prediction, here we avoid additional modeling complexity by switching the stick and slip conditions of the leg and body according to a velocity threshold constant ε in the algorithm below:

Algorithm 4-1: Stick- Slip motion calculation

For i=1,2
if *Force applied > static friction force on mass* m_i
  Output current velocity v_i *calculated by acceleration integration of eq. (4-6) or (4-7) with dynamic friction coefficient.*
else if $|v_i| < \varepsilon$
  Set v_i *velocity to zero*
else
  Output current velocity v_i *calculated by acceleration integration of eq. (4-6) or (4-7) with dynamic friction coefficient.*
  Calculate x_i *location by integrating velocity* v_i.
end

4.2.4 2D Model of the ChevBot

We can expand the 1D dynamical model of the microrobot by considering the three points/lines of contact with the substrate referring to the free body diagram in Figure 4-3.

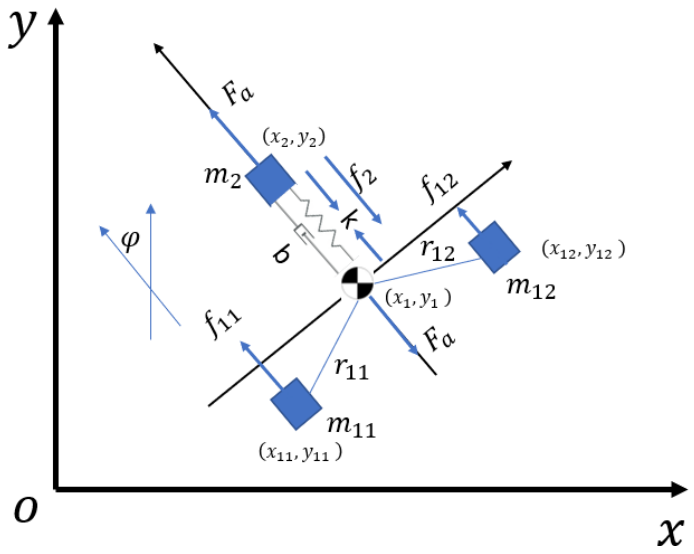

Figure 4-3. The free body diagram of the ChevBot extended to 2D.

The CTA actuator can generate forces and push the robot to move forward or backward, while the friction force unbalance will generate a torque causing rotations. Thus, the ChevBot will behave similarly to a differential drive robot and is susceptible to uneven friction/stiction forces and uncertainty of touching surfaces on the substrate. A 2D extension of the model in equations (4-6) and (4-7) will have an additional equation of motion summarized in vector form notation:

$$\boldsymbol{F_a} - \boldsymbol{f_2} - k(\boldsymbol{x_2} - \boldsymbol{x_1} - \boldsymbol{R} \cdot \boldsymbol{l_0}) - b(\dot{\boldsymbol{x}}_2 - \dot{\boldsymbol{x}}_1) = m_2 \ddot{\boldsymbol{x}}_2, \tag{4-11}$$

$$-\boldsymbol{F_a} + \boldsymbol{f_{11}} + \boldsymbol{f_{12}} - k(\boldsymbol{x_1} - \boldsymbol{x_2} - \boldsymbol{R} \cdot \boldsymbol{l_0}) - b(\dot{\boldsymbol{x}}_1 - \dot{\boldsymbol{x}}_2) = (m_{11} + m_{12}) \ddot{\boldsymbol{x}}_1, \tag{4-12}$$

$$I\ddot{\varphi} = \boldsymbol{r_{11}} \times \boldsymbol{f_{11}} + \boldsymbol{r_{12}} \times \boldsymbol{f_{12}}, \tag{4-13}$$

where bolded quantities are 2 dimensional vectors, $\boldsymbol{f_2}$ is the friction force on the dimple, $\boldsymbol{f_{11}}$ and $\boldsymbol{f_{12}}$ are the friction forces on two microrobot feet, $\boldsymbol{r_{11}}$ and $\boldsymbol{r_{12}}$ are the positional vectors from friction forces $\boldsymbol{f_{11}}$ and $\boldsymbol{f_{12}}$ to the center of the mass of the ChevBot and $\boldsymbol{R}$ is rotational matrix from ChevBot local frame to the global frame. In a 2D scenario, the

ChevBot has 5 degrees of freedom in total, and the equations of motion (4-11) -(4-13) can be expanded as:

$$\begin{pmatrix} F_{ax} \\ F_{ay} \end{pmatrix} - \begin{pmatrix} f_{2x} \\ f_{2y} \end{pmatrix} - k\left[\begin{pmatrix} x_2 \\ y_2 \end{pmatrix} - \begin{pmatrix} x_1 \\ y_1 \end{pmatrix} - \begin{pmatrix} \cos\varphi & -\sin\varphi \\ \sin\varphi & \cos\varphi \end{pmatrix}\begin{pmatrix} l_0 \\ 0 \end{pmatrix}\right] - \mathrm{b}\begin{pmatrix} \dot{x}_2 - \dot{x}_1 \\ \dot{y}_2 - \dot{y}_1 \end{pmatrix}$$

$$= m_2 \begin{pmatrix} \ddot{x}_2 \\ \ddot{y}_2 \end{pmatrix}, \tag{4-14}$$

$$-\begin{pmatrix} F_{ax} \\ F_{ay} \end{pmatrix} + \begin{pmatrix} f_{11x} \\ f_{11y} \end{pmatrix} + \begin{pmatrix} f_{12x} \\ f_{12y} \end{pmatrix} - k\left[\begin{pmatrix} x_1 \\ y_1 \end{pmatrix} - \begin{pmatrix} x_2 \\ y_2 \end{pmatrix} - \begin{pmatrix} \cos\varphi & -\sin\varphi \\ \sin\varphi & \cos\varphi \end{pmatrix}\begin{pmatrix} l_0 \\ 0 \end{pmatrix}\right] - \mathrm{b}\begin{pmatrix} \dot{x}_1 - \dot{x}_2 \\ \dot{y}_1 - \dot{y}_2 \end{pmatrix}$$

$$= (m_{11} + m_{12}) \begin{pmatrix} \ddot{x}_1 \\ \ddot{y}_1 \end{pmatrix}, \tag{4-15}$$

$$I\ddot{\varphi} = -r_{11} f_{11y}\cos\theta_{11} + r_{11} f_{11x}\sin\theta_{11} - r_{12} f_{12y}\cos\theta_{12} + r_{12} f_{12x}\sin\theta_{12}, \tag{4-16}$$

where F_{ax} and F_{ay} are the components of F_a, f_{2x} and f_{2y} are the components of friction force on dimple, f_{11x}, f_{11y}, f_{12x} and f_{12y} are the components of friction force on feet, x_1 and y_1 are the position of the dimple, x_2 and y_2 are the position of the center of the mass of the microrobot. m_{11} and m_{12} are the mass distributed on feet, the m_2 is the mass distribute on dimple. r_{11} and r_{12} are the distance of masses distribute on legs relative to the mass of center, I is angular moment of inertia, φ is the microrobot orientation angle, θ_{11} and θ_{12} are the angle configuration of the feet relative to the center of the mass, k and b are the CTA spring constant and damping coefficients, respectively.

4.3 Simulation Results

4.3.1 Opto-Thermal Finite Element Analysis

To better understand the thermal behavior and stiffness of the actuator of the ChevBot, we conducted a series of Finite Element Analysis (FEA) Multiphysics simulations. Although many FEA packages, such as ANSYS® offer computing engines

for coupled thermal, mechanical, magnetic, piezoelectric, etc., effects, they do not simulate laser radiation absorption. To simulate photo-thermal behavior in our study the absorption of laser energy can be approximated. Specifically, we calculate a heat reception (HAZ) layer on the top surface of the ChevBot, and then implement this layer via "Internal Heat Generation" boundary conditions. The HAZ thickness is given by Beer-Lambert's law written as [17]:

$$e^{-\alpha z} = 0.1, \tag{4-17}$$

where the α is the absorption coefficient, and 0.1 means 90 percent of the transmitted light is absorbed below depth z. In our case, using Si material absorption constant $\alpha = 10197.2(cm^{-1})$ for a green $532\ nm$ laser [35], a resulting $2\ \mu m$ thick HAZ layer with a rectangular shape representing the laser spot was sliced on the device layer. An ANSYS® model was built to simulate a $780\ \mu m \times 510\ \mu m$ tethered microrobot block, with all vertical structures corresponding to the handle layer, the buried oxide, and $2\ \mu m$ air gap between release and the device layer. FEA simulations were conducted using an irradiance of 2e7 W/m^2 directed at the microrobot as shown in Figure 4-4. This irradiance value is similar to the energy of the laser beam used in experiments.

The boundary conditions of our model include conduction to the substrate via the air gap under the microrobot, and via tethers. In the tethered case, the robot is stationary, therefore the laser beam is heating up both the robot and the surrounding substrate. In the case when an untethered microrobot is operated, it is inclined at a tilt angle to the substrate. In this case, a larger triangular prismatic-shaped air gap was defined under the actuator geometry, and conduction occurred through the air gap, as well as through direct contact of the dimple and feet to the substrate. The boundary conditions were modified to simulate

the mobility of the robot via a constant temperature on the substrate. In our simulation, we used a total of 9305 hexahedron and tetrahedron mesh elements. Simulation runs to solve the transient thermal-mechanical process with 5000 data samples took typically 5 hours on a Core i7-600k @ 4Ghz computer.

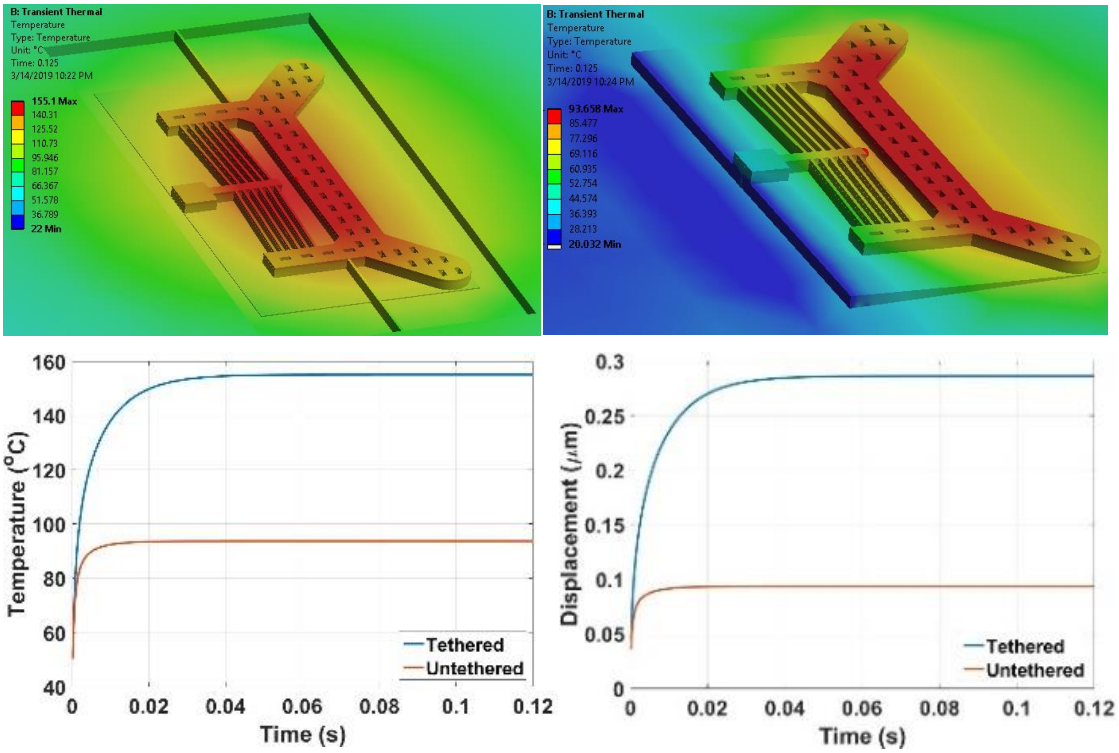

Figure 4-4 ANSYS® Thermo-mechanical simulation for shuttle displacement and temperature distribution of ChevBots tethered (left-top), and untethered (right-top). Graphs correspond to maximum temperature (left) and displacement (right).

Transient response simulations were run by setting volume heat generation as a step function input and extracting temperature or displacement data for system identification. In a small-displacement linear approximation, a transfer function can be defined as $H(s) = \frac{Y(s)}{X(s)}$, in which $X(s)$ is the volumetric heat generation in $pW/\mu m^3$(converted from the irradiance we mentioned), and $Y(s)$ is the actuator displacement in μm. Using a unit step

function volumetric heat generation, we can identify a first order model fit to data generated in either situation, leading to:

$$H_{tethered}(s) = \frac{0.280}{s+143.7}, \tag{4-18}$$

$$H_{untehtered}(s) = \frac{0.094}{s+556.8}. \tag{4-19}$$

Results indicate that the microrobot boundary conditions and operating environment have a considerable impact on its response. In particular, those ChevBots tethered to the substrate will have a steady state displacement and time constant equal to $0.280\ \mu m$ and $7\ ms$, respectively. Untethered ChevBots, on the other hand, experience a smaller static displacement $0.094\ \mu m$ and time constant $1.8\ ms$.

FEA can also calculate other important parameters of our model, including the actuator spring constant k. In particular, we applied $10\ \mu N$ force on the CTA and recoded a shuttle deformation of $0.015\ \mu m$, resulting in a spring constant estimate $k = 645.5\ N/m$. Material and geometric FEA simulation parameters are detailed in Table II.

TABLE II. VALUES OF GEOMETRIC PARAMETERS AND MATERIAL CONSTANTS USED IN FEA SIMULATION OF CHEVBOTS.

l_b	Beam Length	200.25 (μm)
W_b	Beam width	5 (μm)
τ_b	Beam thickness	20 (μm)
α_b	Beam angle	2.860°
N	Beam number	12
ρ_{Si}	Density of Silicon	2328 $(kg \cdot m^{-3})$
E_{Si}	Si Young's modulus	165 (GPa)
k_{Si}	Si thermal conductivity	124 $(W \cdot m^{-1} \cdot ℃^{-1})$
C_{v-Si}	Si Specific heat constant	702 $(J \cdot kg^{-1} \cdot K^{-1})$
α_{Si}	Silicon thermal expansion	2.6e-6 $(℃^{-1})$
ρ_{air}	Density of Air	1.225 $(kg \cdot m^{-3})$
k_{air}	Air thermal conductivity	0.02624 $(W \cdot m^{-1} \cdot ℃^{-1})$
C_{v-air}	Air specific heat	716 $(J \cdot kg^{-1} \cdot K^{-1})$
h_{air}	Air convection constant	10 $(W \cdot m^{-2} \cdot K^{-1})$
τ_{air}	Thickness of Air Layer	2 (μm)

4.3.2 Velocity Prediction Using 1D and 2D Models

Using the 1D and 2D dynamic models introduced in section 4.2, we conducted simulations to predict the untethered microrobot motions on the substrate, with the help of time constants identified by the FEA. Values were further corrected after experiments (see section 4.3). The transfer function in eq. (4-19) was used to generate CTA actuator forces corresponding to pulsed laser irradiance levels. A $5\ kHz$ pulse signal of laser with peak energy (irradiance) $1.74e7\ W/m^2$ was input into the model and stick-and-slip Algorithm 4-1 was implemented in Simulink®. Simulation constants in Table II were obtained via a combination of FEA simulations, geometrical dimensions, while damping coefficients were approximated to correspond to overdamped responses consistent to Figure 4-4. Simulation results from the 1D model are shown in Figure 4-5. The plots depict a typical static-dynamic friction transition, and the resulting stick-slip causing a net velocity in the negative X direction, revealing that backward velocities of $55.59\ \mu m/s$ can be achieved.

Ideally, because the ChevBot only have one actuator, their trajectories should align to a straight line, however, the presence of surface imperfections (particles, organics, etc.) on the substrate introduces uncertainty in friction/stiction constants that may vary between feet and dimple. Using the 2D model, we simulated different friction constants configurations represented by friction parameters of μ_s, μ_d. Simulation results are shown in Figure 4-6. and reveal a high sensitivity of microrobot motion to surface conditions. ChevBot trajectories vary significantly in terms of turn radii, velocities, and direction of motion. In general, results indicate that the higher the friction coefficients, the faster the robot motions can be obtained, while the larger the friction imbalance, the smaller the turn radius.

TABLE III. VALUES OF GEOMETRIC PARAMETERS AND MATERIAL CONSTANTS USED IN 1D AND 2D DYNAMIC SIMULATION OF CHEVBOTS.

b	Damping	6.8e-5 (kg/s)
k_b	Spring constant	645.578 (N/m)
m_1	1D mass of feet	1.095(μg)
m_2	1D mass of frame	3.3054(μg)
h_d	Dimple height	20 (μm)
μ_s	Static friction constant	0.4
μ_d	Dynamic friction constant	0.33
k_v	Viscous constant	8.5e-7(Ns/m)
l_0	Original CTA length	170 (μm)
I	Angular Inertia	5.0957e-2 $(\mu g \cdot \mu m^2)$
m_{11}	Distributed mass on left feet	1.1324 (μg)
m_{12}	Distributed mass on right feet	1.1324 (μg)
m_2	Distributed mass on frame	1.5098 (μg)
r_{11}	Distance of left feet to center	50 (μm)
r_{12}	Distance of right feet to center	50 (μm)
θ_{11}	Configuration angle of left feet	1.5708 (rad)
θ_{12}	Configuration angle of right feet	-1.5708 (rad)

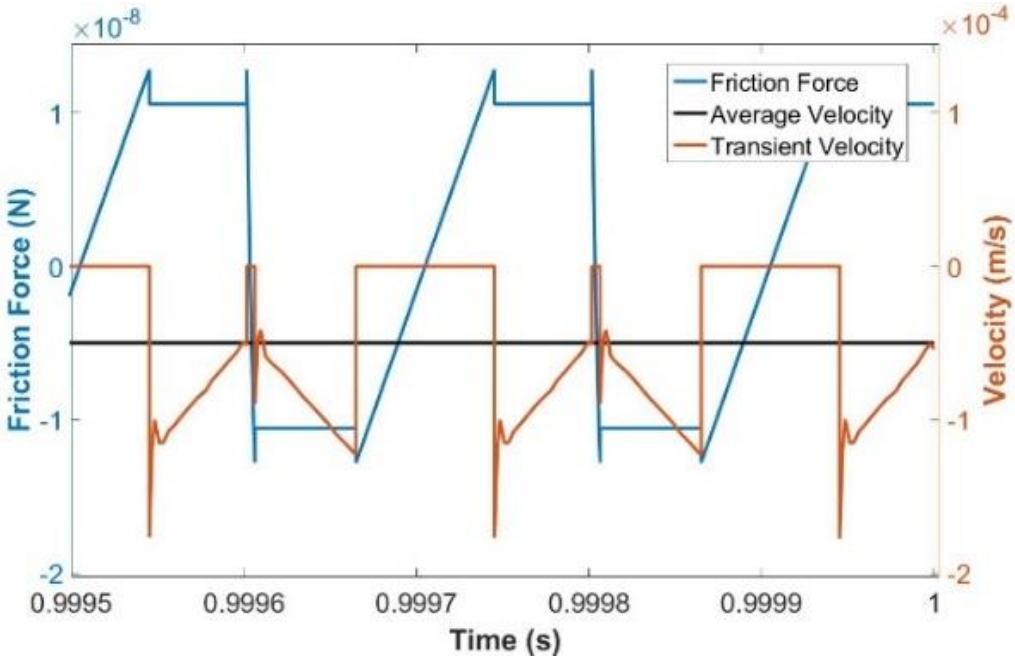

Figure 4-5 Friction and Velocity of ChevBot frame during stick-slip.

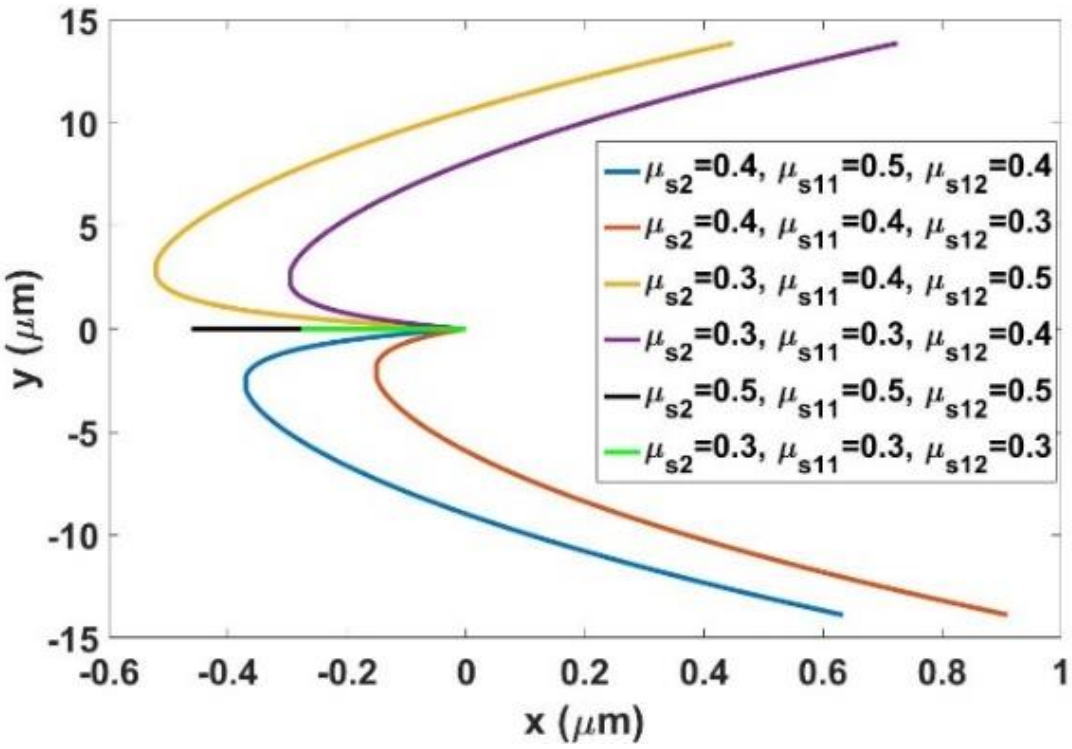

Figure 4-6 2D trajectories of the microrobot resulting from a combination of friction constants, assuming that μ_d is 90% of μ_s. Each trajectory is recorder over in 0.1 seconds, starting at the origin.

4.4 Experimental Validation

4.4.1 Experimental Instrument to Drive ChevBots

Experiments were realized with the help of a custom configured experimental instrument, shown in the schematic of Figure 4-7. The components of the optical system include:

- Explorer One® Nd: YAG laser from Spectra-Physics, with 532 nm wavelength, 2 W Maximum power, 0.5-60 kHz repetition rate and 10 to 40 ns pulse time width.
- A system of lenses, neutral density filters, beam splitters and mirrors to deliver laser energy to the microrobot.

- *X-Y* positioning stages from Newport: one 443 series and three 423 series, with two actuated by linear motor TRA25CC and two controlled manually.
- Tube lens, illuminator, beam splitter, NI Smart camera ISC-1772C for automated tracking and Pixelink CMOS camera for process visualization.
- A range sensor, LK-H008 from Keyence, to measure displacement of the tethered CTA actuator.

During the measurements, the laser beam can be operated under either continuous or burst mode. Continuous mode generates a series of pulses, while under burst mode, the user can specify the number of pulses within a burst and delay between each burst. For both cases, repetition rate of the fundamental pulses and diode current are adjustable. The average power of the laser is defined by diode current and repetition rate within each burst or during continuous mode.

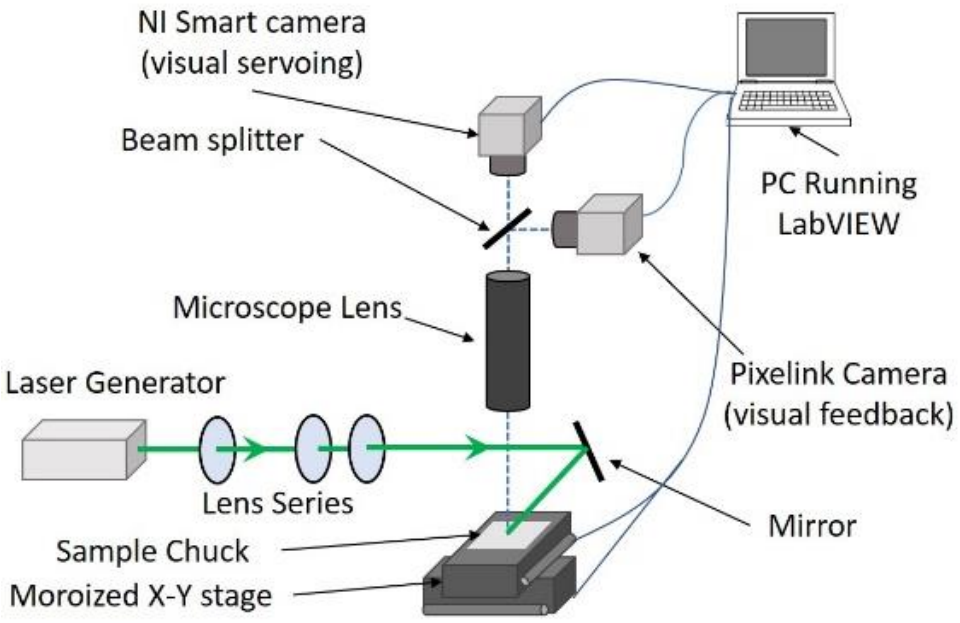

Figure 4-7 Laser delivery and vision acquisition schematic.

Two types of ChevBot laser irradiation experiments were conducted with tethered and untethered microrobots. In the case of the tethered ChevBot, only motion of the thermal actuator was studied. For the untethered microrobot, the goal was to initiate and record stick and slip motion of the whole microrobot on a silicon substrate with the overhead camera.

4.4.2 Tethered ChevBot Dynamic Response

In this configuration ChevBot's body was tethered to the (SOI) device layer thus its frame was stationary, and the actuator and feet are set into the motion upon laser irradiation. The purpose of these measurements was to characterize the actuator sub-micron displacements for specific boundary conditions and acquire results which could utilized for the system identification and validation of simulation results in section 4.3. The repetition rate of the laser was set to $1700\ Hz$ for maximum actuator displacement and the laser diode current was considered as input to system identification. The system's output was the displacement of the thermal actuator, measured by Keyence displacement sensor. A testing die was designed in such way that many tethered ChevBots are located at the edge of the die so that the displacement sensor has access to the leg of thermal actuator to acquire the dynamic measurement. The displacement sensor collected data at a sampling rate of $10\ kHz$, as depicted in Figure 4-8.

The transfer function identified experimentally is a ratio between laser irradiation, as measured indirectly via the laser diode current of the Explorer Nd: YAG unit, and the actuator displacement measured by the Keyence® sensor. As a result, the DC gain of this transfer function bears no similarity to that of the FEA model in section 4.3.1. However,

the time constant of the model should be similar. The first order system identification results were:

$$H_{tethered}(s) = \frac{154.1}{s+524}, \tag{4-20}$$

The system identification result shows the experimental time constant is about $2\ ms$, while the FEA simulation for the tethered the boundary condition is $7\ ms$. Through FEA, we concluded that the tethered robot boundary conditions have introduced more substrate thermal influence than the untethered case, leading to untethered robots time constants and displacements approximately 3 times faster/higher than tethered ones. As a result, we corrected our CTA simulation model estimates based on a time constant of $2\ ms$.

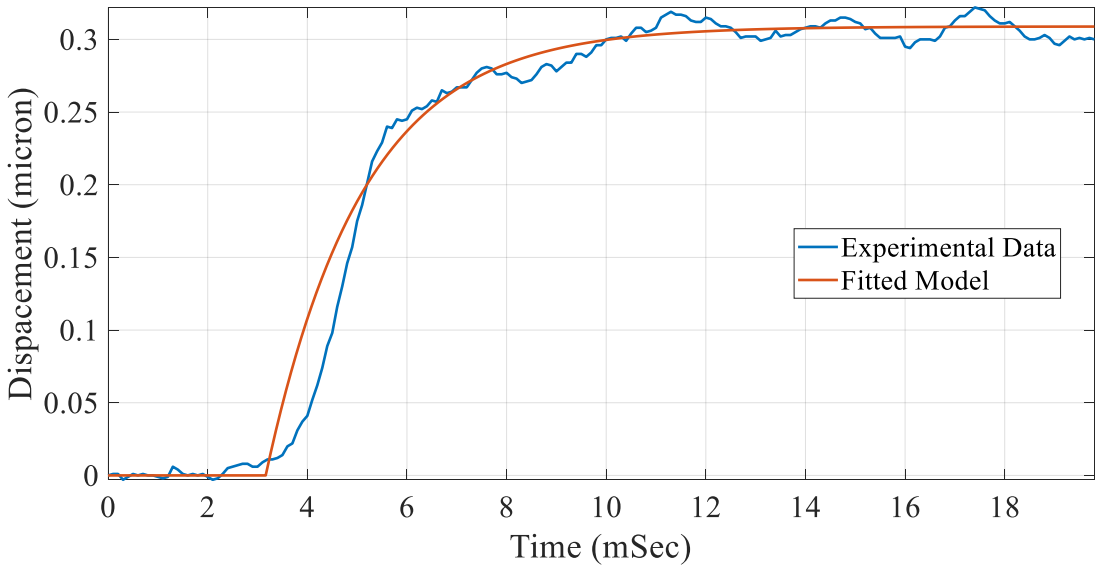

Figure 4-8 Laser power stimulus as input and ChevBot CTA actuator as output fitted to a first order transfer function displacement.

4.4.3 Untethered ChevBot Velocity Measurements

In the second batch of experiments, assembled ChevBots were actuated on a silicon substrate by burst mode. The laser beam was focused onto the ChevBot with sufficient power to initiate gating motion, causing the robot to escape from the laser beam waist. At

that point the microrobot loses power, the laser beam needs to be repositioned to track the motion of the robot. In a novel twist, we keep the laser beam position fixed, but we reposition the robot to the laser spot using a visual servoing scheme implemented by camera feedback [18]. The vision system processes the 640×480 pixel image and extracts the location of the microrobot with a pattern matching feature. An Image Jacobian was identified for visual servoing to bridge the mapping between robot feature positions and the stage displacement. In order to maintain the ChevBot in the center of the camera image, where the laser has been focused, visual servoing feedback provides current pixel location of ChevBots, compares it with the desired pixel location, and generates an error term to drive the stages.

Experiments were conducted with untethered ChevBots, confirming that the microrobot generates a fairly straight trajectory in the defined backward direction, as shown in Figure 4-9, where all trajectories begin from the origin for $0.1\ s$. The effect of different laser parameters on speed are summarized in Table IV. The trajectory plots of the ChevBot are recorded using X and Y encoder readings of the stages while the microrobot is tracked. While most trajectories show straight components, the turning behavior suggests the microrobot encounters dust specks or unbalanced friction conditions. Depending on the geometry and surface condition of the dust, the microrobot may be forced to steer, or completely stop. The experimentally measured velocity of ChevBots under different laser configurations were compared to 1D simulation results, indicating general trend-wise agreement.

Finally, we randomized the friction constant to emulate varying surface conditions of the substrate, with friction constants between 0.1 and 0.3. Simulation results shown in

Figure 4-9 (bottom) indicate that similar length trajectories to the experiment can be obtained through our fitted 2D model.

TABLE IV. MEASURED AND SIMULATED VELOCITIES OF CHEVBOT UNDER VARYING LASER POWER CONDITIONS. 1D SIMULATIONS WERE CONDUCTED USING μS=0.4.

Test	***Pulses***	***Burst Delay***	***Average Power***	***Measured Velocity***	***Simulated Velocity-1D***
1	30	200 ms	388~454 mW	21.8 $\mu m/s$	51.37 $\mu m/s$
2	40	100 ms	410~468 mW	90.6 $\mu m/s$	59.83 $\mu m/s$
3	50	100 ms	432~490 mW	83.4 $\mu m/s$	60.21 $\mu m/s$
4	50	50 ms	440~504 mW	109.0 $\mu m/s$	89.86 $\mu m/s$

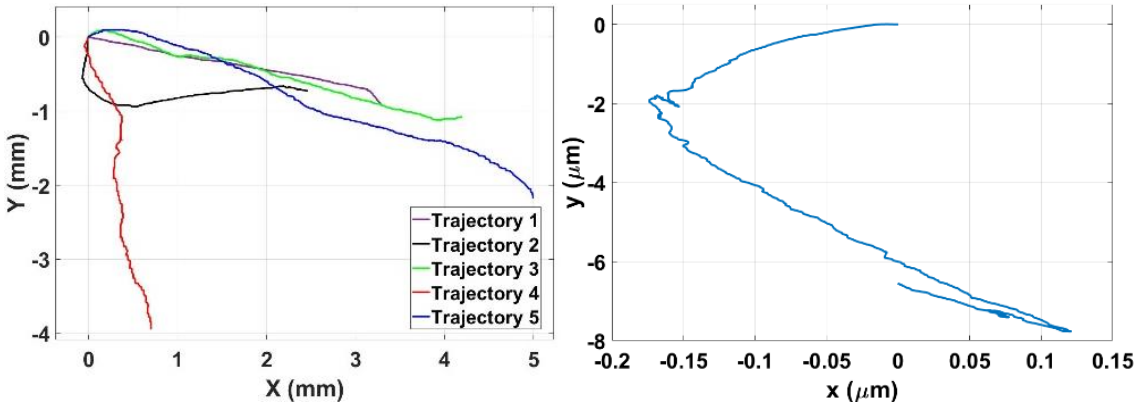

Figure 4-9 ChevBot's trajectories from 5 different experiments (top) in 1-2 minutes, and a randomized parameter 2D simulation result (bottom) in 0.1 seconds.

4.5 Summary

Through the ChevBot, we have verified the concept of the Laser Driven Locomotive Microrobots. We have used different modeling methods and unveiled the mechanism of this type of microrobot. However, from experiments and our model's analysis, the ChevBot doesn't have controllable behavior, since the ChevBot only have one actuator, the design of the ChevBot limit the controllability of this microrobot. So, in next the chapter we will utilize the knowledge we get from the ChevBot to introduce a type of microrobot, SerpenBot, with controllable behavior.

CHAPTER 5 SERPENBOT, A NOVEL LASER-DRIVEN MICROROBOT FOR DRY ENVIRONMENTS

In the last chapter we have discussed a systematic modeling method based on the first principal approach to help us understand the physics behind the ChevBot. This knowledge can be applied to model other types of Laser Driven Locomotive Microrobots (LDLM). In this chapter, we introduce a new LDLM, SerpenBot, describe its design and operation analysis, and discuss how new findings extend our knowledge about behavior of laser driven microscale structures.

5.1 SerpenBot Design and Modeling

Our previous studies have revealed that motion of the laser-driven microrobots strongly depends on the geometry of its body [17,18]. Therefore, design and relative location of the microrobot's components need to be considered to enable locomotion and steering on a flat surface in a controlled way. Based on the findings from the experiments with the older generation of the laser-driven robots (ChevBots) [17,18,24], we introduced and updated a new laser-driven robot based on both static and dynamic behavior considerations and a design shown in Figure 5-1. The new driving structure called Elbow Thermal Actuator (ETA) is the modification of Vertical Thermal Actuators (VTA) used in thin-film MEMS actuator designs [19]. Upon heating, the ETA's serpentine structure experiences thermal expansion, thus causing the actuator to supply the motion to the leg mechanism, and as a result, move the body of the microrobot. The actuators of the microrobot are working under a dynamic Opto-Thermo-Mechanical energy conversion

process, therefore, a multi-physics dynamic analysis of serpentine structure was conducted in order to select appropriate leg designs.

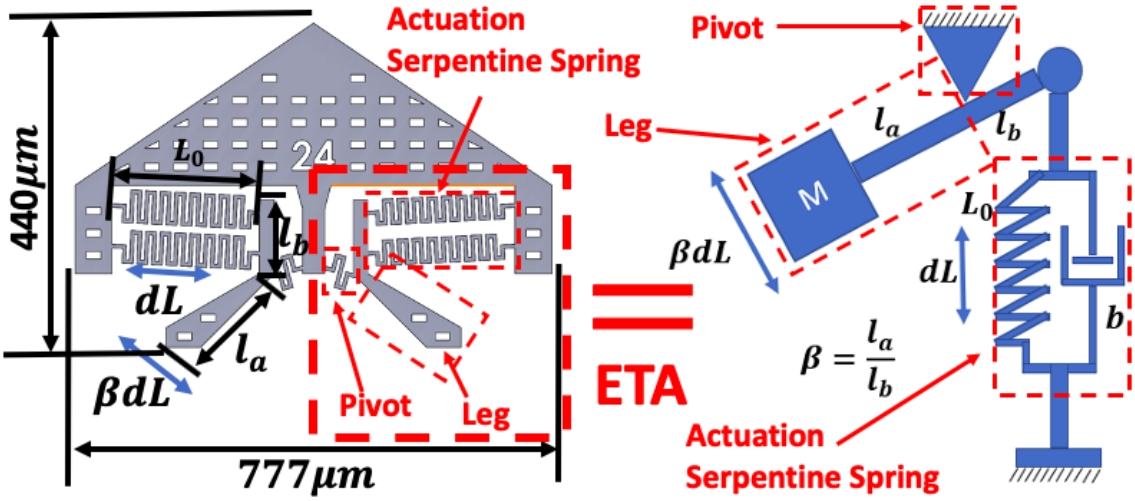

Figure 5-1 SerpenBot design based on serpentine actuator and the Elbow Thermal Actuator (ETA).

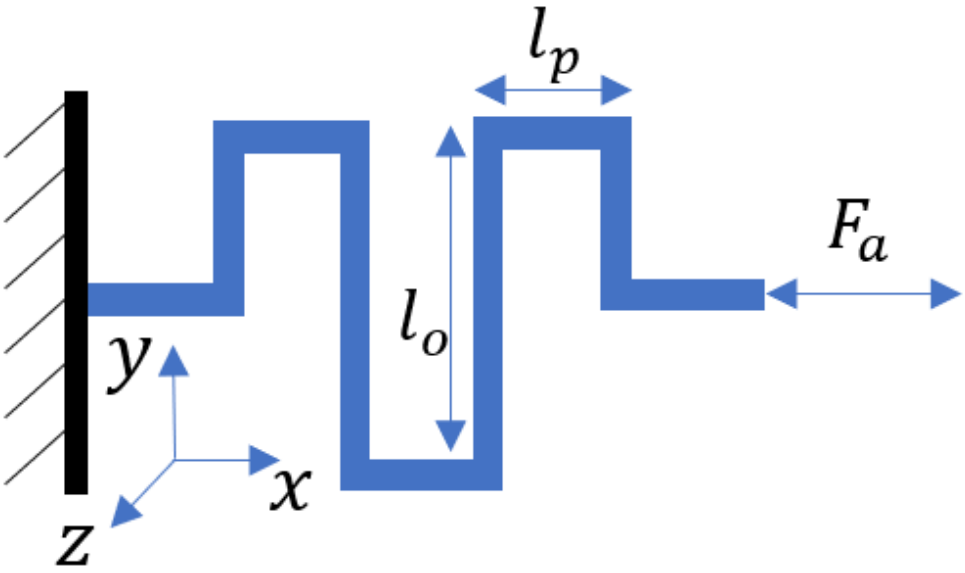

Figure 5-2 Serpentine spring of the Elbow Thermal Actuator (ETA).

5.1.1 Thermal Expansion and Displacement

The optothermal effect is an increase in temperature of the material upon laser irradiation, which leads to thermal expansion. This effect was utilized in the case of the VTA beam structure [24] and by analogy, it can be applied for the new ETA serpentine geometry. Exposing ETA to the laser energy induces thermal expansion of the structure's components (e.g., the serpentine spring) resulting in the motion of the robot's leg (Figure 5-1). We can simulate the behavior of the ETA structure and approximate thermal expansion of the serpentine spring with a lumped model. The change in the length of the serpentine spring due to thermal expansion $\mathrm{d}L$ can be expressed in following way:

$$\mathrm{d}L = \alpha L_0 \mathrm{d}T, \tag{5-1}$$

where the α is the thermal expansion coefficient, dT is the temperature change of the ETA structure, and L_0 is the equivalent original length of actuator serpentine spring. The transfer of motion from the serpentine spring to the leg (Figure 5-1) is enhanced with the help of lever component in ETA design. The enhancement rate is given by:

$$\beta = \frac{l_a}{l_b}, \tag{5-2}$$

where β is the ratio of mechanical leverage, and l_a and l_b is the length of different parts of the lever. Therefore, the displacement of the microrobot's leg dL_L is described by:

$$dL_L = \beta \mathrm{d}L = \beta\alpha L_0 \mathrm{d}T. \tag{5-3}$$

5.1.2 Actuator Stiffness

In the last section we have modeled the thermal behavior and motion mechanism of the ETA. In this section we determine the spring constant of the ETA based on its geometry. The serpentine geometry greatly influences the dynamic behavior of the actuator,

because the serpentine shape has less stiffness compared to a beam design with comparable dimensions. Furthermore, the ETA spring constant determines the resonant frequency of the structure. The spring constant of the serpentine spring is a 6 by 6 tensor. However, considering our geometry in which spring thickness is much larger than width and length, we can approximate the dominant X and Y directions (Figure 5-2) of the tensor. Thus, the spring constant of the serpentine spring in X and Y directions are given by [20, 21]:

$$k_x = \left[\frac{(N+1)l_o^3}{6EI_{zo}} + \frac{(N+1)l_o^2 l_p}{2EI_{zp}}\right]^{-1}, \tag{5-4}$$

$$k_y = \left[\frac{\left(2(N+2)l_p\right)^3}{3EI_{zp}} + \frac{\left(8N^3+36N^2+55N+27\right)l_p^2 l_o}{3EI_{zo}}\right]^{-1}, \tag{5-5}$$

where N is the number of times the structure pattern repeats, E is Young's modulus, l_o is vertical beam length, l_p is horizontal beam length, I_{zo} is z-axis moment of inertia of l_o, and I_{zp} is z-axis moment of inertia of l_p, as shown in Figure 5-2. Through equations (5-4) and (5-5), we can design different geometry constants l_o, l_p, and change N to significantly change the spring constant of the actuator. We can use these two formulas to estimate the spring constants of actuators and, later on, induce differential resonance in each leg.

5.1.3 Actuator Dynamics

In order to describe the behavior of the actuator in a dynamic situation, we can combine a lumped spring-mass-damper system equation with the lever enhancement model. The second order differential equation for ETA can be written as:

$$M\beta\ddot{L} = F_a - k(L_0 - L) - b\dot{L}, \tag{5-6}$$

where M is the mass of the leg, F_a is the thermal stress, k is the spring constant, L_0 is the equivalent original length of actuator serpentine spring, L is the actuator's length after

thermal expansion, $\dot{L}$ and $\ddot{L}$ are the speed and acceleration of the actuator length change, and b is the damping ratio. In this linear second order differential equation, and F_a is generated stress due to the thermal expansion [24]. Therefore, our system is a linear third order system. After applying the Laplace transformation to the differential equation (5-6), we have determined that the system has three poles on the Laplace domain. One real pole from the thermal behavior, and two poles from the mechanical vibration (Figure 5-3). This observation can provide us with good guidance for the design of an actuator with given range of frequency.

To actuate and steer the microrobot we use pulsed laser frequency from a single, large laser spot illuminating the SerpenBot. By tuning the pulsed frequency, we can selectively actuate only one of the actuators, left or right, in order to turn the microrobot left or right respectively. Furthermore, both actuators can be activated simultaneously in order to drive the robot along a straight trajectory. Selective activation can be done by tuning modulation frequency of the laser to resonant frequency of each actuator. Therefore, in our proposed design, each SerpenBot has two ETAs with different leg geometries, therefore two resonant frequencies of each leg given by:

$$f = \frac{1}{2\pi}\sqrt{\frac{N_s k}{m}}, \tag{5-7}$$

Given constraints on the microrobot size and the number of serpentine springs of N_s, we can lower the resonant frequency by increasing the mass of the serpentine structure or decreasing the value of the spring constant. This can be expressed by the pole shift on the complex plane depicted in Figure 5-3. From the plot (Figure 5-3) it can be seen that increase of the beam length of the serpentine spring, will shift the two imaginary poles closer to the Y axis. On the other hand, the decrease of the robot's body area will decrease

its thermal capacity, resulting in increase of the speed of the heating-cooling cycle (shift of real pole - red points in Figure 5-3).

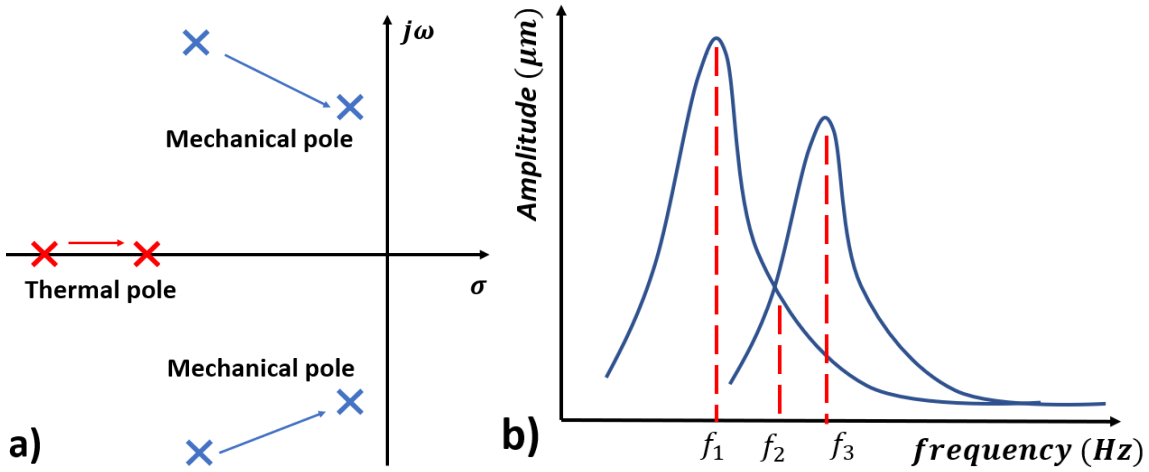

Figure 5-3 The system transfer function poles motion when increasing the size of the beams of the ETA.

Using the geometry design parameters listed in Table V, we can estimate that the resonant frequencies of the microrobot legs will be separated apart by approximately 1 kHz, as shown in Table VI.

TABLE V. ANALYTICAL & SIMULATION PARAMETERS

ρ_{Si}	Density of Silicon	2328 $(kg \cdot m^{-3})$
E_{Si}	Si Young's modulus	165 (GPa)
l_{o-left}	Left vertical beam length	40 μm
l_{p-left}	Left horizontal beam length	15 μm
$l_{o-right}$	Right vertical beam length	30 μm
$l_{p-right}$	Right horizontal beam length	15 μm
t_b	Beam thickness	5 μm
h	Device lay thickness	20 μm
m_{left}	Left actuator mass	0.00069442 μg
m_{right}	Right actuator mass	0.00077669 μg
N	Spring number of the structure repeat times	8
N_s	Actuator serpentine spring number	2

TABLE VI. LEG RESONANT FREQUENCY ESTIMATION

Left actuator	f_{ky}	Left actuator resonant frequency in Y direction	86.5 kHz
Right actuator	f_{ky}	Right actuator resonant frequency in Y direction	87.7 kHz

5.2 SerpenBot FEA Simulations

To better understand the mechanical behavior and to optimize the actuator design, we conducted Finite Element Analysis (FEA) with ANSYS®. In this study, we focus on mechanical structural simulations, while an Opto-Thermo model investigated using FEA is detailed in our past work [24].

5.2.1 FEA Static Analysis

The static FEA simulation assume that the SerpenBot is heating to temperatures of 500℃ and that the body frame is stationary. The thermal expansion on the serpentine spring determines the resulting motion on the leg. The simulation result shown in Figure 5-4 demonstrates the static deformation of the ETA and the leg under constant thermal loading, which gives us numerical values of the structure's motion. We have tabulated the resulting average displacement of the structure in Table VII.

TABLE VII MOTION OF THE SERPENBOT LEG

	l_a motion (dL) (μm)	**l_b motion (βdL) (μm)**	**β**
Left Actuator	0.8318	0.5854	1.4211
Right Actuator	0.8239	0.6125	1.3451

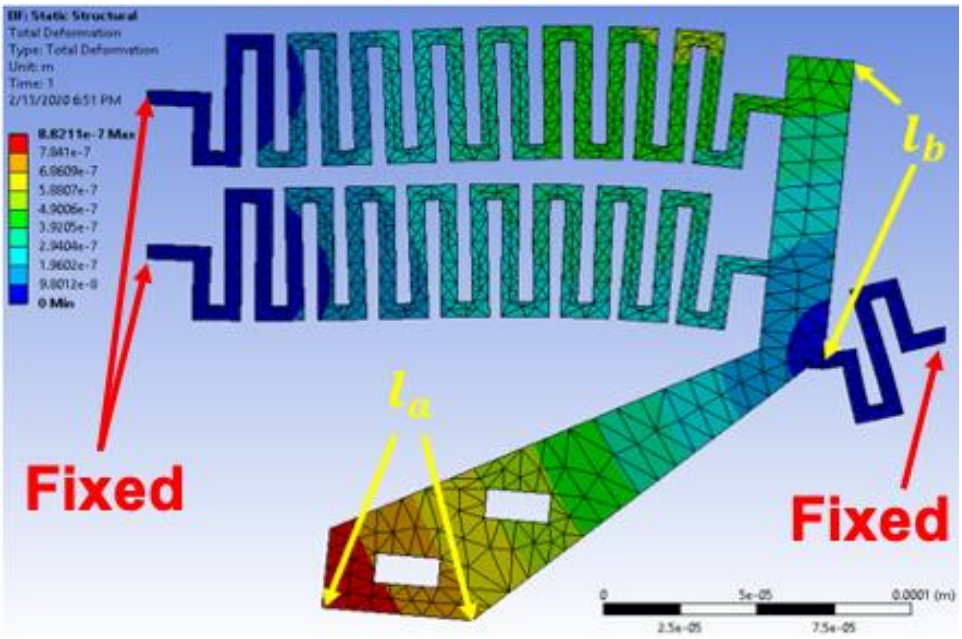

Figure 5-4 Simulation results indicating deformation of the actuator and the leg, where the end of the serpentine spring and pivot spring is fixed. The arrows indicate the reference points to calculate the average motion.

5.2.2 FEA Dynamic Analysis

In order to verify the analytic resonance differentiation between the microrobot legs and further optimize the serpentine actuator design, we employ the Modal and Harmonic Response tools in ANSYS® for vibration analysis. When untethered on the substrate, the SerpenBot's frame and legs are free to move and the contact between the legs and substrate's surface can be considered as a hinged joint. But for FEA modeling, this will bring significant complexity to the simulation. To simplify the boundary conditions, we fixed the frame of the microrobot, then apply driving force in order to analyze the vibrational modes of the actuator. The simulation results shown in Figure 5-5 are based on geometric parameters shown in Table V.

Our simulation-based findings reveal that due to geometry difference, ETAs have multiple different resonant frequencies (Figure 5-5c). In consequence, because of the

different resonant frequencies, specific driving force inputs can be activated selectively on only one actuator and leg. Considering realistic experimental conditions due to the hinged joints, we expect the experimental resonant frequency to be lower than the simulation result (Figure 5-5, Table V). In this scenario the pulsed laser with respective modulation frequency is similar to the driving force F_a from the simulation model in equation (5-6). Therefore, when the whole robot is exposed to the laser spot, only one actuator is activated due to matching of the resonant frequency of the ETA and the laser pulse frequency.

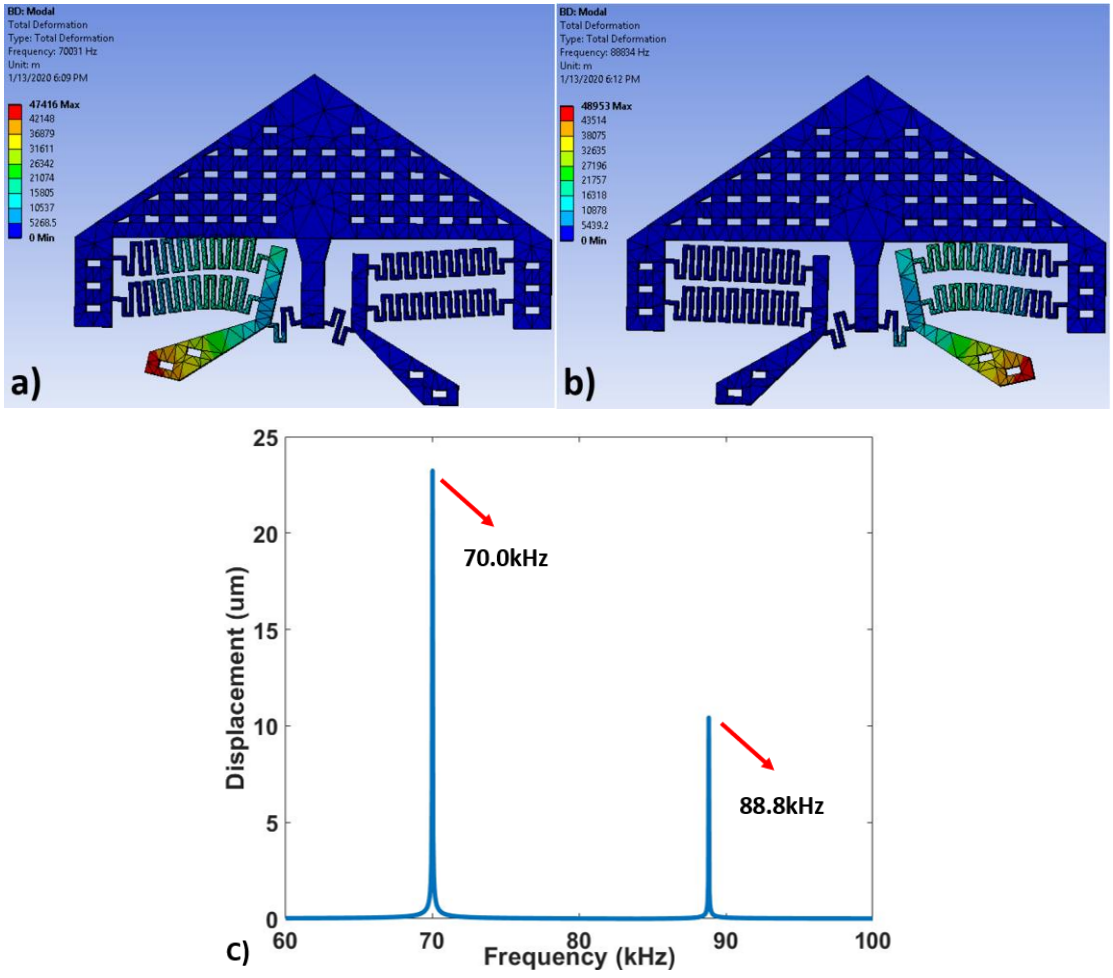

Figure 5-5 Resonant frequency peaks of the left and right leg of the microrobot.

Furthermore, the analysis only includes information about the actuator and legs of the microrobots but does not consider the necessary force output to move the frame. In the design shown in Figure 5-5a, the frame mass is about 11.8 times larger than the legs. As a result, we noted that it may also be necessary to modify the weight distribution of the microrobot to initiate the stick-and-slip motion. Furthermore, the resonance frequencies of the ETAs were estimated using the mass of the leg and actuator while the frame is fixed. Thus, resonant frequency values will undoubtedly be lower once the frame is free to move.

5.3 Fabrication and Experimental Setup

This section introduces the fabrication steps of the SerpenBot, and the locomotion experiment setup with laser delivery and power regulation system.

5.3.1 Cleanroom Fabrication

The SerpenBot is a microrobot based on MEMS technology and fabricated in cleanroom. The wafer we used to fabricate the SerpenBot is Silicon on Insulator (SOI), with the thickness of the device layer and the buried oxide layer of 20 μm and 2 μm, respectively. Since we do not pass current through the silicon nor wet etch, crystal orientation and resistivity of the wafer are not important. The substrate was first cleaned by the RCA process to remove any contamination. The photoresist MicroChem® SPR220-3.0 was selected as the masking material for subsequent bulk micromachining process for its thickness of 3 μm. It both resolves our finest features of 6 μm and is thick enough to withstand the silicon etching media. The hard baking procedure needs to ramp up and down the temperature to avoid cracks on the photoresist surface. The substrate was bulk micromachined by the Deep Reaction Ion Etching (DRIE) process to carve the shape of

the microrobot. The etching rate was estimated by profilometry, and the reflective microscopy was used to verify completion of the process by checking if the smallest etching target, the release holes, are reflecting light and appear bright at end of etch. Before release, a thorough oxygen plasma cleaning of the substrate is necessary since it removes the passivation chemicals that may impede releasing process. Releasing was performed on the die scale in the anhydrous Hydrogen Fluoride etcher for one hour.

5.3.2 Microassembly of SerpenBot

The SerpenBot was assembled by NEXUS microassembly system in several steps. The NEXUS microassembly system, Figure 5-6c, has two motorized manipulators M1 and M2. The M1 holds the vacuum secured sample chuck and provides three degrees of freedom: translational X, Y, and rotation. The end-effector, which is a vacuum tip, is mounted on the M2 manipulator. M2 has five degrees of freedom, a manual Z stage at the bottom provides a height adjustment base, four motorized stages on top of Z consist of X, Y, Z and rotation. The rotation stage is mounted on the sidewall of the last stage and the vacuum tip is fixed on it through a 3D-printed fixture.

The goal of this process is to assemble a $60\ \mu m \times 60\ \mu m$ square or $60\ \mu m$ diameter dimple onto the body of the SerpenBot, as shown in Figure 6-6a and Figure 6-6b. Since the dimple is smaller than the vacuum tip's diameter of $150\ \mu m$, a dimple handle, is designed so that it can be picked up by the tip. The dimple is attached to the handle frame by a $6\ \mu m$ wide $55\ \mu m$ long neck, which allows easy break after assembly.

The dimple with its handle was first set free by breaking all the tethers holding them. Then, it was picked up by the vacuum tip and the dimple was dipped into a pool of UV adhesive. The dimple then aligned with the assembly site on the SerpenBot's body and

lowered on it to make contact. An Ultraviolet (UV) flashlight was then used to cure the adhesive and break the neck after the glue solidifies. And eventually, the tethers holding the SerpenBot were broken and the microrobot was flipped to conclude the process.

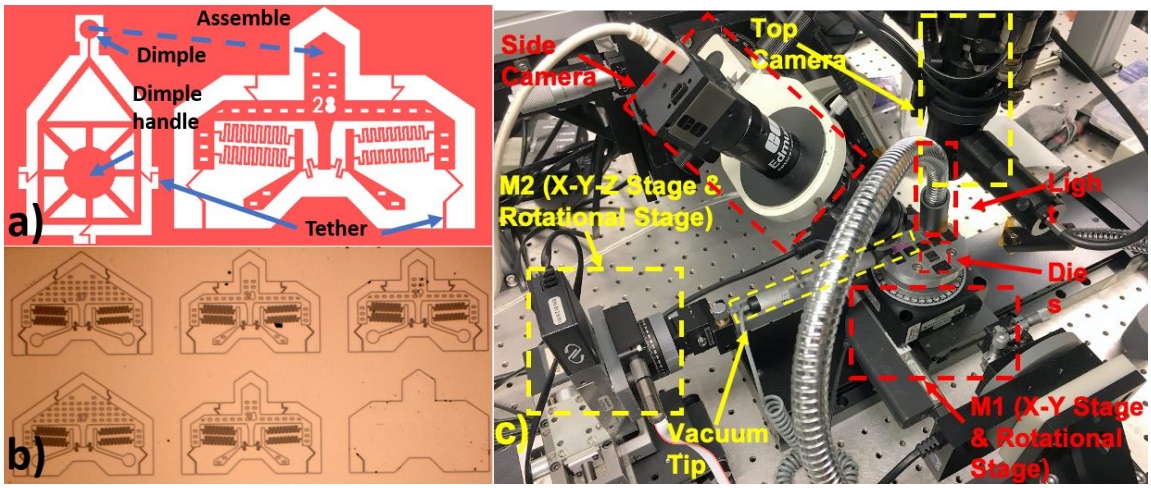

Figure 5-6 a) Illustration of the dimple and the SerpenBot body. b) Tethered SerpenBot on a Silicon die. c) The NEXUS microassembly system.

5.3.3 Experimental Setup

To experimentally validate the SerpenBot, we utilize a laser power delivery instrument that includes a laser source, camera, and motorized stages shown in Figure 5-7. The laser spot is delivered on the center of the microrobot substrate and further aligned with the center of the camera's view. A motorized stage maintains the microrobot under the laser spot through visual feedback of the microscope camera. More details about our experimental conditions and servoing controller can be found in [18, 24].

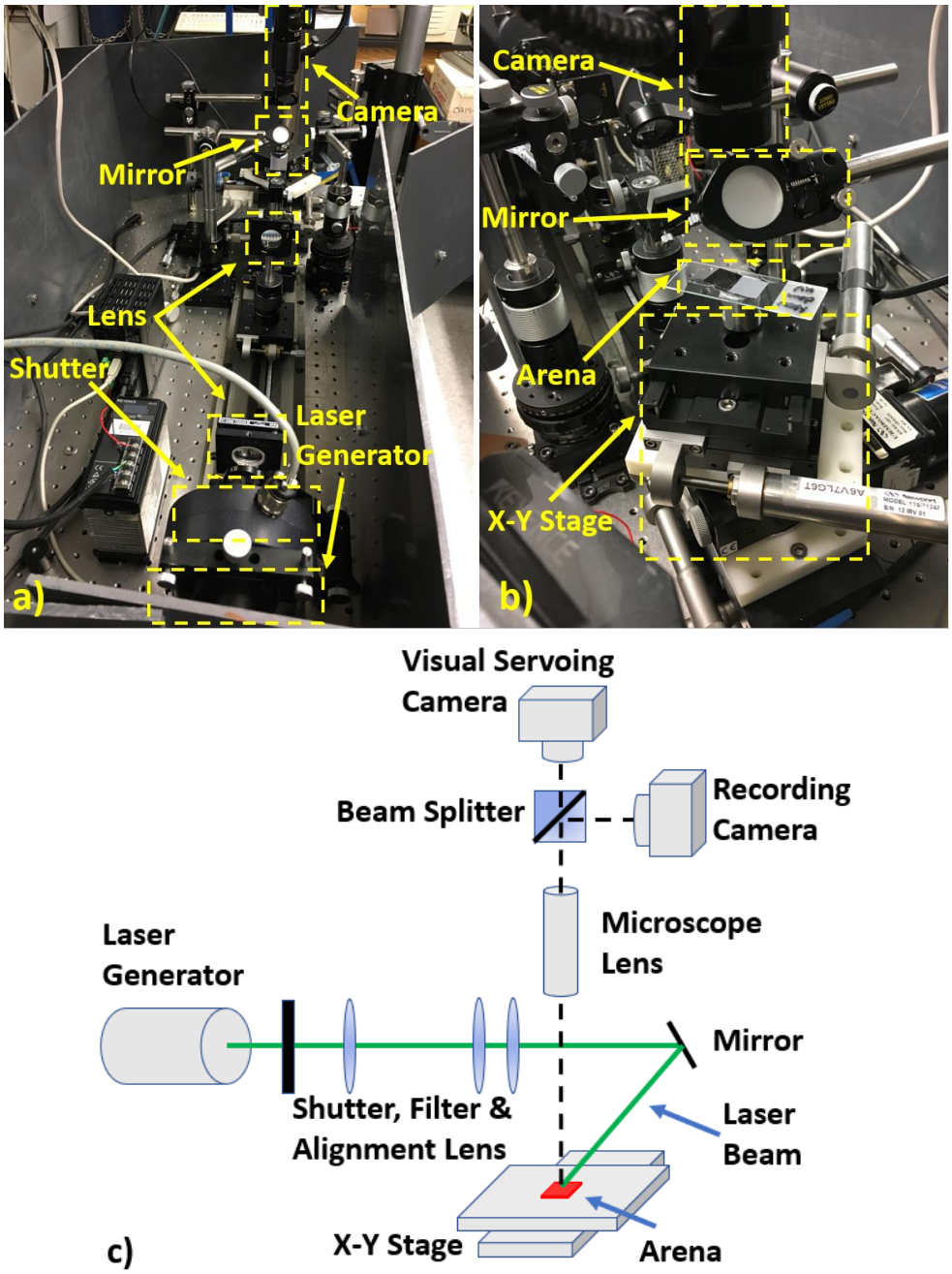

Figure 5-7 a) and b) show different views of the experimental setup. c) schematic diagram of the experimental setup.

5.4 Experimental Results and Discussion

A series of experiments were conducted in order to experimentally validate the proposed SerpenBot design and confirm its steering ability. Assembled SerpenBots with a

reduced frame mass were fabricated, assembled, and placed on a clean Si substrate as depicted in Figure 5-8. The SEM images show two slightly different microrobots in leg design, referred to as design No.28 and No.29. These sample microrobots were exposed to a pulsed laser with repetition rate swept in a range until the robot's motion was observed. Due to the different boundary conditions of an untethered microrobot compared to simulation boundary conditions we observed that differential resonance was achieved at much lower frequencies as expected, with experimental results shown in Table VIII.

The discrepancy between the calculated resonant frequency of the ETA shown in Table VIII) and values determined experimentally in Table VIII is due to the boundary conditions difference between simulation and experimental scenarios. As noted in section 5.1, the model of ETA is significantly idealized as it is very difficult to simulate motion of the untethered microrobot's leg on the substrate. On other hand, we do not have direct evidence that experimental frequencies collected in Table VIII are the actuator's resonance frequencies for two untethered SerpenBots on the Si surface.

TABLE VIII. SERPENBOT'S EXPERIMENTAL OPERATION FREQUENCY

No.	**Forward/Backward Frequency (Hz)**	**Left Frequency (Hz)**	**Right Frequency (Hz)**
28	1000	600	1700
29	1100	2000	700

In the first set of measurements, we tested multiple SerpenBots with slightly different frame and leg designs, in order to see which robot had reasonable maneuverability. The overall size of SerpenBot is less than 1mm and the mass is in the microgram level, so it is sensitive to the spring and frame design. In conclusion we see that little frame and actuator design differences will bring significant performance differences. Results show

that design No.28 and No.29 were the most responsive to laser actuation (Figure 5-8). No.28 and No.29 robots have essentially the same design of the body, with a mass 0.71 times lower than the initial design in Figure 5-5 and differing only in the shape of the legs.

A second series of experiments were conducted to realize motion and steering of the microrobots in a controlled way with the No.28 and No.29 SerpenBot designs. We tested several samples from each design to verify that the results were repeatable and consistent. During our experiments, the laser was operated in the burst mode, where each burst had 15 to 25 pulses with a 300 ms delay. The average power was in the range of 70-200 mW . The laser repetition frequency f was varied in the range between 500-5000 Hz in order to determine the f values that enables specific type of the robot's motion: forward, backward, left turn, and right turn. Robot No.28 always moves in the arrow direction shown in Figure 5-8 (forward), while robot No.29 always moves in the arrow direction backward. Both robots have frequency sensitive turning and driving behavior with 3 different f values, allowing controlled steering and motion along a straight trajectory on a silicon substrate (Table VIII).

For microrobot trajectory shown in Figure 5-9a, we can describe motion and steering mechanism of the given SerpenBot by referring to each of the 7 marked sections:

The robot is initially at rest and starts to move forward upon exposure to the laser with mod. freq. $f = 1000\ Hz$.

Change f to 600 Hz - robot turns left $\sim 45°$ – small curve radius.

Change f to 1000 Hz - robot moves in forward direction.

Change f to 1700 Hz - robot turns right gradually $\sim 180°$ – large curve radius.

Change f to 1000 Hz - robot moves in forward direction.

Change f to 600 Hz - robot turns left ~90° – small curve radius.

Change f to 1000 Hz - robot moves in forward direction.

Using this sequence of laser frequencies, SerpenBot can be steered by switching the modulation frequency of the laser between three values. The same level of control was achieved for the microrobot No.29 but naturally with a different set of frequency values – due to different geometry of the actuators and leg shapes (Figure 5-8). The shape of the recorded trajectory of the No.29 robot reveals that described steering control for this robot is also repeatable. It can be seen in Figure 5-9 that similar maneuvers (turns) are repeated by the SerpenBot several times. The velocity of the robot can be controlled by the light intensity of the pulsed laser. For our experiments, the average forward/backward velocity was 68 $\mu m/s$ and 57 $\mu m/s$ respectively, the turning angular velocity was 2.3 $°/s$ and 3.8 °/s.

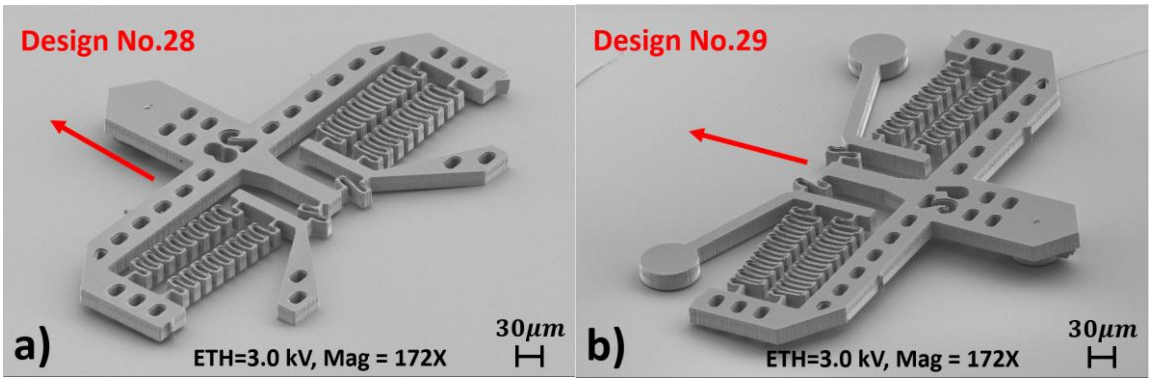

Figure 5-8 Scanning Electron Microscope images of SerpenBot designs 28 and 29, where the red arrows indicate direction (orientation) of motion.

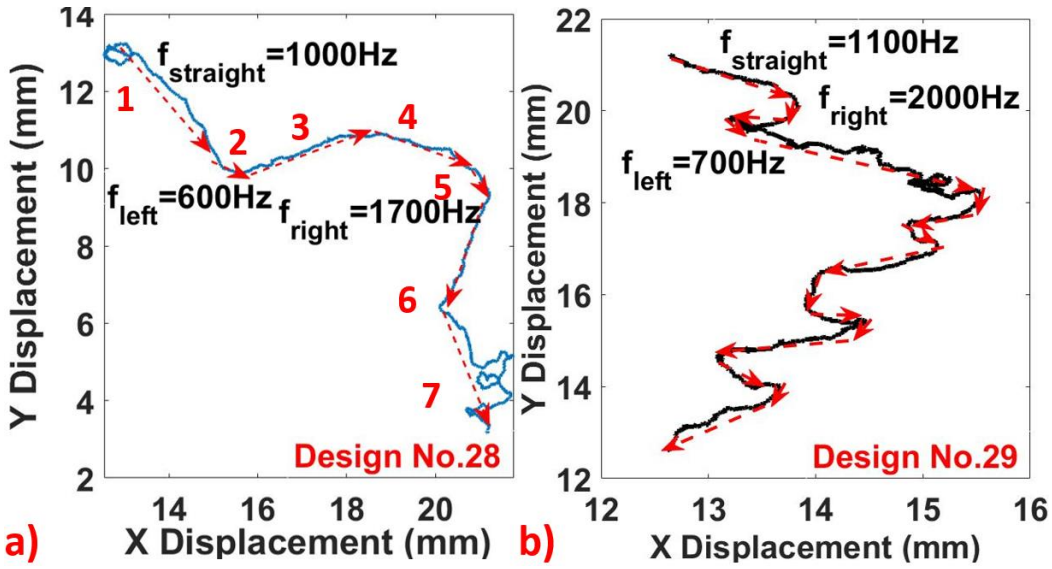

Figure 5-9 Planar steering trajectories with microrobots No.28 and No.29.

5.5 Summary

In this chapter, we have discussed the new Laser Driven Locomotive Microrobot (LDLM), SerpenBot. Comparing to the ChevBot, through modeling and experiments, we have proved that the SerpenBot has controllable behavior. In the future, we can design a close-loop controller for it.

CHAPTER 6 DESIGN AND NEURAL CONTROL OF SERPENBOT

In last chapter, we have discussed the laser driven microrobot, SerpenBot, and we have explored the frequency response features of the microrobot. In the original design, we assumed that the normal frequency difference between left and right actuators can be utilized for control of the microrobot behavior by tuning the laser pulsing frequency. However, based on empirical evidence, it was indicated that the complex nature of surface forces in the microrobot environment, brings additional difficulty in development of the control system design. In following chapter, we will discuss steering control of microrobots in dry environment through selective irradiation of the robot's body. In this work, we focused on the latter method and experimentally validate driving and steering motions of SerpenBots toward a goal. The proposed control scheme to achieve controlled steering consists of a novel Neural – Network Learning Controller (NNLC) based on deep learning. The NNLC is initially deployed through simulation using the microrobot's differential drive model. The controller was then tuned using experimental data, and results are presented in this paper demonstrating its performance. Results confirm that SerpenBot can travel to goals for significant distances greater than $1\ cm$, with translational velocity in the range of $1{\sim}100\ \mu m/s$. Lastly, as we have discussed previously, the last generation of ChevBot/SerpenBot relayed on micro-assembly involving the UV adhesive, which can melt during the laser irradiation, hence, in this chapter we also focus on the introduce new cleanroom fabrication method of SerpenBot, enabling simpler assembly process of the microrobots.

6.1 Monolithic SerpenBot Fabrication

SerpenBot is a laser-driven microrobot that shares locomotion principles with its predecessor, the ChevBot [18][58][59][60]. The SerpenBot has two asymmetrical thermal actuators, called Elbow Thermal Actuator (ETA), implemented as legs shown in Figure 6-1 and 6-2. Actuation by stick and slip principle is achieved by laser irradiation on the microrobot, at selective locations, power levels, and pulse frequencies. When the laser radiates on the surface of the microrobot, cyclic thermal expansion drives the motion on the robot legs. The actuation serpentine springs of the two legs can be designed with different spring constants, so these two actuators have different oscillation frequencies. When the modulated laser pulse is close to the actuator resonant frequency, the motion of the actuator will reach the maximum amplitude, which can be used to frequency control the turning behavior of the microrobot. Alternatively, by varying the center of the laser beam selectively onto each leg, turning behavior can also be achieved regardless of oscillation resonant frequency differentiation. In this case, the microrobot gait is achieved by the selective amplitude of vibration of each leg, coupled with the substrate using one or more dimples that double the robot thickness from $20\ \mu m$ to $40\ \mu m$, and helps tilt the robot relative to the substrate.

Recently, a preliminary study [61], identified both theoretical and experimental methods to evaluate seven different SerpenBot designs and led to the selection of best-fitting candidates for further investigation with regard to steering control. Typical design parameters for the dimensions of the SerpenBot and top and side views of the robot are presented Figure 6-3. In our past work with SerpenBots, the fabrication process included an assembly step to connect the robot body and dimple with the help of the UV adhesive.

Unfortunately, this introduced significant difficulties in maintaining robot dimensional precision and required delicate steps of aligning the dimple with the microrobot's body using a dedicated micro-assembly station [18,58]. Moreover, during operation, we often experienced decomposition of the UV adhesive at elevated temperatures during laser irradiation.

To improve the fabrication yield, we recently developed a new assembly-less fabrication process in which SerpenBot's dimple is manufactured directly on the body of the microrobot in the cleanroom, thus eliminating the need for additional assembly steps and the use of UV adhesive (Figure 6-1). The new fabrication process uses a Silicon on Insulator (SOI) wafer with 40 μm thickness device layer, and selectively etches away the device layer through 10 process steps depicted in Figure 6-2 and detailed below:

1) 300 nm SiO2 growth as a protection layer for the dimple area by Plasma-enhanced chemical vapor deposition for 10 mins @ 300 W power using an Oxford PECVD system.
2) First photolithography step with Shipley 1813 photoresist. Here we spin coat Shipley 1813 at 3000 rpm for 30 seconds, then we hard-baked the photoresist layer with 5 mins at 150℃.
3) Removal of SiO2 by buffered oxide etch (BOE) solution for approximately 5 minutes.
4) Removal of the photoresist by N-Methyl-2-pyrrolidone (NMP) bath for 5 minutes.
5) Second photolithography step with Shipley 1813 photoresist at 3000 rpm for 30 seconds, then we hard bake the photoresist layer for 5 minutes at 150℃.

6) Create the body of the microrobots by first deep reactive ion etching (DRIE) using an SPTS system process with 20 cycles set to 960 $nm/cycle$ etch rate.
7) Etch photoresist by oxygen plasma in the DRIE tool for 5 mins @ 300 W.
8) Second DRIE step to create the dimple of the microrobots. The thickness of the body and the dimple are 20 μm and 40 μm, respectively, measured from the buried oxide (BOX) layer.
9) Removal of the photoresist through an NMP bath for approximately 5 mins.
10) Release the microrobot from the wafer substrate by vapor hydrogen fluoride using a μEtch VHF system set to 6000 etch cycles taking approximately 90 mins of process time.

After completing the successful fabrication of SerpenBot, microrobot tethers are broken, and the robot is removed from the release die, and placed on a transfer die. Finally, it is transferred on a 2-inch Si wafer substrate (arena) for experiments.

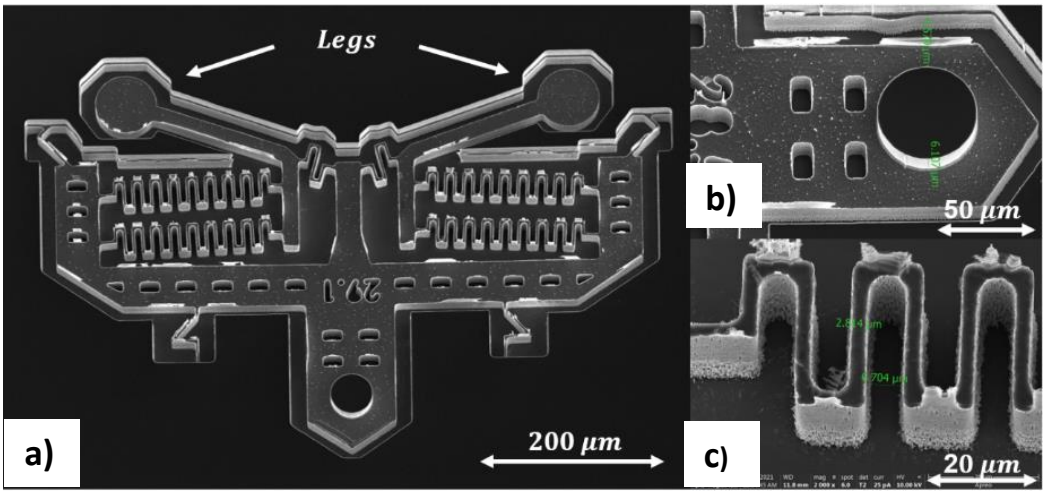

Figure 6-1 SEM images of the assembly-less SerpenBot. a) general view of the tethered microrobot, b) fabricated circular dimple, c) serpentine structures of the robot's actuator.

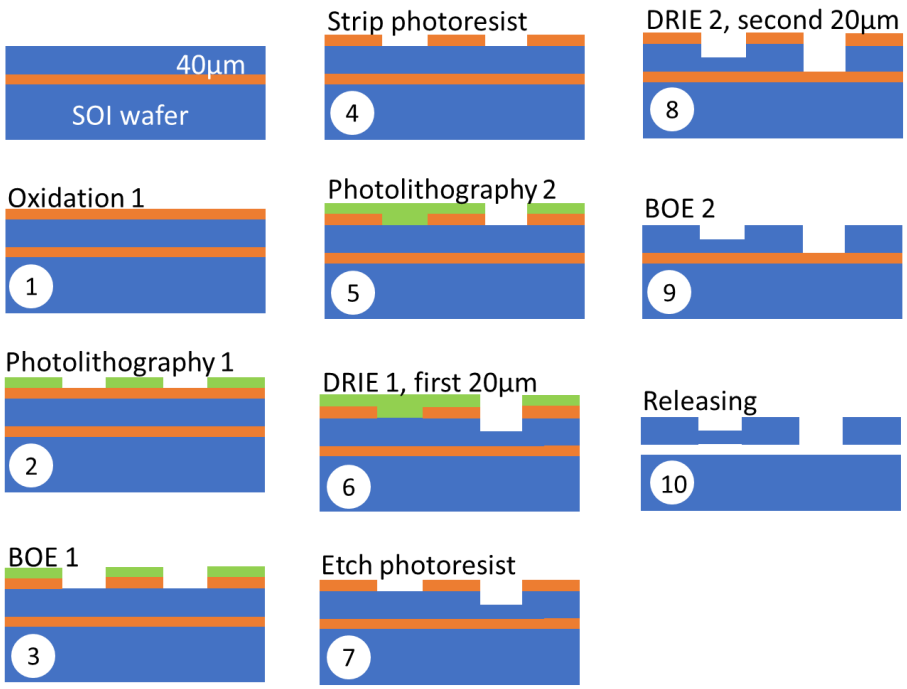

Figure 6-2 Flow chart of the cleanroom fabrication process for the assembly less SerpenBot.

The resulting microrobot has a body with approximate dimension 647 μm by 445 μm, with serpentine width 5 μm and 9 turns. This design is based on the consideration of the laser spot size, power, and pulse frequency, as detailed by our previous publications [17] [57-61].

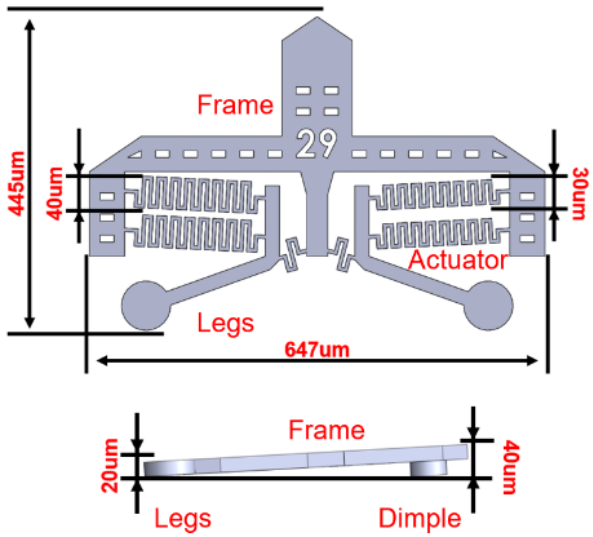

Figure 6-3 Designs of SerpenBot used in this study showing top and side views.

6.2 System Modeling

6.2.1 Dynamic Modeling

Our previous studies have revealed [24] that, SerpenBot is governed by complex opto-thermal-mechanical phenomenon, where optothermal effect is described by a first order differential equation, and the mechanical part represented by a second order differential equations, hence we have to consider a third order system. The opto-thermal behavior can be described by a following equation [24]:

$$(1-R)E_eA_l - hA_r(T-T_\infty) = \rho cV\frac{dT}{dt}, \tag{6-1}$$

where R is surface reflectivity, E_e is laser irradiation, A_l is the laser spot heating area on the robot, h is the thermal conductivity constant, A_r is the thermal diffusion area, T_∞ is the environment temperature, ρ is the material density, c is the material specific heat capacity and V is the volume of the robot.

The transient temperature change is the solution of the equation (6-1), the thermal expansion for given mechanical structure is the linear relation with the temperature as:

$$dL = \alpha L dT, \tag{6-2}$$

in which, α is the thermal expansion coefficient, L is the original length of the mechanical structure, dT is the temperature change on the structure. Since the mechanical structure of the ETA is complex but the motion of the leg of ETA relative to the geometry is small, for simplify, we can assume the force generated by the ETA is also the linear relation with the temperature which is $F \propto T$.

To describe the mechanical process, we are using Spring-Mass-Damper model, the diagram shown in Figure 6-4b, based on the following the equations of motion:

$$\boldsymbol{F_{21}} - \boldsymbol{f_{21}} - k_1[\boldsymbol{R}\cdot(\boldsymbol{x_{21}}-\boldsymbol{x_1}) - l_0] - b_1(\dot{\boldsymbol{x}}_{\boldsymbol{21}} - \dot{\boldsymbol{x}}_{\boldsymbol{1}}) = m_{21}\ddot{\boldsymbol{x}}_{\boldsymbol{21}}, \tag{6-3}$$

$$\boldsymbol{F_{22}} - \boldsymbol{f_{22}} - k_2[\boldsymbol{R} \cdot (\boldsymbol{x_{22}} - \boldsymbol{x_1}) - l_0] - b_2(\dot{\boldsymbol{x}}_{\boldsymbol{22}} - \dot{\boldsymbol{x}}_{\boldsymbol{1}}) = m_{22}\ddot{\boldsymbol{x}}_{\boldsymbol{22}}, \quad (6\text{-}4)$$

$$-\boldsymbol{F_{21}} - \boldsymbol{F_{22}} + \boldsymbol{f_1} - k_1[\boldsymbol{R} \cdot (\boldsymbol{x_1} - \boldsymbol{x_{21}}) - l_0] - k_1[\boldsymbol{R} \cdot (\boldsymbol{x_1} - \boldsymbol{x_{22}}) - l_0] -$$

$$b_1(\dot{\boldsymbol{x}}_{\boldsymbol{1}} - \dot{\boldsymbol{x}}_{\boldsymbol{21}}) - b_1(\dot{\boldsymbol{x}}_{\boldsymbol{1}} - \dot{\boldsymbol{x}}_{\boldsymbol{22}}) = m_1\ddot{\boldsymbol{x}}_{\boldsymbol{1}}, \quad (6\text{-}5)$$

$$I\ddot{\varphi} = \boldsymbol{r_{21}} \times \boldsymbol{F_{21}} + \boldsymbol{r_{22}} \times \boldsymbol{F_{22}}, \quad (6\text{-}6)$$

where bold letters represent 2-dimensional force vectors, $\boldsymbol{F_{21}}$ and $\boldsymbol{F_{22}}$ generated by two ETAs, $\boldsymbol{f_1}$ is the friction force between dimple of robot and substrate's surface, $\boldsymbol{f_{21}}$ and $\boldsymbol{f_{22}}$ are the friction forces acting on legs, $\boldsymbol{R}$ is the rotational matrix.

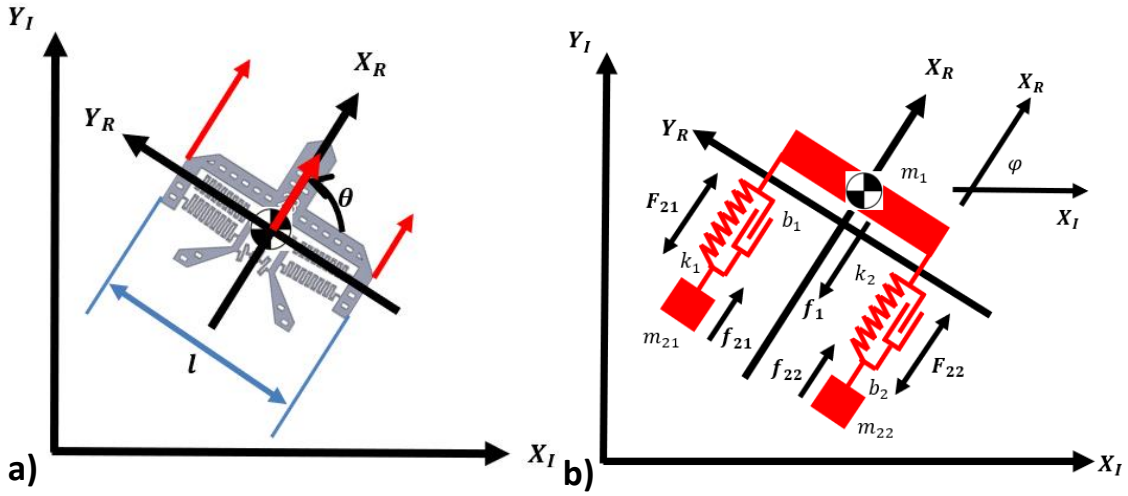

Figure 6-4 Kinematic model of SerpenBot: a) kinematic model diagram of the SerpenBot, b) dynamic model: force diagram for Spring-Mass-Damper model.

6.2.2 Differential Drive Kinematics

The simplified kinematics of the robot can be described as a mapping between leg velocities in a local frame and robot velocity in a global frame depicted in Figure 6-4a, and represented by states $\dot{q}^R = [\dot{x}^R\ \dot{y}^R]^T, \dot{q}^G = \left[\dot{x}^G\ \dot{y}^G\ \dot{\theta}^G\right]^T$, in which $\dot{x}^R$ and $\dot{y}^R$ are the velocity of the robot legs in the local frame, while $\dot{x}^G$, $\dot{y}^G$, $\dot{\theta}^G$ are the linear and angular velocities of the robot in the global frame. The relationship between $\dot{q}^R$ and $\dot{q}^G$ can be further described through the Jacobian matrix of the robot J_{rob} as:

$$\dot{q}^R = J_{rob}\dot{q}^G, \tag{6-7}$$

Through numerical difference expansion and integration, we can approximate the robot location in a discrete-time fashion according to:

$$\begin{bmatrix} x_k^G \\ y_k^G \\ \theta_k^G \end{bmatrix} = \begin{bmatrix} cos\,\theta_{k-1}^G & -sin\,\theta_{k-1}^G & 0 \\ sin\,\theta_{k-1}^G & cos\,\theta_{k-1}^G & 0 \\ 0 & 0 & 1 \end{bmatrix} \begin{bmatrix} \frac{1}{2} & \frac{1}{2} \\ 0 & 0 \\ -\frac{1}{l} & \frac{1}{l} \end{bmatrix} \begin{bmatrix} \dot{x}_l^R \\ \dot{x}_r^R \end{bmatrix} \Delta t + \begin{bmatrix} x_{k-1}^G \\ y_{k-1}^G \\ \theta_{k-1}^G \end{bmatrix}, \tag{6-8}$$

where k represents a time step index, l is distance between the legs of the robot, and Δt is the sampling time. Since the motion of the leg occurs only along one direction parallel to X_R, we can use scalars $\dot{x}_l^R$ and $\dot{x}_r^R$ to represent the robot right leg and left leg velocity. These velocities can be described as a second order system, a function of pulsed laser energy and frequency inputs as:

$$\dot{x}_{l,r}^R = \frac{K_l I}{\sqrt{\left[1-\left(\frac{f}{f_n}\right)^2\right]^2 + \left[2\zeta\left(\frac{f}{f_n}\right)\right]^2}}, \tag{6-9}$$

where f_n is the actuator resonant frequency, ζ is damping ratio, K_l is the gain of the laser, an empirical value, and I is the laser current.

By describing the motion of the SerpenBot as a differential drive robot, if we can realize a scenario where each leg of the robot moves at different pace (different velocity), we can change the turning behavior of the robot. Therefore, our control strategy involves laser beam heating of selected actuator of the robot each time we want to drive different leg, and in a result to run the whole SerpenBot in a desired direction. We called this scheme depicted in Figure 6-5b Right-Forward-Left control (RFL).

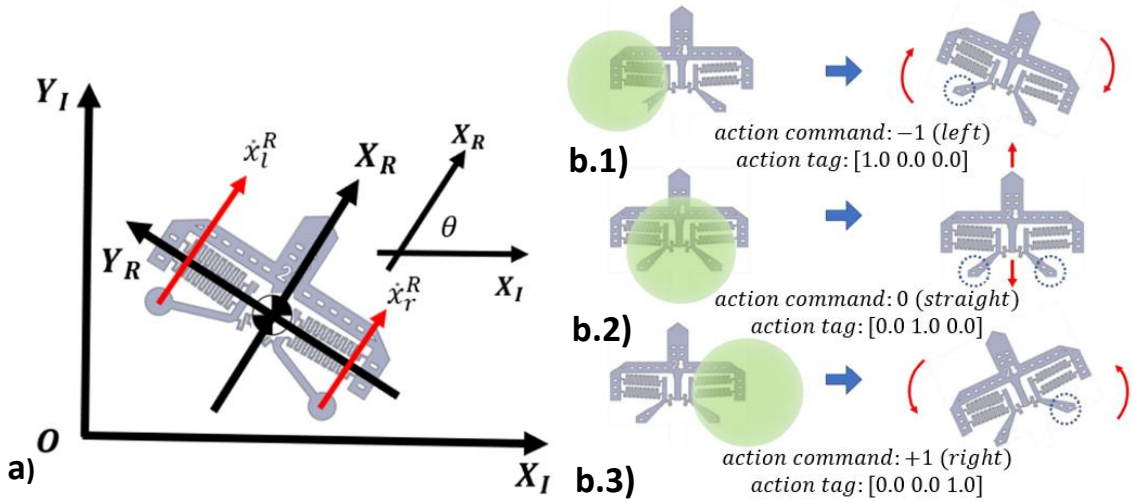

Figure 6-5 SerpenBot steering scheme based on selective irradiation. a) kinematic model of the SerpenBot b.1) clockwise (counterclockwise) motion, b.2) forward (backward) motion, b.3) counterclockwise (clockwise) motion. (Red arrows represent orientation and direction of the motion. Dashed circles indicate which actuator pair and leg is activated. Green circle represents laser spot irradiating selected part of microrobot.

6.2.3 Theory of neural networks control stability

Definition 6.1 The nonlinear system $\dot{x} = f(x,t)$ is said to be autonomous if f does not depend on time explicitly, otherwise, the system is nonautonomous system.[60][61]

Definition 6.2 For an autonomous system $\dot{x} = f(x)$, the state $x^* \in \mathcal{D}$ is an equilibrium point of the system, if $f(x^*) = 0$, where domain $\mathcal{D} \subseteq \mathbb{R}^{\boldsymbol{n}}$. Without loss of generality, $x^* = 0$. [60][61]

From last section discussion, our robot is a nonlinear nonautonomous system, we can formulate it as the vector form:

$$\dot{x} = f(x,u), \tag{6-10}$$

where $f: \mathcal{D} \to \mathbb{R}^{\boldsymbol{n}}$ is a continues mapping from a domain $\mathcal{D} \subseteq \mathbb{R}^{\boldsymbol{n}}$ into $\mathbb{R}^{\boldsymbol{n}}$, and $x(t) \in \mathbb{R}^{\boldsymbol{n}}$ is the system state and $u(t) \in \mathbb{R}^{\boldsymbol{n}}$ is the control parameters. Since a nonautonomous system can be converted to an autonomous system by increasing its dimension by one, without loss of generality, the system can be defined as

$$\dot{x} = f(x), \tag{6-11}$$

where $f: \mathcal{D} \to \mathbb{R}^{\boldsymbol{n}}$ is a continues mapping from a domain $\mathcal{D} \subseteq \mathbb{R}^{\boldsymbol{n}}$ into $\mathbb{R}^{\boldsymbol{n}}$, $x \in \mathcal{D} \subseteq \mathbb{R}^{\boldsymbol{n}}$ is the system state.

Definition 6.3 Lyapunov stable, for an autonomous system $\dot{x} = f(x(t))$, $x(t_0) = x_0$, where $x(t) \in \mathcal{D} \subseteq \mathbb{R}^{\boldsymbol{n}}$. The system is Lyapunov stable around equilibrium point x^* if $\forall \epsilon > 0, \exists \delta > 0$, such that, if $\|x(t_0) - x^*\| < \delta$, then $\|x(t) - x^*\| < \epsilon,\ \forall t \geq t_0$. [60][61]

Definition 6.4 Asymptotically stable, for an autonomous system $\dot{x} = f(x(t))$, $x(t_0) = x_0$, where $x(t) \in \mathcal{D} \subseteq \mathbb{R}^{\boldsymbol{n}}$. The system is asymptotically stable around equilibrium point x^*, if $\exists \delta > 0$, such that if $\|x(t_0) - x^*\| < \delta$, then $\lim_{t \to \infty} \|x(t) - x^*\| = 0$. [60][61]

Theorem 6.1 Lyapunov's indirect method, consider system autonomous system $\dot{x} = f(x)$, if $f: \mathcal{D} \to \mathbb{R}^{\boldsymbol{n}}$ continuously differentiable around equilibrium point $x^* \in \mathcal{D}$, where $\mathcal{D}$ is the neighborhood domain of x^*, then,

$$\dot{x} = Ax + h(x), \tag{6-12}$$

where A is Jacobian matrix,

$$A = \frac{\partial f}{\partial x}\Big|_{x=x^*} = \begin{bmatrix} \frac{\partial f_1}{\partial x_1} & \cdots & \frac{\partial f_1}{\partial x_n} \\ \vdots & \ddots & \vdots \\ \frac{\partial f_n}{\partial x_1} & \cdots & \frac{\partial f_n}{\partial x_n} \end{bmatrix}_{x=x^*}, \tag{6-13}$$

and $h(x) \coloneqq \|f(x) - Ax\|$ represents higher-order terms, and denote eigenvalues of A as $\{\lambda_i\}_{i=1}^n$

then,

a) If $Re(\lambda_i) < 0, i = 1, \dots, n$, then the system is asymptotically stable around x^*, then $h(x) \coloneqq \|f(x) - Ax\| < \epsilon, \forall \epsilon > 0$
b) If $Re(\lambda_i) > 0, i = 1, \dots, n$, then the system is unstable around x^*, then $h(x) \coloneqq \|f(x) - Ax\| > \epsilon, \forall \epsilon > 0$. [60][61]

Remark: The SerpenBot is driven by laser pulses, each laser pulse's energy is bounded, and considering the friction force and damping, the SerpenBot are moving around equilibrium points, the system can be considered as asymptotically stable according to the experiments observations.

Next, we are going to introduce the extension of the Lyapunov's indirect method with neural networks.

Theorem 6.2 Universal approximation theorem, let $\sigma: \mathbb{R} \to \mathbb{R}$ be a nonlinear continuous activation function, the $C[0,1]^m$ is the real-valued continuous functions space. For $\forall \varepsilon > 0$, and $\forall f \in C[0,1]^m$, then $\exists N \in \mathbb{Z}$, $\exists v_i, b_i \in \mathbb{R}$ and $\exists \omega_i \in \mathbb{R}^m$, for $i \in \{1, \dots, N\}$, such that $\|f(x) - F(x)\| < \varepsilon, \forall x \in [0,1]^m$, where approximation function $F(x)$ defined as[62]

$$F(x) := \sum_{i=1}^{N} v_i \sigma(\omega_i^T x + b_i) = v^T \sigma(\omega^T x + b). \tag{6-14}$$

Theorem 6.3 For an autonomous system $\dot{x} = f(x)$, and $f: \mathcal{D} \to \mathbb{R}^{\boldsymbol{n}}$ continuously differentiable around equilibrium point $x^* \in \mathcal{D}$, where $\mathcal{D}$ is the neighborhood domain of x^*, then $\dot{x} = F(x) + g(x)$ is asymptotically stable around x^*, if $\dot{x} = Ax + h(x)$ is

asymptotically stable around x^*, where $F(x)$ is neural networks approximation function defined in theorem 6.2, and $g(x) \coloneqq \|f(x) - F(x)\|$ represents higher-order terms.

Proof: according to theorem 6.1 the high order term of linearization is $h(x) \coloneqq \|f(x) - Ax\|$ and the high order term of neural networks approximation is $g(x) \coloneqq \|f(x) - F(x)\|$, since $F(x)$ is higher order model than linear model, then $g(x)$ is bounded by $h(x)$, which mean $\|f(x) - F(x)\| \leq \|f(x) - Ax\|$. Assume linearization is asymptotically stable around x^*, and through squeeze theorem, we have $0 \leq \|f(x) - F(x)\| \leq \|f(x) - Ax\| < \epsilon$, $\forall \epsilon > 0$, then $\dot{x} = F(x) + g(x)$ is asymptotically stable around x^*. ■

Remark: the theorem 6.3 is using nonlinear model, neural networks replace linear model, the proof shows that neural networks converge to the equilibrium point bounded by linear model. This is given us a powerful tool to approximate system dynamics by using neural networks, since the intrinsic nonlinearity of neural networks, and capability of classification and decision-making of the neural networks, it is given us the tool for controlling discrete and continues parameters of a system simultaneously. In normal nonlinear control, we should find Lyapunov function to proof the stability of a system or a controller, however, since the complexness of the structure of the neural networks, find Lyapunov function become to challenge, so in here, we have extended and generalized the Lyapunov indirect method to be for neural networks applications. The theorem 6.3 also can be generalized for kinematic system, the proof will follow the same principle.

Theorem 6.4 For a mapping $\dot{x} = f(u)$, where $f: \mathcal{D} \to \mathbb{R}^{\boldsymbol{n}}$, and $u \in \mathcal{D}$, $\dot{x} \in \mathbb{R}^{\boldsymbol{n}}$, then $\exists g \in C[0,1]^m$ as approximation function, and $u = g(\dot{x})$, $g: \mathbb{R}^{\boldsymbol{n}} \to \mathcal{D}$, such that $\mathrm{id}_{\mathcal{D}} = f \circ g$ around x^*, where $\mathrm{id}_{\mathcal{D}}$ is and identity mapping $\mathrm{id}_{\mathcal{D}}: \mathcal{D} \to \mathbb{R}^{\boldsymbol{n}}$.

Proof: the inverse of mapping of f is f^{-1}, then $\mathrm{id}_{\mathcal{D}} = f \circ f^{-1}$. According to theorem 6.2 and 6.3, then around x^*, we have $\|f^{-1}(\dot{x}) - g(\dot{x})\| < \epsilon, \forall \epsilon > 0$, since ϵ is an infinitesimal number, then we have $f^{-1}(\dot{x}) = g(\dot{x})$, hence $\mathrm{id}_{\mathcal{D}} = f \circ g$. ■

Remark: given a kinematic of a system, through theorem 6.4 we can utilize neural networks construct an inverse kinematic of the system, then combine kinematic and inverse kinematic, the system can be approximated as linear system.

6.2.4 PID-Bayes Controller

The dynamics of the SerpenBot is through first principle from thermal dynamic and newton's law, however, the physics properties of SerpenBot system bring hardness to measure and modeling the dynamics of the system, such as legs vibrations behavior, opto-thermal behavior, and surface friction constants. Though, those physics parameters cannot directly be measured by experiments, in real experiment setups, the state of the robot is always measurable, hence, the phenomenology description of the system becomes necessary. In here we introduced the forward kinematics and inverse kinematics describing the system behavior.

Assume the robot is a described by a kinematic mapping function $\dot{x} = f(u)$ between control parameters u and state $\dot{x}$, where $f: \mathcal{D} \to \mathbb{R}^{\boldsymbol{n}}$, $u \in \{u | d \otimes c, d \in \mathbb{Z}, c \in \mathbb{R}\} \subseteq \mathcal{D}$, $x \in \mathbb{R}^{\boldsymbol{n}}$, and $\mathcal{D}: \mathbb{Z} \times \mathbb{R}$. d is a discrete control variable for decision making, and c is for continues control variable. Let us define the error dynamics of the system,

$$e = x_c - x_d, \tag{6-15}$$

and

$$\dot{e} = \dot{x}_c, \tag{6-16}$$

where $e \in \mathbb{R}^{\boldsymbol{m}}$, $x_c \in \mathbb{R}^{\boldsymbol{m}}$ is current configuration of the robot and $x_d \in \mathbb{R}^{\boldsymbol{m}}$ is the desired configuration of the robot. Since the control variable $u \subseteq \mathcal{D}$ combined discrete and continues variables, the error dynamic cannot directly used for control, we need coordinate transformation. According to theorem 6.4, we can introduce neural network as inverse kinematic which can be defined as $u = g(\dot{x})$, $g: \mathbb{R}^{\boldsymbol{n}} \to \mathcal{D}$, such that $\mathrm{id}_{\mathcal{D}} = f \circ g$, $\mathrm{id}_{\mathcal{D}}: \mathcal{D} \to \mathbb{R}^{\boldsymbol{n}}$. Then the robot with inverse kinematic together can be seen as linear system, and function g can be utilized as mapping from $\mathbb{R}^{\boldsymbol{n}}$ to $\mathcal{D}$, we can define a PID controller with coordinate transformation as:

$$v = PID(e), \tag{6-17}$$

where PID output $v \in \mathbb{R}^{\boldsymbol{n}}$, and $PID: \mathbb{R}^{\boldsymbol{m}} \to \mathbb{R}^{\boldsymbol{n}}$. Hence, our controller in discrete form can be expressed as:

$$x_k = f \circ g \circ PID(x_{k-1} - x_d) * \Delta t + x_{k-1}, \tag{6-18}$$

The structure of the controller shows in figure 6-6.

The inverse kinematic g is a neural network, now we need to formulate the learning process of g. We can use supervised learning to form g. Since $u \subseteq \mathcal{D}$ is a simi-discrete domain (each $d \in \mathbb{Z}$ in u are discrete), u can be seen as a tag for learning, then g can be seen as a Naïve Bayes Classifier with parameters Θ , then we have.

$$\hat{u} = \underset{k \in \{1,\dots,K\}}{\operatorname{argmax}} \; p(u_k) \prod_{i=1}^{n} p(\dot{x}_i | u_k, \theta), \theta \in \Theta. \tag{6-19}$$

The learning process is shown in Figure 6-7.

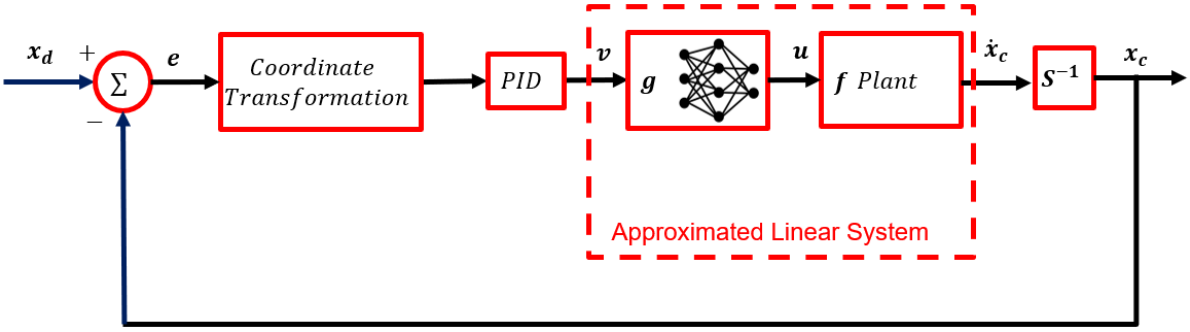

Figure 6-6 the PID-Bayes controller diagram.

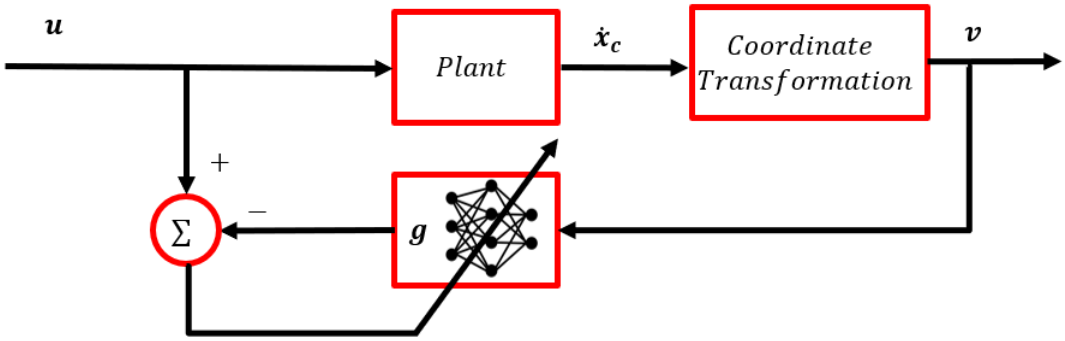

Figure 6-7 The learning framework of neural-network of the PID-Bayes controller.

6.3 SerpenBot Controller Design

To develop a controller for the SerpenBot and implement the steering strategy, we must consider a scheme in which the laser spot position is synchronized with respect to the motion of the microrobot on the substrate. In our microrobot driving system, described in more detail in section 6.4, the substrate, also called the arena, is moved via three micropositioning stages under a fixed laser spot delivered from a $532\ nm$ green pulsed $2\ W$ laser unit. Thus, our control system consists of two main parts: 1) visual servoing for laser spot control and 2) steering microrobot behavior control. Since the SerpenBot is

moving on the arena and the position of laser spot is fixed, the visual servoing system is continuously keeping selected parts of the robot under the laser beam (Figure 6-5b). Furthermore, the microscope camera provides feedback to always keep the robot legs and body irradiated by the laser in the center of the field of view. The robot steering behavior control system consists of PID Neural Right-Forward-Left (PID-N-RFL) scheme that irradiates selected microrobot's actuators (left actuator, right actuator, or both), while the varying intensity of the laser beam (laser diode current) can be used to change the turning radius of the robot. To describe our controller, we refer to Figure 6-5a showing what the microscope image (camera's field of view (FOV)) of the robot will look like, while the overall control block diagram is shown in Figure 6-8.

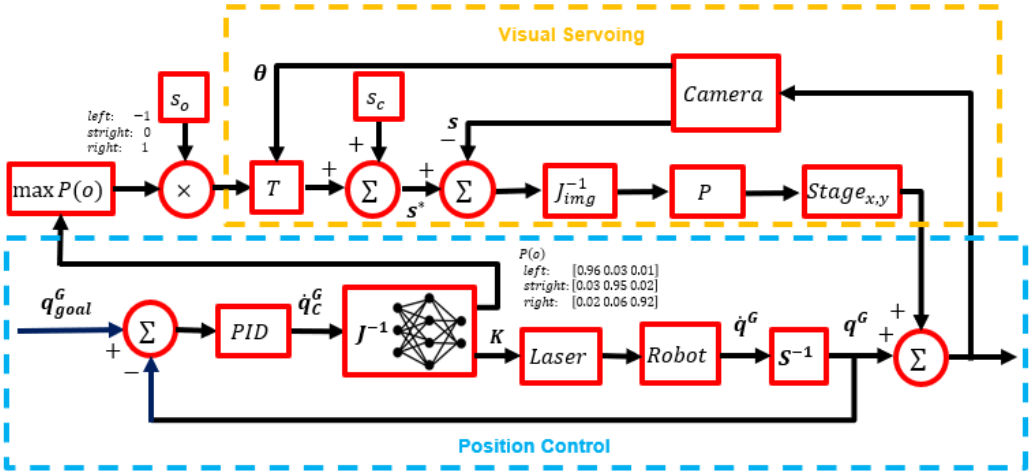

Figure 6-8 PID-N-RFL Controller block diagram.

6.3.1 Visual Servoing

A visual servoing controller is necessary to track robot during its motion by keeping it irradiated, e.g., within the same area in a FOV of a camera, with the help of motorized *X-Y* stages located under the robot arena. In this arrangement, control error is the difference between robot current location in pixel coordinates s_r^P, and desired point in FOV of camera

center of the FOV (center) s_c^P. Error mapping serves as a control value for the *X-Y* stages and is realized with the help of inverse image Jacobian matrix J_{img}^{-1} for transformation from pixel space to Cartesian space of *X-Y* stages. (Figure 6-8)

The image Jacobian matrix is described as follows:

$$\dot{s}^P = J_{img}\dot{q}^G = \begin{bmatrix} \frac{\partial s_x}{\partial x^G} & \frac{\partial s_x}{\partial y^G} & \frac{\partial s_x}{\partial \theta^G} \\ \frac{\partial s_y}{\partial x^G} & \frac{\partial s_y}{\partial y^G} & \frac{\partial s_y}{\partial \theta^G} \end{bmatrix} \begin{bmatrix} \dot{x}^G \\ \dot{y}^G \\ \dot{\theta}^G \end{bmatrix}. \tag{6-20}$$

We can identify the image Jacobian matrix by acquiring set of random points based on the motion of the motorized *X-Y* stages and recording from the smart camera, as a result, the regression equation for identification of the image Jacobian is [62]:

$$J_{img,k+1} = J_{img,k} + \frac{(\Delta s_k - J_{img,k}\Delta q_k)\Delta q_{G,k}^T}{\Delta q_{G,k}^T \Delta q_{G,k}}, \tag{6-21}$$

where $\Delta s_{P,k} = s_{P,k} - s_{P,k-1}$ and $\Delta q_{G,k} = q_{G,k} - q_{G,k-1}$. After identifying Image Jacobian matrix, we implemented only proportional (P) controller, determining control equation:

$$q_{G,k+1} = q_{G,k} + K_{img}\left(J_{img,k}^T J_{img,k}\right)^{-1} J_{img,k}^T (s_c^P - s_r^P), \tag{6-22}$$

where K_{img} is the gain of the control value for visual servoing, s_c^P is the center coordinate of the camera in camera space.

6.3.2 Homogenous coordinates transformation for action switching

Through visual servoing we establish a method for centering the microrobot in the microscope field of view, which coincides with the center of the laser spot. We can then apply the visual servoing strategy to switching the location of the laser spot in different parts of the robot in particular on each of the SerpenBot's legs. We employ a homogeneous coordinates transformation to redirect the laser spot onto desired parts of the SerpenBot for steering control. Figure 6-9 shows a diagram of our SerpenBot under the camera field of

view, and we employ visual servoing to make the laser spot overlap with the geometric center of the robot, to the left leg center, and right leg center. Assuming a laser spot offset $\tilde{s}_{R,o}^{P} := \left[x_{R,o}^{P}\ y_{R,o}^{P}\ 1\right]^{T}$ relative to the center of the robot in the local frame, through a rotation matrix $R(\theta)$ and transformation matrix $T(\tilde{s}_{r}^{P}, \theta)$ with the center coordinate of the SerpenBot $\tilde{s}_{r}^{P} := [x_{r}^{P}\ y_{r}^{P}\ 1]^{T}$ in homogenous camera space, we can calculate the laser spot offset $\tilde{s}_{o}^{P} := [x_{o}^{P}\ y_{o}^{P}\ 1]^{T}$ in homogenous camera space as $\tilde{s}_{o}^{P} = T(\tilde{s}_{r}^{P}, \theta)R(\theta)\tilde{s}_{R,o}^{P}$, as:

$$\begin{bmatrix} x_o^P \\ y_o^P \\ 1 \end{bmatrix} = \begin{bmatrix} 1 & 0 & x_r^P \\ 0 & 1 & y_r^P \\ 0 & 0 & 1 \end{bmatrix} \begin{bmatrix} cos\,\theta & sin\,\theta & 0 \\ -sin\,\theta & cos\,\theta & 0 \\ 0 & 0 & 1 \end{bmatrix} \begin{bmatrix} x_{R,o}^P \\ y_{R,o}^P \\ 1 \end{bmatrix}, \tag{6-23}$$

or:

$$\begin{bmatrix} x_o^P \\ y_o^P \\ 1 \end{bmatrix} = \begin{bmatrix} \cos\theta & \sin\theta & x_r^P \\ -\sin\theta & \cos\theta & y_r^P \\ 0 & 0 & 1 \end{bmatrix} \begin{bmatrix} x_{R,o}^P \\ y_{R,o}^P \\ 1 \end{bmatrix}. \tag{6-24}$$

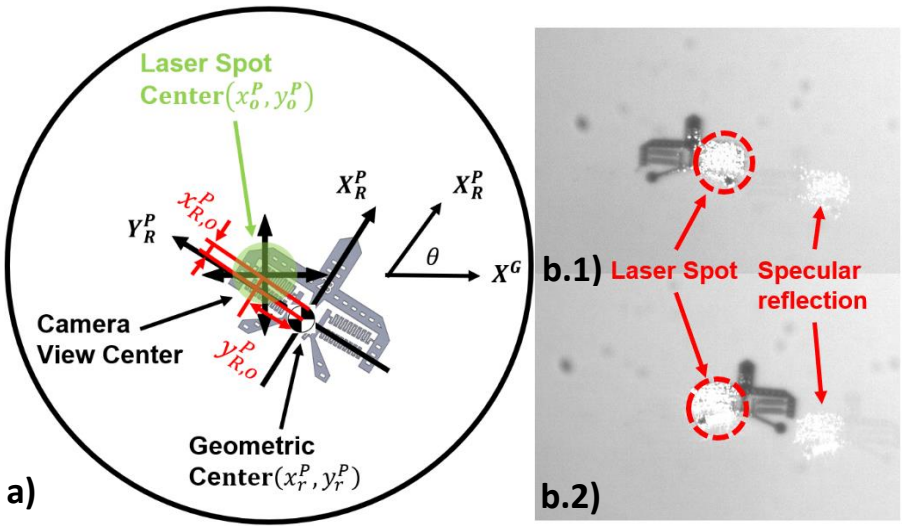

Figure 6-9 Laser spot switching using visual servoing for microrobot steering. The laser spot to the left in each figure is a specular reflection from camera lens and substrate, and not a second laser spot.

Given a laser spot offset relative to the center of the robot, we can calculate the laser spot offset in camera space for visual servoing, by converting $\tilde{s}_o^P$ in homogenous camera space to $s_o^P \coloneqq [x_o^P \; y_o^P]^T$ in normal camera space. Finally, to move the laser beam location to the desired spot, we simply implement equation (6-22).

6.3.3 PID-N-RFL controller

The PID Neural Right-Forward-Left (PID-N-RFL) controller, shown in Figure 6-8, is proposed for controlling the motion of SerpenBot to reach a specific goal location on the substrate. The PID-N-RFL controller is an application of the PID-Bayes controller discussed in the previous section. The Right-Forward-Left action can be classified as a category of SerpenBot behavior, allowing the control problem to be converted to a classification problem. The PID controller maps the error between current configuration $[x_c^G \; y_c^G \; \theta_c^G]^T$ and goal configuration $[x_d^G \; y_d^G \; \theta_d^G]^T$ by setting the robot velocity in polar coordinates $\dot{q}_C^G = [v_c^G \; \omega_c^G]^T$, including its forward velocity v_c^G and turning velocity ω_c^G as:

$$v_c^G = K_v \cdot \sqrt{e_x^2 + e_y^2}, \tag{6-25}$$

$$\omega_c^G = PID(e_\theta), \tag{6-26}$$

where K_v is the gain for linear velocity, PID parameter including $K_{\omega,P}$, $K_{\omega,I}$, and $K_{\omega,D}$ are the gain for the angular velocity, $e_x = x_c^G - x_d^G$, $e_y = y_c^G - y_d^G$ and $e_\theta = \theta_c^G - \theta_d^G$, are the controller position and orientation errors, and θ_d^G is defined as the desired directional angle toward the goal:

$$\theta_d^G = atan2(e_x, e_y), \tag{6-27}$$

The PID-N-RFL controller is very flexible to apply, as it only requires one discrete variable as tag for decision making on what part of the robot to apply the laser spot, and

one continuous variable for velocity control. To validate this controller, we began by selecting the laser current as the continuous control variable determining velocity and conducted simulations. However, through experiments we later found that the offset distance is a better choice of control variable since the SerpenBot's angular velocity is more responsive to this variable.

We define the control variable C as belonging to a semi-discrete domain, $C \in \{c|A \otimes K, A \in \{-1,0,1\},\ K \in [0,1]\}$, including discrete actions A (RFL) and normalized continuous laser current K. We propose to use a neural network to approximate the robot inverse Jacobian J_{rob}^{-1} as a bridge mapping the continuous value of the PID controller to be semi-discrete space of the actual control value which is $C = J_{rob}^{-1}\dot{q}_C^G$. The neural network approximating J_{rob}^{-1}, is shown in Figure 6-10.

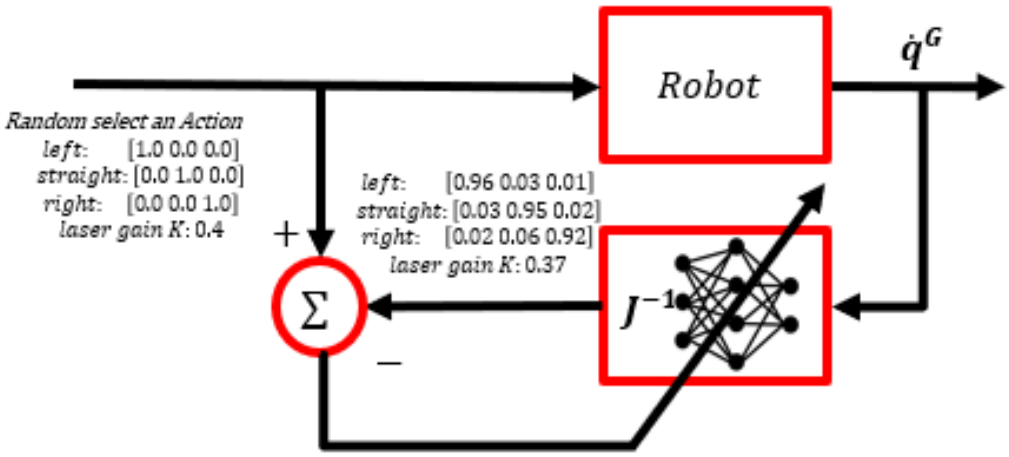

Figure 6-10 Learning scheme of the SerpenBot's inverse kinematics by applying a set of random action and gains, collecting batch data, and fitting an inverse Jacobian mapping.

We used a supervised learning method to train the neural network with tags defined as right, forward, and left for representing the RFL and the laser gain values. For training the system, these tags and the normalized laser current are randomly selected as actions.

After applying actions to the system, the system output is related to the microrobot state velocity $\dot{q}^G$, expressed as a pair with scalar velocity $v^G = \sqrt{(\dot{x}^G)^2 + (\dot{y}^G)^2}$ and angular velocity $\omega^G = \dot{\theta}^G$ of the robot is sent back to the neural network. At the end of training process, the neural network acts as a classifier which finds the occurrence probability of the input actions. However, during the training process, the difference of the tags and output probabilities with the laser gain will back propagate to update the parameters of the neural network. Finally, the neural network learns to get the current states of the microrobot as input and finds the laser behavior RFL as output. That makes the neural network J_{rob}^{-1} a classifier as well as a tool to calculate the inverse kinematics of the robot.

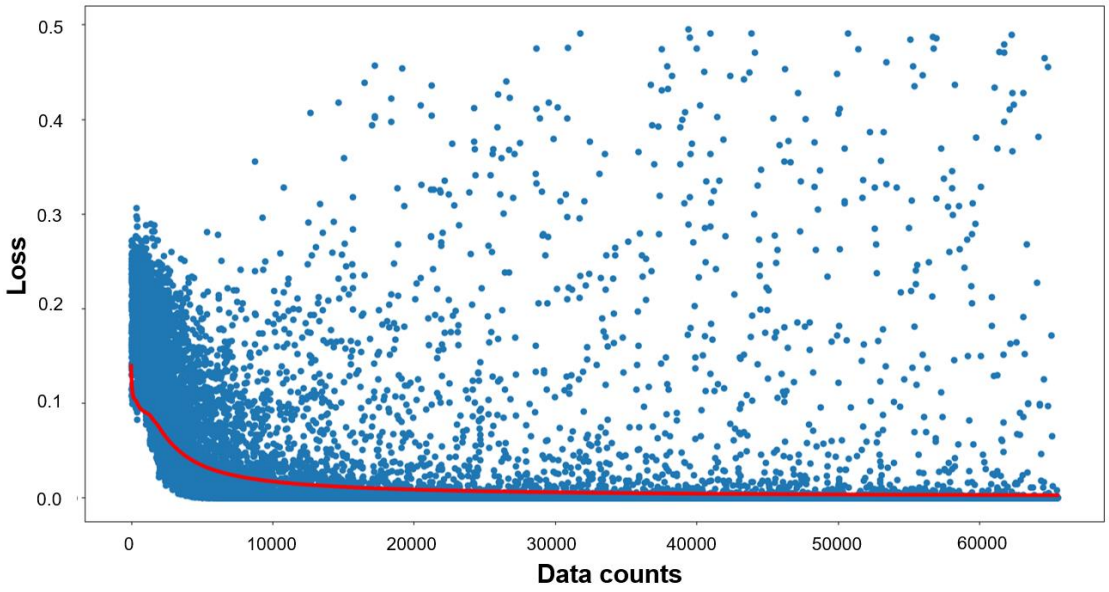

Figure 6-11 The loss functions during the learning process represented by blue dots after 70000 training points. The red line is the average loss during learning.

In practice, we constructed our neural network using PyTorch (® open-source library with two hidden layers of 128 neurons each and selected “tanh”, as activation function for the hidden layers, and selected a learning rate of 0.00017. The output layer

includes four outputs: right, forward, and left (defined tags) as well as offset relative to the center of the SerpenBot in pixel. The activation functions for the NN output were both "softmax" for action switching, and "sigmoid" for the laser gain.

Figure 6-10 presents training results of the proposed neural network. For this process, we first use the kinematic model to train the neural network, then through transfer leaning, we continued training the neural network with experimental data collected during steering. Results show that the loss function converges to very small values under the pre-described threshold, demonstrating the promising ability of the neural network to model the robot inverse kinematic from image data.

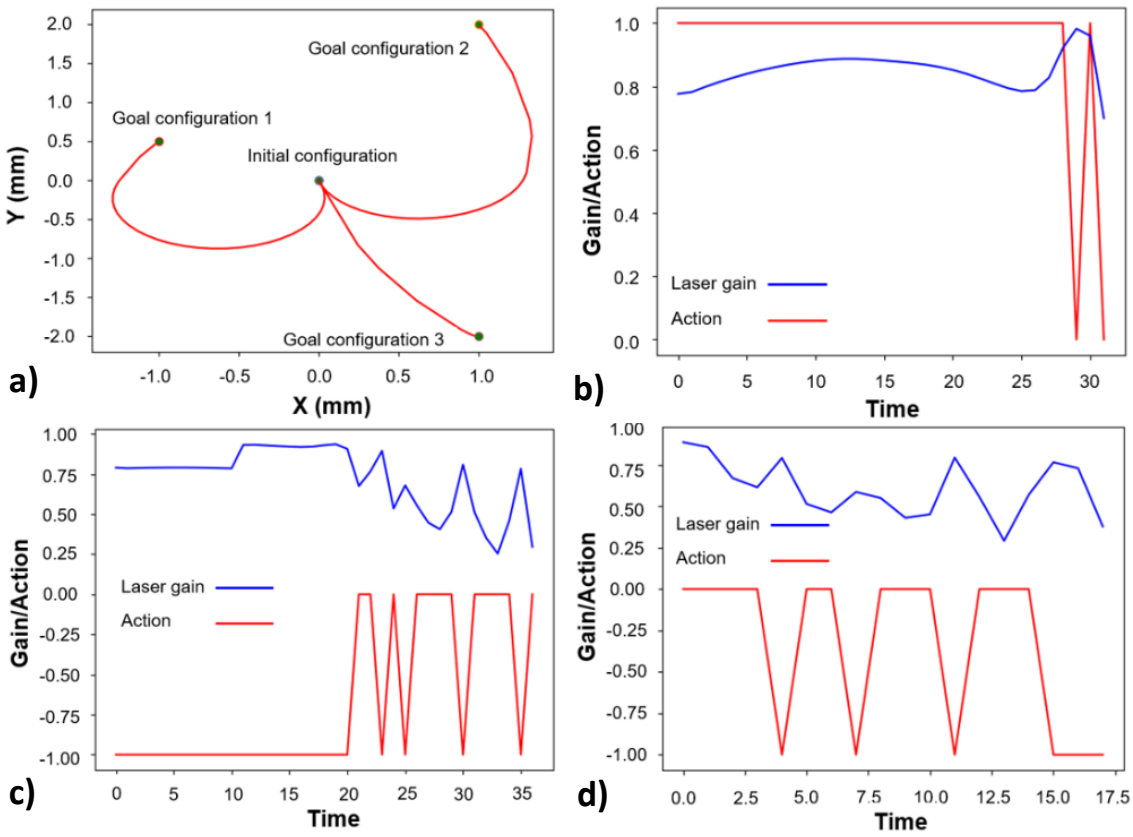

Figure 6-12 a) simulation results of the controller reaching random goal locations, b, c, d) the control parameters for reaching the goal locations in a).

While training our neural network we have simulated the robot to drive and steer with three distinct states: left, forward, or right depending on the laser irradiation of the selected part of SerpenBot (Figure 6-12). Simulation results show that we were able to realize three different trajectories necessary for microrobot control: clockwise/counterclockwise revolutions, and translational motion.

6.4 Experimental Methods

6.4.1 Experimental setup

A schematic view of the experimental setup to drive the SerpenBot is depicted in Figure 6-13. As source of laser light for microrobot's actuation, we have used high power Nd: YAG pulse laser (Spectra-Physics Explorer® one) with wavelength of $532\ nm$. The pulse frequency can be adjusted between $0.5{\sim}60\ kHz$, the pulse time width and average output power can be adjusted between $10{\sim}40\ nm$ and $0{\sim}2\ W$ respectively. A variable neutral density filter (NDF) followed by the Uniblitz optical shutter was used to attenuate laser beam during experiments. A system of two lenses adjacent to NDF allows adjustment of the size of laser spot and position of the laser beam is adjusted by varying tilt of 4 mirrors (M1-M4). Two cameras integrated with beam splitter were attached to two tube lenses: one, a National Instrument smart camera (ISC-1772C) was used for visual servoing; second, a Pixelink PL-D734, was used as real time visual feedback for SerpenBot. The microrobots are placed on an arena consisting of a 2-inch Si wafer, which was secured on a sample chuck and positioned on top of four cascaded linear stages. Two of the stages are manually controlled for calibrated adjustments, while the other two are motorized (PI Q-521), controlled by National Instrument LabVIEW, and used for automated tracking and control of SerpenBot's motion. A custom LabVIEW user interface (UI) allows adjustment of the

laser spot position relative to the SerpenBot's body thus allowing irradiation of the selected actuator and results in automated or semi-automated steering of the robot (Figure 6-9).

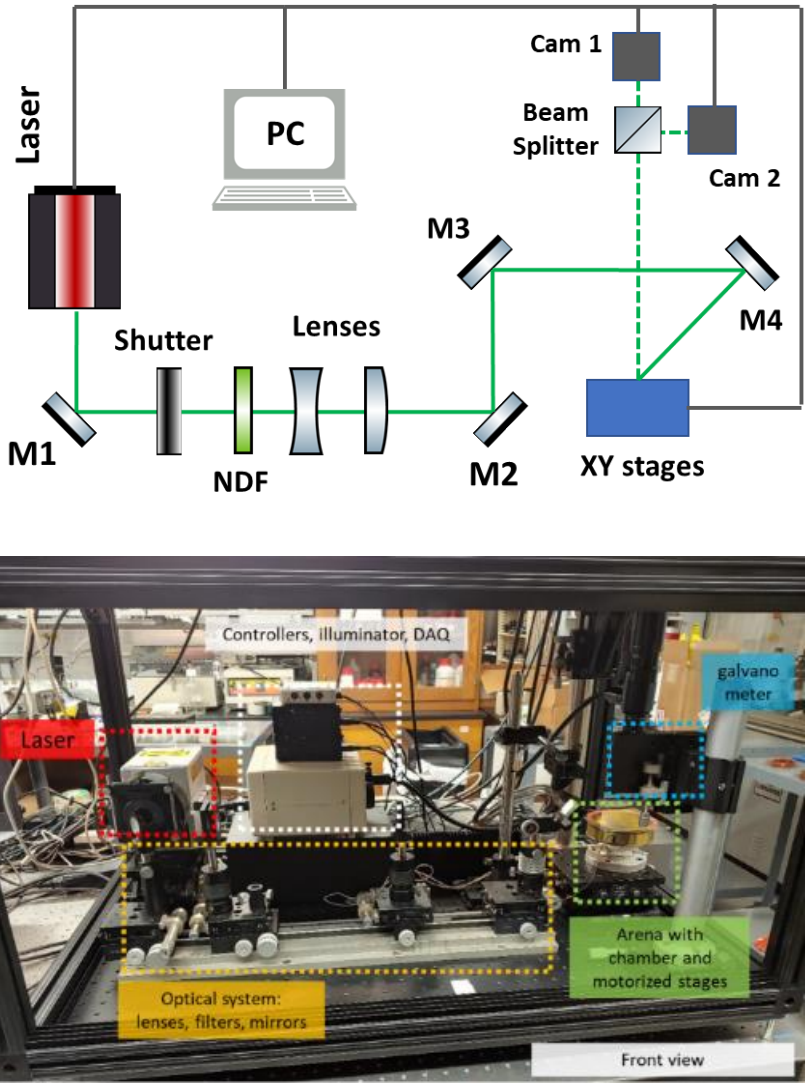

Figure 6-13 Schematic and actual image of experimental setup for SerpenBot steering control.

6.4.2 Neural Network Training Process and Controller Testing

In section 6.3.3, we utilized the approximate kinematic model of the SerpenBot to validate our PID-N-RFL controller in simulation. We then utilized the real experiment data training the forward and inverse kinematic model of the robot to validate the concept and

then applied it to experiments with the robot. To efficiently collect data, we utilized the Monte Carlo method generating random action sequences (left -1, forward 0 or right +1), offsets, and a random period of time as inputs to the robot. The velocity of the robot $\dot{x}$ was calculated by backward differentiation from microscope images using:

$$\dot{x}_{k+1} \approx \frac{x_{k+1}-x_k}{\Delta t}, \tag{6-28}$$

The PID-N-RFL controller utilizing offset as a control variable is depicted in Figure 6-11. Specifically, the control variable $C \in \{c|A \otimes s_o^P, A \in \{-1,0,1\}, s_o^P \in [0,1]\}$, where A is the action deciding to irradiate the laser beam on the left side or the right side of the SerpenBot, s_o^P is the offset relative to the center of the SerpenBot measured in pixels. In our experiment the maximum offset was 80 pixels, based on specific magnification and size of our robot, and the neural network type and size were similar to the simulation case (section 6.3.3).

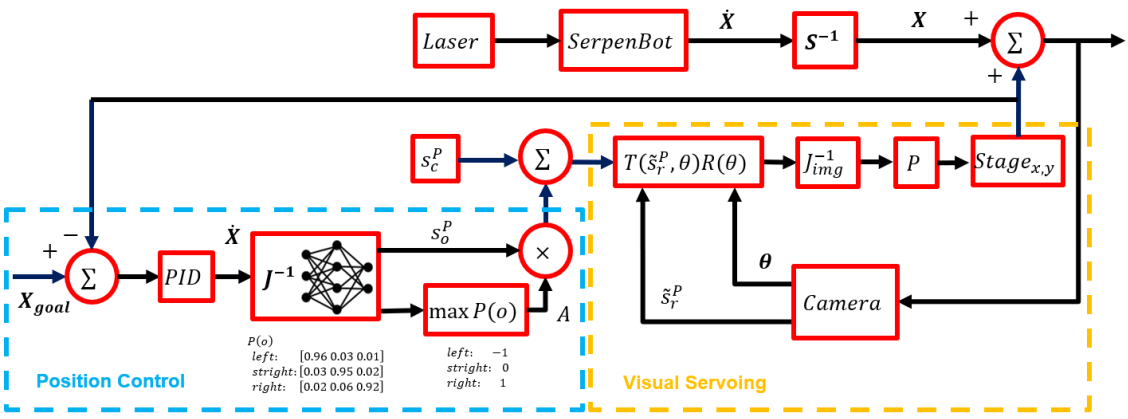

Figure 6-14 PID-N-RFL controller real experiment setup block diagram.

6.5 Experimental Results and Discussion

We conducted a series of experiments to verify the proposed steering strategy involving selective actuation by irradiating specific parts of the SerpenBot. In a first stage of experimentation, we tested whether selective irradiation of the left or right or both actuators would result in an expected and repeatable behavior - motion in a specific direction. In a second stage of experimentation, we have driven SerpenBots along a planned path of specific shape. And, in the third stage of experimentation, we demonstrate automatic goal attainment by direct action with the PID-N-RFL controller.

6.5.1 SerpenBot steering control through selective irradiation

We conducted a series of experiments in order to verify our steering method. Using a user interface written in LabVIEW, we irradiated specific parts of the SerpenBot by manual laser spot control and observed the resulting behavior of our microrobot. Results show that we can realize clockwise and counterclockwise rotation depending on which actuator was under the laser beam (Figure 6-15).

As it can be seen in Figure 6-15e, recorded trajectories are elliptical in shape and for clockwise motions, we have noticed significant drift of the center of rotation. Nevertheless, motion is repeatable and relatively stable, with respect to uninterrupted propulsion through laser irradiation, making it possible to realize number of revolutions continuously (Figure 6-15 c, d, e, f). Combining these three types of SerpenBot's motions allows us to direct the microrobot to a desired location. Hence, we verified our steering strategy and enables future experimental implementation of the proposed control scheme based on the neural network.

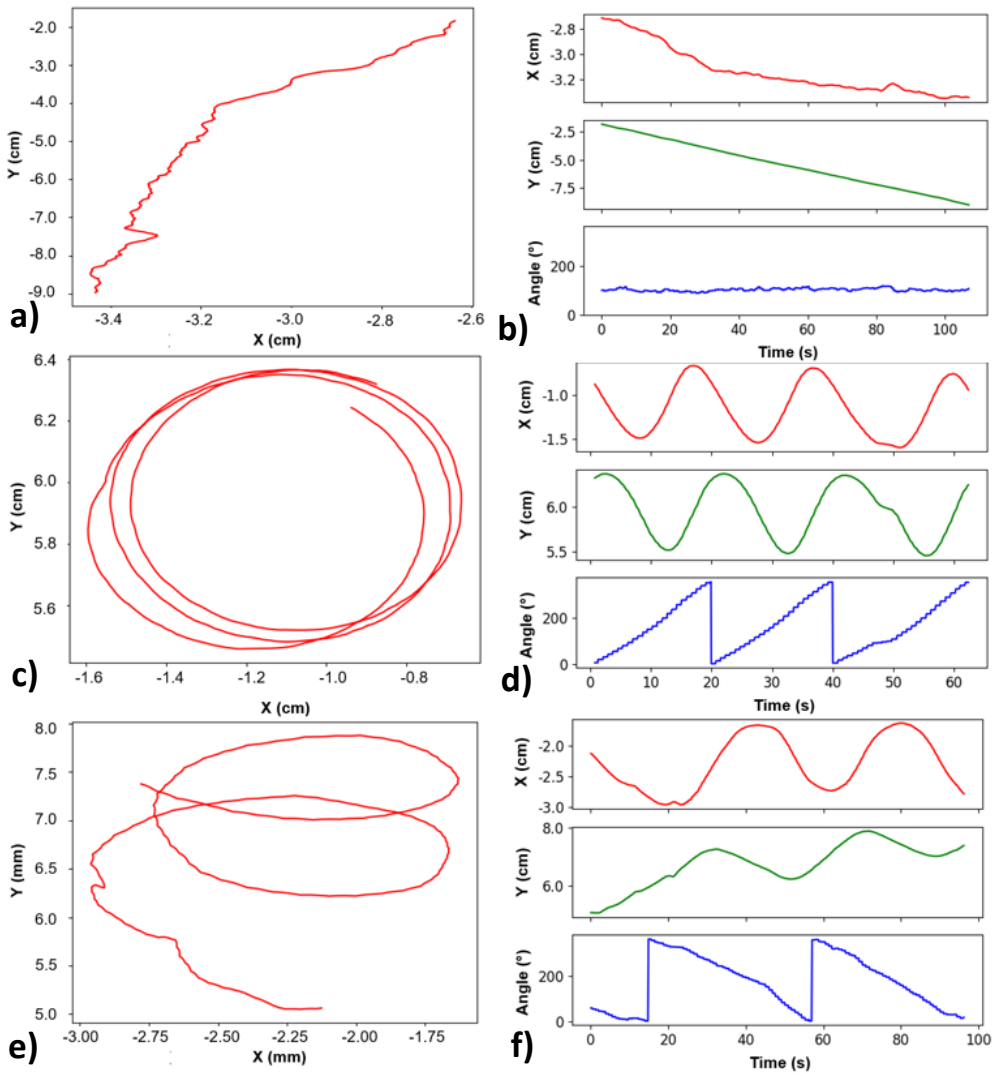

Figure 6-15 Experimental results representing three basic types of SerpenBot motion – on the left trajectories; on the right recorded position (XY) and angle variation with respect to time: a, b) translational motion, c, d) counterclockwise rotation, e, f) clockwise rotation.

6.5.2 SerpenBot steering control through selective irradiation – motion along specific trajectory

For this experiment, we wanted the microrobot to follow a rectangular shape trajectory. Position of the laser beam relative to SerpenBot's body was manually controlled with the help of LabVIEW UI. In Figure 6-16 presents the recorded trajectory of the

SerpenBot along an approximately rectangular shape. In this experiment, the laser frequency was kept constant at 1700 Hz with laser power of 430 mW, and we used the laser's burst mode with 50 pulses per burst, and a delay time between bursts of 300 ms.

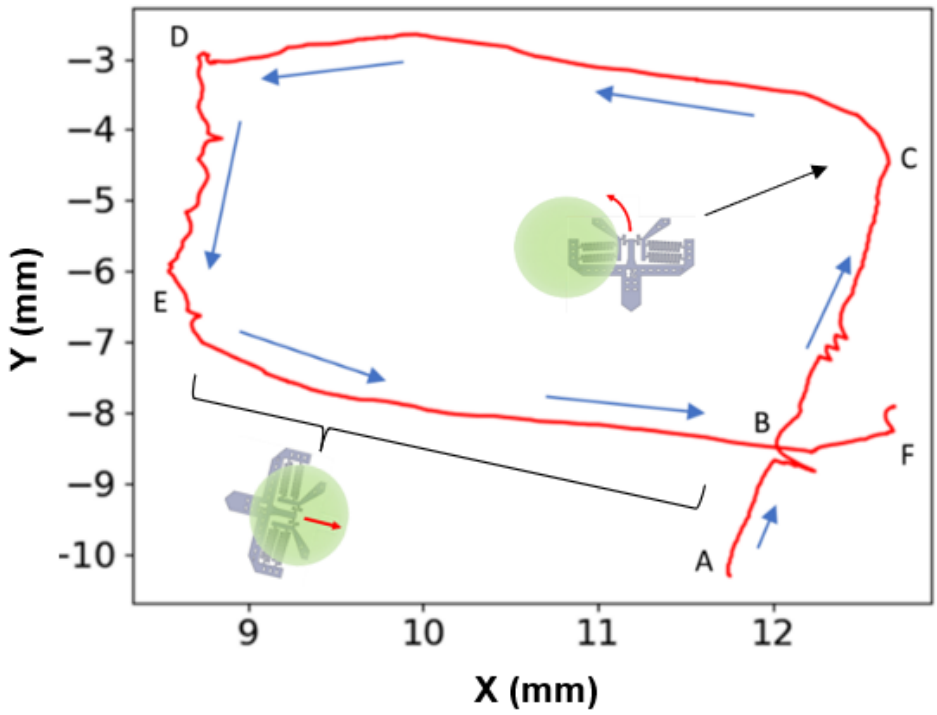

Figure 6-16 SerpenBot steered along rectangular trajectory.

To better understand proposed steering mechanism the trajectory shown in Figure 6-16 can be described in the following way:

1) section AB and BC – microrobot is initially at rest and starts to move forward along straight line upon exposure to a laser light focused on the center of SerpenBot, as depicted in bottom diagram in Figure 6-16.
2) point C – robot turns left after the laser beam was focused on left actuator of the SerpenBot, see top diagram in the plot, Figure 6-16.

3) section CD – laser beam is focused back on center of SerpenBot which moves in forward direction; around ¾ of the CD section robot starts to drift slightly to the left.
4) point D - robot turns left after the laser beam was focused on a left section of robot.
5) section DE – laser beam is focused on center again - robot moves in forward direction.
6) point E – robot turns left again.
7) section EB and BF – finally, the beam is focused on a center of the robot; at point B it intersects section AC and stops at F, after the laser beam is shut off.

Applying the same steering strategy, we were able to move and control SerpenBot of other designs along the trajectories of different shapes (Figure 6-17). For rectangular, triangular, and trapezoidal shapes of paths (Figure 6-17 b, c, d) we followed the same receipt as in case of trajectory from Figure 6-16, switching position of the laser beam depending on the part of the motion. However, for the circular trajectory (Figure 6-17a) we have kept laser beam focused on one of the actuators continuously during the whole travel (Figure 6-14).

Trajectories shown in the Figure 6-15 b, c, d are less stable than “circular” one (Figure 6-17a), which is related to the fact that during motion along the straight path, robots tends to uncontrollably turn, thus continuing adjustments has to be made during the motion by human user inputs with the help of LabVIEW UI. These adjustments include switching the position of the laser beam from one side of the robot to the opposite in order to compensate for the uncontrollable turns to keep it traveling along the main trajectory.

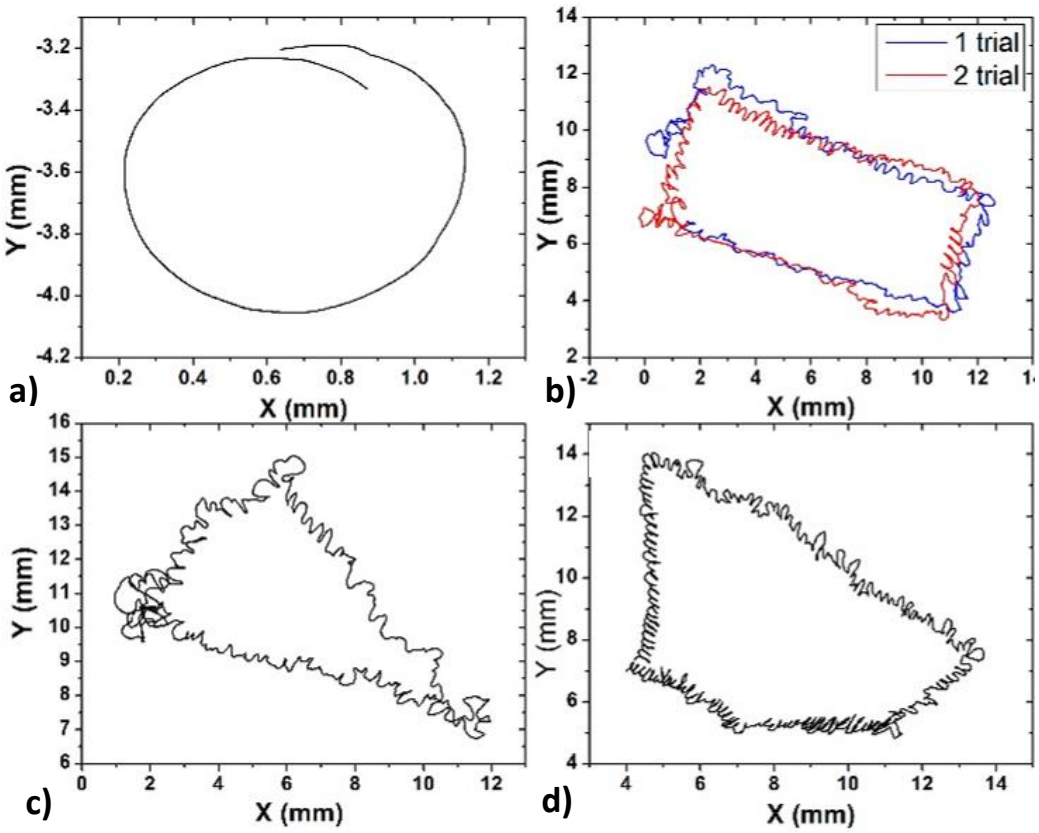

Figure 6-17 SerpenBot trajectories experimentally realized following proposed steering trajectory.

6.5.3 Neural controller training and experimental validation

Using a Monte-Carlo approach to generate microrobot input action, we collected image sequence information and used it to train the inverse neural network approximation of the robot Jacobian. The input signals and output states of the SerpenBot are shown in Figure 6-18, collected for a duration of over 10 minutes. It can be seen that when the input is a positive offset, the angular velocity is also positive, while vice versa, a negative offset produces a negative value of the angular velocity. Furthermore, the loss function during the training process inverse kinematic is shown in Figure 6-19 and converges toward zero after 140,000 data points.

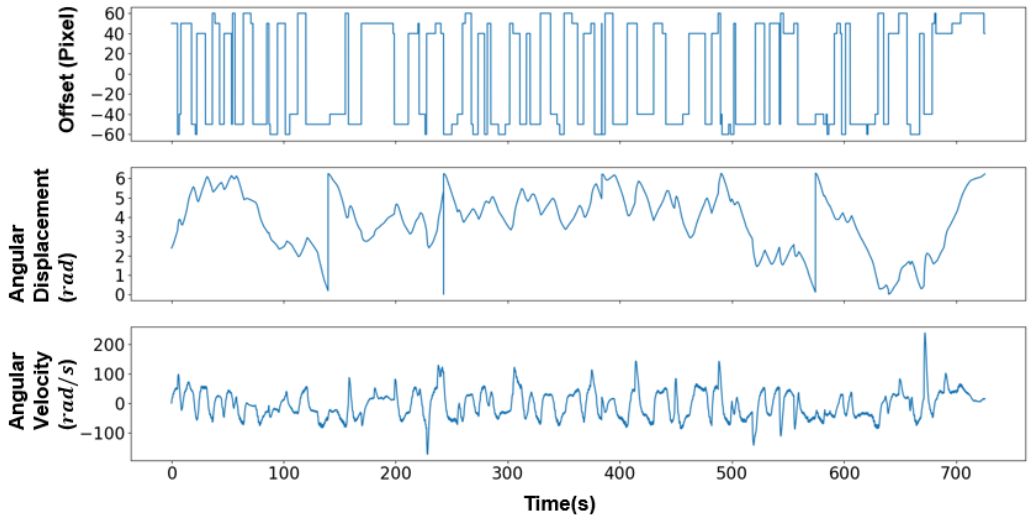

Figure 6-18 Angular velocity and input action sequence.

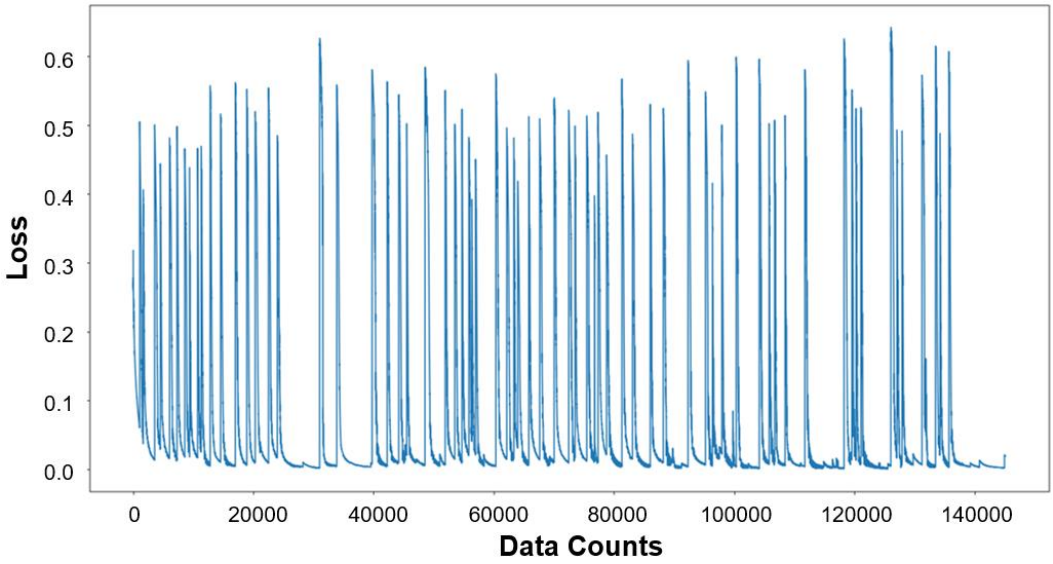

Figure 6-19 Loss during model training process.

After NN training was completed, we applied the PID-N-RFL controller to realize automated steering of the microrobot. For that purpose, we conducted a series of experimental trials to verify the controller's functionality. In our experiment we first defined "goal" location $[x_d^G\ y_d^G\ \theta_d^G]^T$ for the SerpenBot in the arena's (motorized

stages)coordinate frame The controller commands the SerpenBot to move in specific direction by switching laser beam position (offset value) relative to the robot's body, while in parallel continuously verifying current location and orientation of microrobot with respect to the goal's coordinates. Figures 6-20 and 6-21 depict three SerpenBot trajectories obtained by running the PID-N-RFL controller from various initial position and orientation of the microrobot relative the goal. For the 1st trajectory (Figure 6-18a) SerpenBot was traveling from the initial point $[0, 0, 4.022]$ towards goal point $[-5, -5, 1.406]$ in global coordinates – arena's (motorized stages) system of coordinates. It can be clearly seen that the path includes several relatively straight lines (t_0, t_1) and curved sections (arcs, t_0, t_1, t_3, t_4, t_5) with various arc radii. The behavior of the microrobot while traveling along first path (Figure 6-20a) was recorded in the plots of Figure 6-20b showing changes in time of the robot's controller motion parameters (offset, robot's orientation angle, angular velocity, and error) which correspond to specific section of the trajectory and respective time interval (t_0 to t_6). The plots provide insight into our controller's operation as discussed below:

1) In the first section of the trajectory (time interval t_0), SerpenBot travels along two arcs with large radii, and short straight path – first turning sightly clockwise then counterclockwise, which is represented by initial decreasing trend of the angle vs time and negative value angular velocity (Figure 6-20b) (around $10\ s \sim 20\ s$), then slight increase of the angle value – positive value of angular velocity ($20\ s \sim 25\ s$), and plateau with constant value of angle and angular velocity around zero ($25\ s \sim 30\ s$). In the meantime, the value of the offset is constant for the t_0 (Figure

6-20 b), and the error value is decreasing, as microrobot is moving towards goal point.

2) At around $30\ s$ of the motion, at the beginning of the second section t_1, SerpenBot takes a sudden turn clockwise, away from the goal, where angle is increasing, and angular velocity is positive with a rising slope of the distinct peak ($\sim 30\ s$). The controller introduces correction in the motion, by switching the offset from around positive 20 to -40 (Figure 6-20b), consequently we observe that SerpenBot takes a sharp turn counter-clockwise (Figure 6-20a), as angle is decreasing with the time – falling slope of angular velocity distinct peak ($\sim 30\ s$).
3) After robot's course was corrected and set towards the goal – around the middle of the t_2 section, the controller switches offset value back to the positive ($\sim 20\ s$), where SerpenBot move along approximately straight line, orientation angle is slightly decreasing, with minor fluctuation of the angular velocity around 0. Error value keeps decreasing as microrobot is closer to the goal.
4) A similar pattern in SerpenBot's behavior can be observed for the time intervals t_3, t_4, t_5. – similar shape of the trajectory (Figure 6-20a). Sudden deviation of the microrobot from the approximate path leading towards goal, is corrected by switching the offset (laser beam position), which steers the robot towards the desired direction.
5) Finally, SerpenBot reaches the goal location within the error tolerance after approximately $90\ s$ and recorded an average speed of approximately $100\ \mu m/s$.

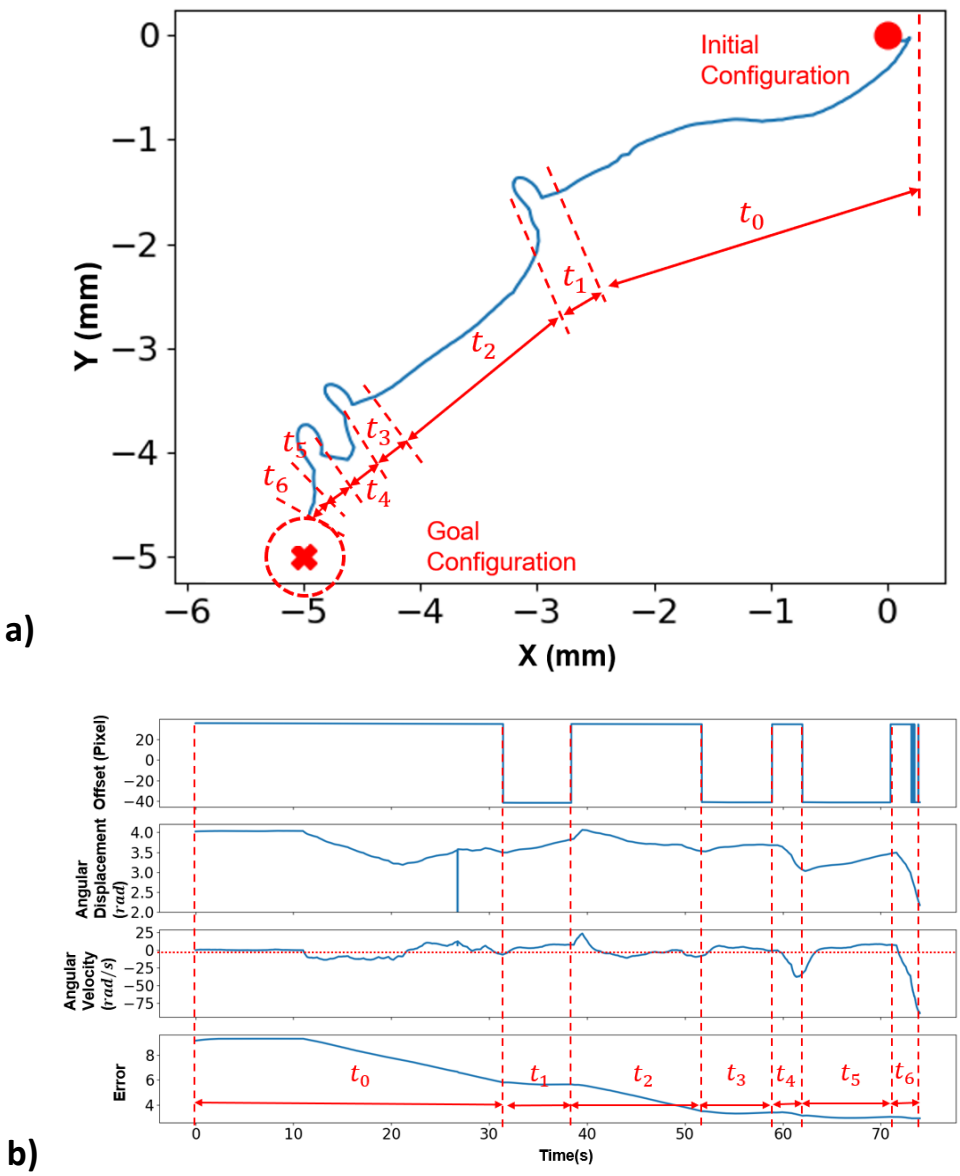

Figure 6-20 a) Trajectory of the SerpenBot with the PID-N-RFL controller. b) Controller output sequence and SerpenBot angular displacement and angular velocity.

In Figure 6-21a, b we have tested additional trajectories verifying controller's functionality for different goal points. By trial-and-error tuning of the PID gain values of our controller, we were able to find $K_v = 1$, $K_{\omega,P} = 10$, $K_{\omega,I} = 0.001$, and $K_{\omega,D} = 0.1$ that seer the motion of the SerpenBot to the desired goals point. In Figure 6-19a, the initial configuration was $[0, 0, 6.188]$ and the goal was $[-5, 5, 5.790]$, while for Figure 6-21b,

the initial configuration was $[0, 0, 2.280]$ and the goal was $[-5, -5, 5.408]$, in both cases microrobot reaches the vicinity of the goal coordinates with a steady-state error between 0.1 and 0.5 mm.

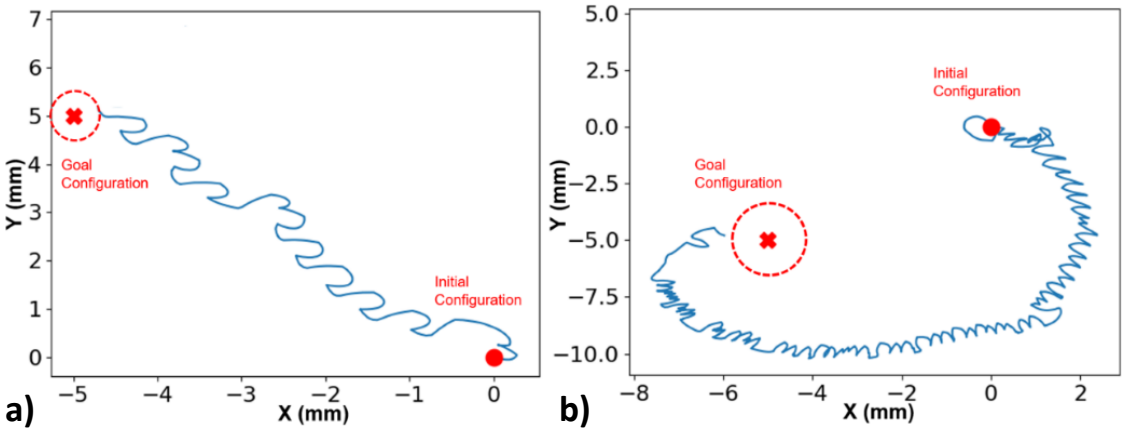

Figure 6-21 Additional experiment results with different starting orientations (B) or goal configuration (A). The steady-state controller error was between from 0.1 to 0.5 mm due to the surface conditions, visual servoing steady-state error.

6.6 Summary

In this chapter we presented a novel design of assembly-less laser driven microrobot on dry surfaces, SerpenBot, along with new fabrication process, which simplified assembly process and optimized experimental process with laser irradiation. We have proposed new steering strategy for SerpenBot based on the selective irradiation of the microrobot's body, which was verified experimentally. Experimental results show that we have a sufficient steering control enabling realization of various planned trajectories. At average linear speed between $10{\sim}100\ \mu m/s$. It is suggested that proposed steering mechanism is a robust approach which allows overcoming the difficulties related to complex surface effects at microscale in dry environments. We experimentally

demonstrated controlled motion of the SerpenBot in all direction on the flat plane – Si substrate. Furthermore, we have conducted simulations of the steering control scheme based on the implementation of the neural network solutions, developed, and experimentally verified PID-N-RFL controller by demonstrating microrobot's motion in desired direction realized autonomously without major human user intervention.

CHAPTER 7 CONCLUSION AND FUTURE WORK

7.1 Conclusion

In this thesis, we proposed a constrained modeling optimization method for assembled microrobots with both serial and parallel geometries. We illustrated the approach using the AFAM microrobot constructed by MEMS assembly. Equations for the constrained Lagrangian method were derived and numerically integrated using the Newton-Raphson method to solve both the forward and inverse kinematics of the microrobot.

The FK and IK solvers were implemented on a simulation platform based on ROS-RViz, which enabled trajectory planning and visualization. Using this framework, we analyzed the workspace, uncertainty, and repeatability of the AFAM. Although the robot repeatability showed that it can perform nanoscale work, the size of the workspace is comparable to the bounding box uncertainty. Therefore, we will pursue an optimized fabrication and assembly process for the AFAM components, especially the cable-arm assembly.

We have developed a dynamical model for SolarPede, a stick-slip multi-legged microrobot that collects solar light energy through a solar-cell and converts it into mechanical energy to achieve crawling locomotion on a Silicon substrate or realize microscale conveyor design for transport of the Si substrates. The model was used to predict the motion of the robot operating under an optical microscope.

In the ChevBot section of this thesis, we presented a modeling methodology for laser-driven microrobots based on a combination of Finite Element Analysis, lumped-model approximations, and experimentation with tethered and untethered prototypes. The ChevBot actuation principle is based on a complex Multiphysics opto-thermo-mechanical conversion and stick-slip friction contact with the substrate. FEA models were used to compare the displacement and time constants of the microrobots in tethered and untethered states. Tethered microrobots were subjected to laser pulses for system identification, and the resulting first-order thermal actuator models were fed into 1D and 2D stick and slip models to predict the velocity and orientation of the ChevBot operating on a flat silicon substrate. Finally, a visual servoing scheme was employed to automatically track the robot and focus the laser beam. Motion tracking results indicate wide agreement with the simulation predictions and reveal that the microrobot is sensitive to robot-substrate friction conditions.

For the SerpenBot, we have introduced a new type of thermal actuator, the Elbow Thermal Actuator (ETA), for a laser-driven MEMS microrobot. Applying theoretical analysis and simulation, we determined that the leverage mechanism of this type of thermal actuator can enhance thermal expansion to achieve larger static displacement. By tuning the geometric parameters of the actuator, such as lengths, widths, and the number of serpentine turns, we can achieve different resonant frequencies of the actuator in a dynamic scenario and design microrobots with different leg responses.

We have experimentally validated our differential leg dynamic models by illuminating SerpenBots with different laser frequencies through a customized laser and visual servoing tracking experimental instrument. The position of the microrobot was

tracked while laser pulse frequencies were swept in a wide range. The results show that it is possible to achieve locomotion and steering control of the robot by tuning the laser frequency. We have determined the experimental frequencies needed to realize locomotion and steering control for two different microrobot designs and verified that the resulting motions are repeatable.

For the controller design of the SerpenBot, we have introduced a neural-network-based controller called the PID-Bayes controller. We have theoretically proved the stability of this controller in the general case and then tailored it to be a PID-N-RFL controller, which we verified through experiments. The experiments showed that this controller can be used to direct the SerpenBot to the desired goal configuration from the arbitrary chosen initial position.

7.2 Future Work

In future work for the AFAM, closed-loop operation could be further improved by integrating joint flexure sensors and implementing visual servoing techniques such as optical microscope, laser interferometry, and SEM imaging.

For the microconveyor robot SolarPede, a closed-loop controller will also need to be designed, and the PID-Bayes controller could be considered for this application as well.

Regarding the SerpenBot, we have implemented a galvanometer for controlling the steering behavior using the PID-RFL controller. As the current setup relies on a motorized stage for selective irradiation of the laser beam on the structure of the SerpenBot, the motion of the system is coupled with the motion of the microrobot and motorized stage.

In future, we will plan to refine our controller, optimize its operation, and continue experimental trials to accomplish SerpenBot's travel along more complex trajectories. We

consider an integration of galvanometer in our experimental set up which would allow us to decouple the laser spot positioning system with the robot substrate motion.

The galvanometer can simplify and decouple these motions to achieve better performance, and further experiments are required to verify the system. Once the galvanometer system is validated, the SerpenBot system could be extended to a swarm of microrobotic systems.

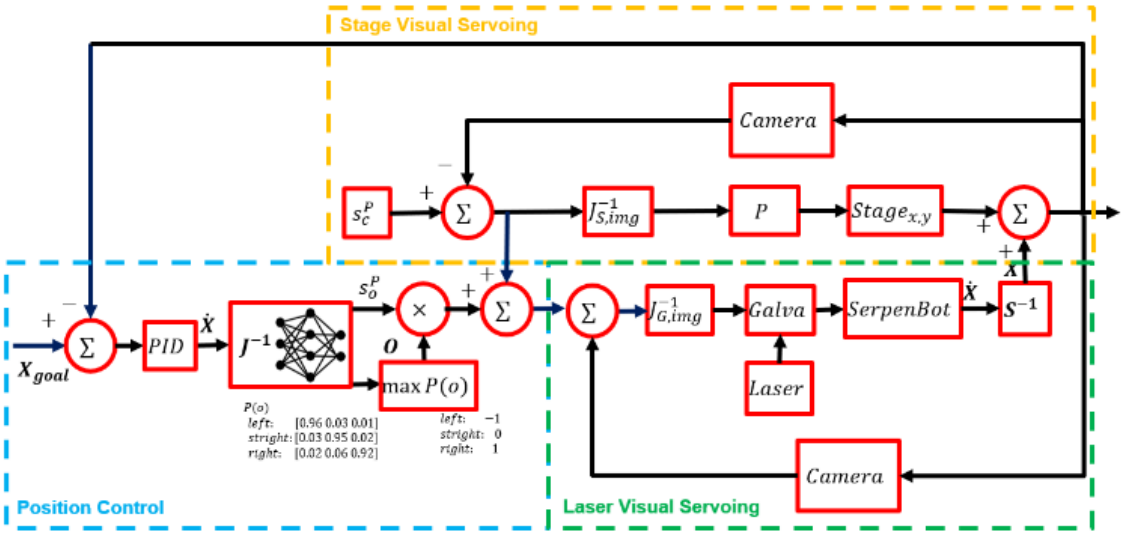

Figure 7-1 Block diagram extending the galvanometer control system for one or multiple SerpenBots.

To model the SerpenBot system more accurately, we still need to determine several unknown or unmeasurable parameters and boundary conditions. To gain a better understanding of the system, we can use a thermal camera to measure the microrobot's thermal behavior and set up an ultrafast camera to observe the motion of the actuators, which can help us understand how the microrobot's legs interact with the arena surface. With this knowledge, we can improve the microrobot's design.

From a control perspective, the camera used for visual servoing is a bottleneck for the system because its frame rate is much slower than the SerpenBot's movement and

response time. To address this issue, we need to develop a localization method that does not rely on a camera.

Since the PID-Bayes controller requires training step of the neural network. To improve the controller further, we can extend it to be a neural-adaptive version of the PID-Bayes controller.

REFERENCES

[1] Galstyan, Vardan & Bhandari, Manohar & Sberveglieri, Veronica & Sberveglieri, Giorgio & Comini, Elisabetta. (2018). Metal Oxide Nanostructures in Food Applications: Quality Control and Packaging. *Chemosensors*. 6. 16. 10.3390/chemosensors6020016.

[2] https://www.britannica.com/technology/nanotechnology/Nanofabrication

[3] Kawahara, N., Suto, T., Hirano, T. et al. Microfactories; new applications of micromachine technology to the manufacture of small products. *Microsystem Technologies* 3, 37–41 (1997).

[4] Y. Okazaki, "Microfactories—A New Methodology for Sustainable Manufacturing", *International Journal of Automation Technology*, 4, 2 (2010) 82-87.

[5] Kitahara T, Ashida K, Tanaka M, Ishikawa Y, Ooyama N, Nakazawa Y (1998) Microfactory and microlathe. In: *Proceedings of international workshop on microfactories*, pp 1–8

[6] Ashida, K. & Mishima, Nozomu & Maekawa, H. & Tanikawa, T. & Kaneko, K. & Tanaka, M.. (2000). Development of desktop machining microfactory. Proc. *J-USA Symposium on Flexible Automation*. 175-178.

[7] N. Mishima, "A Study on a Microfactory and an Evaluation Method of its System Configuration," *2006 International Conference on Mechatronics and Automation*, Luoyang, Henan, 2006, pp. 837-842, doi: 10.1109/ICMA.2006.257718.

[8] I. Verettas, R. Clavel and A. Codourey, "Microfactory: desktop cleanrooms for the production of microsystems," Proceedings of the *IEEE International Symposium on Assembly and Task Planning*, 2003., Besancon, France, 2003, pp. 18-23, doi: 10.1109/ISATP.2003.1217181.

[9] S. Miyashita., S. Guitron, S. Li and D. Rus, “Robotic metamorphosis by origami exoskeletons,” *Science Robotics* 27 Sep 2017: Vol. 2, Issue 10.

[10] M.A, Rahman, J. Cheng, Z. Wang and A.T Ohta, “Cooperative micromanipulation using the independent actuation of fifty microrobots in parallel,” *Scientific Reports* vol.7, Article number: 3278 (2017).

[11] B. J. Nelson, I. K. Kaliakatsos and J. J. Abbott, “Microrobots for minimally invasive medicine.” *Annual Review of Biomedical Engineering*, vol. 12, no. 1, p. 55, 2010.

[12] P. Ryan and E. Diller, "Magnetic Actuation for Full Dexterity Microrobotic Control Using Rotating Permanent Magnets," *IEEE Transactions on Robotics*, vol. 33, no. 6, pp. 1398-1409, 2017.

[13] C. Elbuken, M. B. Khamesee and M. Yavuz, "Magnetic levitation as a micromanipulation technique for MEMS," *2009 International Conference on Mechatronics and Automation*, Changchun, 2009, pp. 955-959.

[14] B. Goldberg, R. Zufferey, N. Doshi, E. F. Helbling, G. Whittredge, M. Kovac, and R. J. Wood, "Power and Control Autonomy for High-Speed Locomotion With an Insect-Scale Legged Robot," in *IEEE Robotics and Automation Letters*, vol. 3, no. 2, pp. 987-993, April 2018.

[15] R. Murthy, A. N. Das and D. O. Popa, "ARRIpede: A stick-slip micro crawler/conveyor robot constructed via 2 ½D MEMS assembly," *2008 IEEE/RSJ International Conference on Intelligent Robots and Systems*, Nice, 2008, pp. 34-40.

[16] J. James, V. Iyer, Y. Chukewad, S. Gollakota and S. B. Fuller, "Liftoff of a 190 mg Laser-Powered Aerial Vehicle: The Lightest Wireless Robot to Fly," *2018 IEEE International Conference on Robotics and Automation (ICRA)*, Brisbane, Australia, May 21-25, 2018.

[17] M. R. Pac and D. O. Popa, "3-DOF untethered microrobot powered by a single laser beam based on differential thermal dynamics," *2011 IEEE International Conference on Robotics and Automation*, Shanghai, 2011, pp. 121-127.

[18] R. Zhang, A. Sherehiy, Z. Yang, D. Wei, C. K. Harnett and D. O. Popa, "ChevBot – An Untethered Microrobot Powered by Laser for Microfactory Applications," *2019 International Conference on Robotics and Automation (ICRA)*, Montreal, QC, Canada, 2019, pp. 231-236.

[19] J. Varona, M. Tecpoyotl-Torres and A. A. Hamoui, "Polysilicon vertical actuator powered with waste heat," *2008 IEEE Custom Integrated Circuits Conference*, San Jose, CA, 2008, pp. 519-522.

[20] G. Barillaro, A. Molfese, A. Nannini, F. Pieri, (2005), “Analysis, simulation and relative performances of two kinds of serpentine springs.” *Journal of Micromechanics and Microengineering*. 15. 736.

[21] A. Ghisi, S. Mariani. “Effect of Imperfections Due to Material Heterogeneity on the Offset of Polysilicon MEMS Structures,” *Sensors (Basel)*. 2019;19(15):3256, July 2019.

[22] Liu, Y. F., Li, J., Zhang, Z. M., Hu, X. H., and Zhang, W. J.: Experimental comparison of five friction models on the same test-bed of the micro stick-slip motion system, Mech. *Sci.*, 6, 15-28, 2015.

[23] D.O. Popa, B.H. Kang, J.T. Wen, H.E. Stephanou, “Dynamic modeling and input shaping of thermal bimorph MEMS actuators,” in *IEEE International Conference on Robotics and Automation*, Taipei, 2003.

[24] Z. Yang, M. N. Saadatzi, R. Zhang, A. Sherehiy, D. Wei, C. K. Harnett, and D. O. Popa, "Multiphysics Dynamic Model Validation Methodology for Laser-Driven Microrobots," *2019 IEEE 15th International Conference on Automation Science and Engineering (CASE)*, Vancouver, BC, Canada, 2019, pp. 1555-1561.

[25] https://www.physikinstrumente.com/en/products/linear-stages/miniature-linear-stages/q-521-q-motion-miniature-linear-stage-103151/

[26] A. Ferreira, S. Boudjabi and J. -. Fontaine, "Dynamic model of an arrayed-type ultrasonic microconveyor for control design," *Proceedings 2002 IEEE International Conference on Robotics and Automation* (Cat. No.02CH37292), Washington, DC, USA, 2002, pp. 3205-3211 vol.3.

[27] N. Arora, M. U. Khan, L. Petit, F. Lamarque and C. Prelle, "Design and Development of a Planar Electromagnetic Conveyor for the Microfactory," in *IEEE/ASME Transactions on Mechatronics*, vol. 24, no. 4, pp. 1723-1731, Aug. 2019, doi: 10.1109/TMECH.2019.2917007.

[28] M. P. Kummer, J. J. Abbott, B. E. Kratochvil, R. Borer, A. Sengul and B. J. Nelson, "OctoMag: An Electromagnetic System for 5-DOF Wireless Micromanipulation," *IEEE Transactions on Robotics*, vol. 26, no. 6, pp. 1006-1017, 2010.

[29] E. Diller, S. Floyd, C. Pawashe and M. Sitti, "Control of Multiple Heterogeneous Magnetic Microrobots in Two Dimensions on Nonspecialized Surfaces," *IEEE Transactions on Robotics*, vol. 28, no. 1, pp. 172-182, 2012.

[30] K. S. Ishii, W. Hu and A. T. Ohta, "Cooperative micromanipulation using optically controlled bubble microrobots," in *IEEE International Conference on Robotics and Automation*, Saint Paul, MN, USA, 2012

[31] H. Chen, C. Wang, X. Li and D. Sun, "Transportation of MultipleBiological Cells Through Saturation-Controlled Optical Tweezers In Crowded Microenvironments," *IEEE/ASME Transactions on Mechatronics*, vol. 21, no. 2, pp. 888-899, 2016.

[32] L. Que, J.-S. Park and Y. B. Gianchandani, "Bent-beam electrothermal actuators-Part I: Single beam and cascaded devices," *Journal of Microelectromechanical Systems*, vol. 10, no. 2, pp. 247 - 254, Jun 2001.

[33] M. Tecpoyotl-Torres, J. Varona, A. A. Hamoui, J. Escobedo-Alatorre and J. Sanchez-Mondragón, "Polysilicon thermal micro-actuators for heat scavenging and power conversion," in Proceedings Volume 7043, *High and Low Concentration for Solar Electric Applications III*, San Diego, California, 2008.

[34] *Fundamentals of Heat and Mass Transfer 7th Edition* by T. L. Bergman, et. al., John Willey & Sons, 2007.

[35] "Optical Absorption Coefficient Calculator," Brigham Young University Cleanroom, [Online]. Available: https://cleanroom.byu.edu/OpticalCalc#. [Accessed 15 9 2018]

[36] C. Clévy, A. Hubert, and N. Chaillet, “Flexible micro-assembly system equipped with an automated tool changer,” *Journal of micro-nano mechatronics*, vol. 4, no. 1-2, pp. 59–72, 2008.

[37] C. Diederichs, M. Mikczinski and T. Tiemerding, "A Flexible and Compact High Precision Micro-Factory for Low Volume Production and Lab-Automation," ISR/Robotik 2014; *41st International Symposium on Robotics*, Munich, Germany, pp. 1-7, 2014.

[38] M. Bartenwerfer and S. Fatikow, "Robotic dual-tip assembly for nanowire handling and integration," *2015 IEEE 15th International Conference on Nanotechnology (IEEE-NANO)*, Rome, pp. 1497-1500, 2015.

[39] S. Zimmermann, T. Tiemerding, O. C. Haenssler and S. Fatikow, "Automated robotic manipulation of individual sub-micro particles using a dual probe setup inside the scanning electron microscope," *2015 IEEE International Conference on Robotics and Automation (ICRA)*, Seattle, WA, pp. 950-955, 2015.

[40] N. Dechev, W. L. Cleghorn and J. K. Mills, "Microassembly of 3D MEMS structures utilizing a MEMS microgripper with a robotic manipulator," *2003 IEEE International Conference on Robotics and Automation*, pp. 3193-3199 vol.3, 2003.

[41] Y. Zhang, B. K. Chen, X. Liu and Y. Sun, "Autonomous Robotic Pick-and-Place of Microobjects," in *IEEE Transactions on Robotics*, vol. 26, no. 1, pp. 200-207, Feb. 2010.

[42] K. F. Bohringer, B. R. Donald, N. C. MacDonald, G. T. A. Kovacs and J. W. Suh, "Computational methods for design and control of MEMS micromanipulator arrays," in *IEEE Computational Science and Engineering*, vol. 4, no. 1, pp. 17-29, Jan-Mar 1997.

[43] R. Murthy, A. Das and D. Popa, "Multiscale Robotics Framework for MEMS Assembly," *2006 9th International Conference on Control*, Automation, Robotics and Vision, Singapore, pp. 1-6, 2006.

[44] T. Foote and S. Cousins, "Precisely Groovy [ROS Topics]," in *IEEE Robotics & Automation Magazine*, vol. 20, no. 1, pp. 13-15, March 2013.

[45] Rakesh Murthy, D. O. Popa , “Articulated MEMS Robot for Microfactory Applications”, *Conference: ASME 2009 International Design Engineering Technical Conferences and Computers and Information in Engineering Conference*, 2009.

[46] R. Murthy, D.O. Popa, “AFAM: An Articulated Four-axis Micro Robot for Nanoscale Applications,” in *IEEE Transactions on Automation Science and Engineering (T-ASE)*, 2012.

[47] "AFAM ROS Repository,” [Online]. Available: http://www.bitbucket.org/nextgensystems/afam

[48] K. Tsui, A. A. Geisberger, M. Ellis and G. D. Skidmore, "Micromachined end-effector and techniques for directed MEMS assembly," *Journal of Micromechanics and Microengineering*, vol. 14, no. 4, 2004.

[49] M. Viani, T. Schaffer, G. Paloczi, L. Pietrasanta, B. Smith, J. Thompson, ¨ M. Richter, M. Rief, H. Gaub, K. Plaxco et al., “Fast imaging and fast force spectroscopy of single biopolymers with a new atomic force microscope designed for small cantilevers,” *Review of Scientific Instruments*, vol. 70, no. 11, pp. 4300–4303, 1999.

[50] K. K. Leang and A. J. Fleming, “High-speed serial-kinematic SPM scanner: design and drive considerations,” *Asian Journal of Control*, vol. 11, no. 2, pp. 144–153, 2009.

[51] R. Yeh, E. J. J. Kruglick and K. S. J. Pister, "Microelectromechanical Components For Articulated Microrobots," *Solid-State Sensors and Actuators, 1995 and Eurosensors* IX. Transducers '95. The 8th International Conference on, Stockholm, Sweden, pp. 346-349, 1995.

[52] N. Sarkar, D. Strathearn, G. Lee, M. Olfat and R. R. Mansour, "A platform technology for metrology, manipulation and automation at the nanoscale," *2017 International Conference on Manipulation, Automation and Robotics at Small Scales (MARSS)*, Montreal, QC, pp. 1-6, 2017.

[53] McClintock, Hayley and Temel, Fatma Zeynep and Doshi, Neel and Koh, Je-sung and Wood, Robert J., The milliDelta: A high-bandwidth, high-precision, millimeter-scale Delta robot, *Science Robotics*, January 2018.

[54] A. Iazzolino, Y. Tourtit, A. Chafaï, T. Gilet, P. Lambert and L. Tadrist, "Pick and release of micro-objects: An actuation-free method to change the conformity of a capillary contact," *2019 International Conference on Manipulation*, Automation and Robotics at Small Scales (MARSS), Helsinki, Finland, 2019, pp. 1-6.

[55] Padgett, Miles & Leonardo, Roberto. (2011). Holographic optical tweezers and their relevance to lab on chip devices. *Lab on a chip*. 11. 1196-205. 10.1039/c0lc00526f.

[56] E. Gerena, F. Legendre, Y. Vitry, S. Régnier and S. Haliyo, "Robotic Optical-micromanipulation Platform for Teleoperated Single-Cell Manipulation," *2019 International Conference on Manipulation, Automation and Robotics at Small Scales (MARSS)*, Helsinki, Finland, 2019, pp. 1-6, doi: 10.1109/MARSS.2019.8860946.

[57] O. Youssefi and E. Diller, "Contactless Robotic Micromanipulation in Air Using a Magneto-Acoustic System," in *IEEE Robotics and Automation Letters*, vol. 4, no. 2, pp. 1580-1586, April 2019, doi: 10.1109/LRA.2019.2896444.

[58] R. Zhang, A. Sherehiy, D. Wei, Z. Yang, M. N. Saadatzi and D. O. Popa, "Tracking Experiments with ChevBot: A Laser-Actuated Stick-Slip Microrobot," 2019 International Conference on Manipulation, Automation and Robotics at Small Scales (MARSS), 2019, pp. 1-6,

[59] Z. Yang, A. Sherehiy, S. S. Chowdhury, D. Wei, R. Zhang and D. O. Popa, "Design, Fabrication and Experimental Validation of a Steerable, Laser-Driven Microrobot in Dry Environments," 2020 IEEE 16th International Conference on Automation Science and Engineering (CASE), 2020, pp. 882-887,

[60] Z. Yang et al., "Multiphysics Dynamic Model Validation Methodology for Laser-Driven Microrobots," 2019 IEEE 15th International Conference on Automation Science and Engineering (CASE), 2019, pp. 1555-1561,

[61] Chowdhury, SS, Yang, Z, Clapacs, PW, & Popa, DO. "Untethered Microrobots With Serpentine Actuators: The Role of Elastics Point Contact & Laser Beam Shape on Their Locomotion." Proceedings of the ASME 2021 16th International Manufacturing Science and Engineering Conference. Volume 2: Manufacturing Processes; Manufacturing Systems; Nano/Micro/Meso Manufacturing; Quality and Reliability. Virtual, Online. June 21–25, 2021. V002T08A008. ASME.

[60] H. Marquez, "Nonlinear Control Systems, Analysis and Design," Wiley Interscience, Hoboken, 2003

[61] Slotine, J.J.E. and Li, W., " Applied Nonlinear Control ", Prentice-Hall, 1991

[62] Goodfellow, I. and Bengio, Y. and Courville, A., " Adaptive Computation and Machine Learning series ", Adaptive Computation and Machine Learning series , MIT Press, 2016

[63] Jose M. Sebastián, Lizardo Pari, Carolina González & Luis Ángel. (2005). A New Method for the Estimation of the Image Jacobian for the Control of an Uncalibrated Joint System. 3522. 631-638.

CURRICULUM VITA

Zhong Yang, Ph.D.
Next Generation System Group (NGS)
Louisville Automation and Robotic Research Institute (LARRI)
Electrical and Computer Engineering Department Louisville, Kentucky, 40209
Email: zhong.yang@louisville.edu
Phone: (520) 241-0257

EDUCATION

University of Louisville, Louisville, KY, USA
Aug 2016 – May 2023
Ph.D. Candidate in Electrical & Computer Engineering, Specialty in Robotics and MEMS design
University of Arizona, Tucson, AZ, USA
Master of Science in Electrical & Computer Engineering
Apr 2013 – May 2016
Tianjin University Renai College, TianJin, China
B.E in Electrical Science & Technology
Sep 2008 – Jun 2012

TECHNICAL SKILLS

Languages: C/ C++, Python, Matlab, Labview
Software: ANSYS, Comsol, Solidworks, L-Edit
Cleanroom tools: Suss Mask Aligner (photolithography), DRIE, HF wet etch, HF Vapor Etch, Dektak Profilometer, Filmetrics, Lesker PVD 75 (sputtering), Oxford PECVD, Spin Coating, YES Image Reversal Oven.

RELEVANT EXPERIENCES

AFAM Microrobot Control Application, Louisville, KY, USA
Spring 2018
Kinematic modeling for microrobotic arm.

Implement the control framework and nonlinear solver of the microrobotic arm with C++ in ROS environment.

Skin Sensor Design, Louisville, KY, USA
Fall 2017 – Spring 2023
Sensor structure design with Solidworks.
FEA (Finite Element Analysis) modeling & simulation with Comsol.
Mask design with L-Edit.

SolarPede Microrobot design, Louisville, KY, USA
Fall 2019 – Spring 2023
Microrobot actuator structure design with Solidworks.
FEA (Finite Element Analysis) modeling & simulation with ANSYS.
Dynamic modeling & simulation with Simulink.
Mask design with L-Edit.
Cleanroom fabrication & test.

ChevBot/SerpenBot Microrobot design, Louisville, KY, USA
Fall 2019 – Spring 2023
Microrobot actuator structure design with Solidworks.
FEA (Finite Element Analysis) modeling & simulation with ANSYS.
Dynamic modeling & simulation with Simulink.
Mask design with L-Edit.
Cleanroom fabrication & test.
Control & Vision servoing system design and implement with Labview.

PATENTS

Joshua R Baptist, Mohammad Nasser Saadatzi, **Zhong Yang**, Ruoshi Zhang, Dan O Popa, "Robot skin apparatus, method of fabricating a robot skin apparatus, and a system including a robot skin apparatus", US Patent: US20200070356A1

PUBLICATIONS

Ruoshi Zhang**, Zhong Yang**, Danming Wei, Dan O. Popa, "Design and fabrication of an articulated four axes microrobot arm," Proc. SPIE 10216, Smart Biomedical and Physiological Sensor Technology XIV, 102160C (16 May 2017)

Mohammad Nasser Saadatzi, **Zhong Yang**, Joshua R. Baptist, Ritvij R. Sahasrabuddhe, Indika B. Wijayasinghe, Dan O. Popa, "Parametric investigation of scalable tactile sensors," Proc. SPIE 10216, Smart Biomedical and Physiological Sensor Technology XIV, 102160A (16 May 2017).

Z. Yang and D. O. Popa, "A General Kinematic Modeling Framework for a 3D Compliant Micromechanism," *2018 International Conference on Manipulation, Automation and Robotics at Small Scales (MARSS)*, 2018, pp. 1-6.

R. Zhang, A. Sherehiy, **Z. Yang**, D. Wei, C. K. Harnett, and D. O. Popa, "ChevBot – An Untethered Microrobot Powered by Laser for Microfactory Applications," *2019 International Conference on Robotics and Automation (ICRA)*, 2019, pp. 231-236.

M. N. Saadatzi, J. R. Baptist, **Z. Yang** and D. O. Popa, "Modeling and Fabrication of Scalable Tactile Sensor Arrays for Flexible Robot Skins," in *IEEE Sensors Journal*, vol. 19, no. 17, pp. 7632-7643, 1 Sept.1, 2019.

Jordan F. Klotz, Danming Wei, **Zhong Yang**, Ruoshi Zhang, Andriy Sherehiy, Mohammad N. Saadatzi, Dan O. Popa, "Concept Validation for a Novel Stick-and-Slip, Light-Powered, Mobile Micro-Crawler," *2019 International Conference on Manipulation, Automation and Robotics at Small Scales (MARSS)*, 2019, pp. 1-7;

Zhong Yang, Mohammad N. Saadatzi, Ruoshi Zhang, Andriy Sherehiy, Danming Wei, Cindy K. Harnett, Dan O. Popa, "Multiphysics Dynamic Model Validation Methodology for Laser-Driven Microrobots," *2019 IEEE 15th International Conference on Automation Science and Engineering (CASE)*, 2019, pp. 1555-1561

R. Zhang, A. Sherehiy, D. Wei, **Z. Yang**, M. N. Saadatzi and D. O. Popa, "Tracking Experiments with ChevBot: A Laser-Actuated Stick-Slip Microrobot," *2019 International Conference on Manipulation, Automation and Robotics at Small Scales (MARSS)*, 2019, pp. 1-6.

Ruoshi Zhang, Jordan F. Klotz, Danming Wei, **Zhong Yang**, Andriy Sherehiy, Mohammad N. Saadatzi & Dan O. Popa, "SolarPede: a stick-and-slip, light-powered, Mobile micro-crawler." J Micro-Bio Robot 16, 1–12 (2020).

Z. Yang, A. Sherehiy, S. S. Chowdhury, D. Wei, R. Zhang, and D. O. Popa, "Design, Fabrication and Experimental Validation of a Steerable, Laser-Driven Microrobot in Dry Environments," *2020 IEEE 16th International Conference on Automation Science and Engineering (CASE)*, 2020, pp. 882-887

S. S. Chowdhury, **Z. Yang**, A. Sherehiy, R. Zhang, D. Wei, and D. O. Popa, "Parametric Investigation of Laser-Driven Microrobot Maneuvrability on Dry Substrates," *2020 International Conference on Manipulation, Automation and Robotics at Small Scales (MARSS)*, 2020, pp. 1-6.

Zhong Yang, Moath Alqatamin, Andriy Sherehiy et al. Learning Control of a Laser-Driven Locomotive Microrobot for Dry Environments, 22 December 2022, PREPRINT (Version 1) available at Research Square

So do not fear, for I am with you; do not be dismayed, for I am your God. I will strengthen you and help you; I will uphold you with my righteous right hand."

Isaiah 41:10